Photoluminescence Spectroscopy of $CdSe/Cd_{0.5}Zn_{0.5}S$ Core/Shell Colloidal Quantum Dots

by

Jamie Brar

Thesis submitted to the Faculty of Graduate and Postdoctoral Studies
in partial fulfillment of the requirements for the degree of
Master of Science in Physics

Department of Physics
University of Ottawa
Ottawa-Carleton Institute for Physics

Abstract

The photoluminescence (PL) of dense aggregates of CdSe/$Cd_{0.5}Zn_{0.5}S$ core/shell colloidal quantum dots (cQDs) was investigated to gain insight into bleaching processes, quantum efficiency behaviour, band gap energy temperature dependence, and the phonon-coupling contribution to thermal broadening. This work also encompassed a study of various sample preparation techniques. These newly investigated strain-engineered core/shell cQDs, having an effective lattice constant in between that of CdS and ZnS, fosters the study of novel properties not present in the previous two systems. The bleaching behaviour, studied subject to strong optical pumping for different external cQD environments, showed effective shell passivation, thus limiting non-radiative processes mainly to the core or shell structures. The relative quantum efficiency was determined as a function of temperature, showing two distinct regimes, with activation of a phonon process above ~ 180 K. The band gap energy was found to follow the empirical Varshni relation describing the temperature dependence of a semiconductor material, dominating any thermally induced changes of the cQD volume and confinement potential. The PL spectral width change with temperature showed highly coupled carrier-phonon scattering behaviour.

Statement of Originality

The author declares that she obtained the results presented in this thesis during the period of her M.Sc. research project under the supervision of Dr. H. P. Schriemer and co-supervision of Dr. K. Hinzer. This work is to the best of her knowledge original.

The strain-engineered core/shell colloidal quantum dot samples studied were fabricated by Dr. C. Nì. Allen's group at Université Laval. Her team provided the estimates of the quantum dots' structures dimensions and concentration in solution given in Table 2. Preparation of Sample 3 described in Chapter 3, along with the accompanying work described in Appendix A, was done by the author at the facilities of Centre d'Optique, Photonique et Laser (COPL) at Université Laval with the assistance of Ph.D. candidate Vincent Veilleux.

The following contributions cover results presented in this thesis:

1. Brar, J., Veilleux, V., Krug, P., Hinzer, K., Allen, C. Nì., Schriemer, H., "Photoluminescence of Strain-Engineered CdSe/$Cd_{0.5}Zn_{0.5}S$ Core/Shell Colloidal Quantum Dots," refereed conference publication for *2011 Integrated Photonics Research, Silicon and Nano Photonics (IPR) Topical Meeting*, Toronto (2011).
2. Brar, J., "Photoluminescence spectroscopy of colloidal quantum dots," oral presentation at the Ottawa Carleton Institute for Physics Fall Graduate Student Symposium, Ottawa (2010).

3. Brar, J., Veilleux, V., Krug, P., Allen, C. Nì., Schriemer, H., “Low temperature photoluminescence spectroscopy of quantum dots,” poster presentation at *Photonics North 2010*, Niagara Falls (2010).

Acknowledgements

I owe my gratitude to a number of people I have interacted with over the course of this work. I would first like to thank my supervisor, Dr. Henry Schriemer, for the opportunity to work on such an interesting project and for his guidance, especially when motivating me to perform certain tasks thoroughly in the lab until I fully understood the underlying behaviour. I would also like to thank my co-supervisor, Dr. Karin Hinzer, for all of her constant advice and feedback and for always motivating me. Furthermore, I am indebted to Dr. Peter Krug for his immense supervision in the lab.

I would like to express my gratitude to Dr. Claudine Allen for the quantum dot samples and for the opportunity to visit her laboratory at Université Laval. I also thank her student Vincent Veilleux for spending time with me to prepare samples.

I am grateful for having had the opportunity to visit Dr. Sylvain Raymond's laboratory at the NRC Institute for Microstructural Sciences. I thank him, William Render, and David Roy-Guay for providing me with my first hands-on photoluminescence training.

I am grateful to have worked with Alex Ip when initially setting up the lab. I am also grateful to have worked with Olivier Thériault and for all of his assistance. Moreover, I am thankful for all of the guidance and advice from Dr. Chris Valdivia and Dr. Jeff Wheeldon.

I additionally would like to thank anyone I have shared lab or office space with and everyone in all the neighbouring photonics labs in SITE, including Nic Olivieri and all SUNLab members.

Finally, I would like to thank my family and friends for their support.

Contents

Figures

Tables

Abbreviations

Asym2Sig	Asymmetric double sigmoidal
CCD	Charge coupled device
cQD	Colloidal quantum dot
FDSW	Finite-depth square well
FFT	Fast Fourier transform
FI	Fluorescence intermittency
FRET	Förster resonance energy transfer
FWHM	Full width at half maximum
LED	Light emitting device
LN2	Liquid nitrogen
LO phonon	Longitudinal optical phonon
MBE	Molecular beam epitaxy
MOCVD	Metal-oxide chemical vapour deposition
MOSFET	Metal-oxide semiconductor field effect transistor
NIR	Near-infrared
PI	Pump intensity
PL	Photoluminescence
PLE	Photoluminescence enhancement
PMMA	Polymethyl acrylate
QCSE	Quantum confined stark effect
QD	Quantum dot
TE	Transverse electric
TM	Transverse magnetic
UV	Ultraviolet

Chapter 1 Introduction

1.1. History and introduction to quantum confinement

Quantum confinement has been of great interest since the 1920s [1], and is a phenomenon exhibited by nanoscale materials, which are among one of today's prevalent research topics. During the mid-1800s, however, Faraday unknowingly encountered quantum size-dependence in thin gold films [2].

In the 1970s, etching and lithographic fabrication techniques allowed Esaki et al. [3,4] to experimentally study the first semiconductor quantum heterostructure, in which the abrupt bandstucture change between two materials introduces new phenomena. Quantum wells, films of nanoscale thickness sandwiched between materials of larger band gap energies were soon after created, leading to the development of a superlattice consisting of a periodic array of wells. Quantum wells and superlattices exhibit quantization of energy levels in the direction of reduced spacial dimension, restricting movement of electron and hole charge carriers to a two-dimensional plane.

One-dimensional quantum wires and zero-dimensional quantum dots (QDs) were later created. The electronic spectra of QDs is a series of discrete states dependent on the size of the structure or the amount of confinement. The density of electronic states also increases from that in the bulk material. The first QDs studied by chemists in the 1980s [5,6,7] were dispersed throughout glass matricies [1,8] and were known as colloidal nanocrystals or cQDs. Today cQDs are commonly fabricated by wet chemistry techniques and suspended in organic solvents. Stransky-Krastanov QDs, which are islands nucleating out of strained epitaxial layers, were later developed using molecular beam expitaxy (MBE) and metal oxide chemical vapour deposition (MOCVD) techniques [5]. Both QD types are widely researched today and they each present their own advantages and disadvantages.

1.2. Core/shell colloidal quantum dots

The nanocrystal's shape affects its properties. The bulk material, of macroscopic dimensions, has an electronic bandstructure that is composition-dependent due to bond strengths in different material types. Reducing at least one of the material's dimensions to confine the charge carriers changes the bandstructure [3]. The larger the confinement potential, or the smaller the spacial dimensions, the larger the shift in the band gap energy. The QD, confined in all three dimensions, has a widely tunable band gap due to variation in the material size, shape, and composition.

The optical properties of a cQD depend on both its internal and surface configuration. The large surface-to-volume ratio implies that the surface properties may have a great effect on the optical properties. The surface atoms, which are not completely bonded to the inner crystal lattice, contain dangling bonds which can serve as trap sites for photoexcited carriers and thus increase non-radiative decay [5].

To minimise carrier trapping at these surface atoms, the surface can be passivated to "fill" these bonds by deposition of another material onto the surface. One way that the surface may be passivated is by binding organic ligands to the surface bonds [9]. However, it has been observed that using a chemical bath deposition method to grow an epitaxial-like shell of inorganic material onto the cQD "core" provides better passivation [9]. This shell passivates the surface, confines the core to a deeper potential well, and electrically shields the core from the environment.

The shell can be subsequently passivated with organic ligands, for suspension in an organic solvent and prevention of agglomeration between neighbouring nanocrystals. A core/shell cQD is shown in Fig.1.1. The resulting properties of the core/shell cQD can be tuned by the shell's parameters, such as composition and thickness [9]. Appropriate shell parameters can even allow for tunability of the emission wavelength over a larger spectral range than available with both materials alone [9].

The band alignment of the core/shell system can be of one of three classifications: Type-I, Reverse Type-I, and Type-II [9]. In the first, the band gap of the shell is larger than that of the core, so that the electrons and holes are both confined in the core. In the reverse case, the band gap of the shell is smaller than that of the core. The electrons and holes are either partially or fully confined to the shell material, depending on its thickness. The last

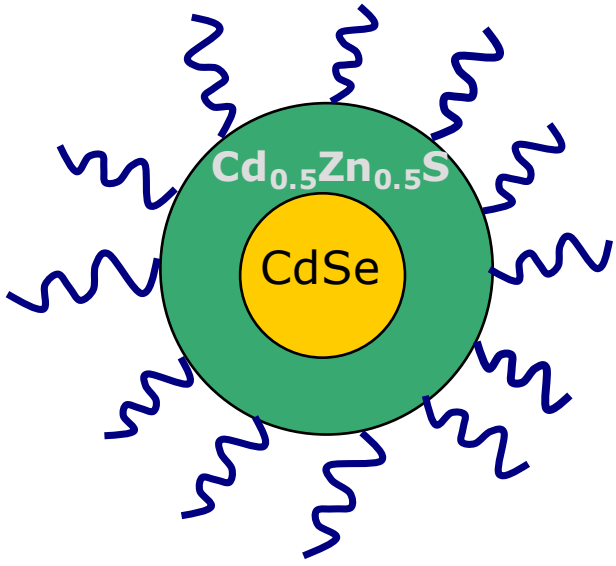

Fig.1.1: Diagram of a CdSe/$Cd_{0.5}Zn_{0.5}S$ core/shell cQD. The shell surface is passivated with organic ligands.

case consists of a staggered band alignment in which either the top of the shell's valence or the bottom of the core's conduction band lies within the band gap of the core.

A common technique for shell growth onto core seeds is the successive ion layer adsorption and reaction (SILAR) method [9,10]. Cationic and anionic precursors are alternately injected into a solution of the cores to form one monolayer of shell material at a time. The shell material, precursors for shell growth, and shell thickness are considered before growing the shell.

The shell, grown onto the core in an epitaxial-like manner, should nominally have a small lattice mismatch with the core, otherwise the resulting strain energy at the interface leads to the formation of lattice defects, which can serve as carrier traps. New mechanisms to tune the cQD properties, on the other hand, are being realized by strain engineering the shell [9,10]. In comparison to bulk crystals, an isolated cQD deforms more easily by the overgrowth of a strained shell since it has a larger fraction of surface atoms. Strained shells can even be grown to change a Type-I core/shell system to a Type-II bandstructure. Strain engineered shells, still in their early stages of research, are being exploited to tune the overlap of the electron and hole wave functions to tailor the system to have a higher probability of recombination or a greater separation of carriers.

The precursors for growing the shell are chosen to have a high reactivity and selectivity, so that they do not produce other side reactions. The amount of precursors must

be chosen so that the shell thickness is not so thin that it does not properly passivate the core, but also not so thick that it increases strain to introduce defects at the core/shell interface or within the shell structure.

This thesis studies a specific sample from a series of CdSe/$Cd_xZn_{1-x}S$ core/shell cQDs that were grown by Dr. Claudine Allen's group at Université Laval. They varied the lattice parameter between x=0 and x=1 to study the effect of lattice mismatch between 3.9 % for CdS and 12 % for ZnS on the cQDs' optical properties. A larger lattice-mismatched shell introduces more strain energy on the core: this can affect the electronic bandstructure and introduce defects at the core/shell interface [10]. The sample studied in this thesis is from a batch with x=0.5, having a shell whose mean lattice constant is midway between that of CdS and ZnS. Although this work does not investigate the strain induced properties on cQDs, the sample has a strain-engineered shell which can influence its optical properties.

cQDs have some advantages over Stransky-Krastanov QDs, which are self-assembled islands grown on bulk materials in a vacuum [11]. A thin "wetting layer" material with different lattice constant is deposited onto the bulk substrate and the resulting strain causes spontaneous formation of islands with bases of diameter ~<100 nm and height of ~10 nm [11]. cQDs made from II-VI semiconductor materials are easier and less expensive to fabricate. They can be fabricated with more monodispersivity, or less size variation [5]. A reasonably symmetric spherical shape can be achieved, typically with diameters <10 nm, and they are closer to exhibiting a discrete delta-function-like density of states. Smaller sized cQDs can be achieved, allowing for their emission to be tuned from the ultraviolet (UV) to the near-infrared (NIR) regions of the spectrum. The cQDs' surface properties, however, are not well characterized and can alter their optical properties [5]. The III-V Stransky-Krastanov QDs, in contrast, typically emit within the infrared and can be more easily implemented into many existing electronic and photonic devices. Their fabrication, however, is more expensive than solution-processible cQDs.

1.3. Photoluminescence in quantum dots

One way that quantum confinement in QDs can be studied is by looking at the material's optical response. Photoluminescence (PL) is photon emission due to excitation of electronic

states with light. After photon absorption, an electron can decay to a lower energy state to recombine with the vacancy, or "hole", and emit a photon of energy equal to the difference between the two states. Most semiconductors have band gap energies corresponding to the visible, near- and mid-infrared light, so PL is a common method in which visible laser light can be used to excite transitions to study their energy levels.

1.4. Applications

Although QDs were first developed to investigate quantum confinement in a regime between the molecular and macroscopic states [12], it was soon found that their size-dependent properties could aid the development of new technologies. Some applications include their use in: biological imaging, light emitting devices (LEDs), solar cells, and memory elements.

Biological imaging:

It has become increasingly important to develop imaging techniques to study very small biological structures. cQDs were first used as biological labels in 1998 [5]. cQDs are advantageous over molecular dyes for their photostability, narrower fluorescence linewidths to simultaneously track multiple molecules, and their broader absorption spectrum with ability to absorb in the infrared where blood is more transparent. To incorporate into biological environments, their surface ligands must be modified so that they are water-soluble and their size must allow them to withstand hydrodynamic forces [13]. One concern is the toxicity of some cQD elements, such as cadmium and lead.

Light emitting devices (LEDs):

LEDs emit light based on radiative recombination of electron-hole pairs from forward-biasing a p-n junction diode [14]. cQDs can improve these devices with their high quantum efficiency, narrow emission band, size-tunable emission over the ultraviolet to near-infrared frequencies, and inexpensive fabrication. CdSe cQDs were first used in LEDs by Colvin et al. in 1994 [15]. Much research thus far has investigated using emission from organic electron and hole transport layers to excite thin layers of cQDs [5,16]. White light can be created by arranging cQDs of specific sizes so that their collective emission follows a

blackbody spectrum. To improve LED applications, the cQDs' photostability and quantum efficiency must be improved.

Solar cells:

Solar cells are photovoltaic devices that generate current by photoinduced charge carriers. Silicon has traditionally been used due to its abundance and low cost, but other materials are being investigated to improve efficiencies. Incorporating cQDs provide the advantage of size-tunable properties and inexpensive fabrication. Hybrid bulk heterojunction donor-acceptor solar cells use conductive conjugated organic polymer layers to form a semiconductor-like p-n junction, and incorporating cQDs can improve efficiency of charge carrier separation [16]. Alternatively, all-inorganic solar cells can be made by stacking QDs layers, each absorbing a particular spectral band. Johnston et al. [17] were the first to create a cQD Schottky diode based device using a PbS cQD film. Dye sensitized solar cells, based on a photoelectrochemical process, traditionally use a ruthenium molecular synthetiser to absorb light [16]. As ruthenium is a precious metal in limited supply, cQDs have been alternatively used. So far, these latter cells have efficiencies that are an order of magnitude lower than that of the former ones.

Memory elements:

cQDs have been explored for use in memory elements due to their size-dependent electronic and magnetic properties, hysteresis effects, and low cost fabrication. Flash memory traditionally uses a polycrystalline silicon floating gate within a metal-oxide semiconductor field effect transistor (MOSFET). Bit information can be stored into and erased from the floating gate by applying positive and negative voltages, respectively. A defect in the floating gate can create an electron discharge path and subsequently damage the memory. In 1996, IBM proposed to use a layer of nanocrystals to each independently store electrons as the floating gate [16]. Resistance-change or random access memory devices use materials that can switch between high and low resistances subject to an electric pulse [16]. Metal and semiconductor nanocrystals in hybrid organic-inorganic composites have been recently investigated. In 2000, Sun et al. [18] proposed the use of ferromagnetic nanocrystals in magnetic data storage applications, or hard disk drives. Applying an electric field can align their spin orientations and bit information can be stored in their magnetic moments. The

nanocrystals' magnetic properties, such as temperature stability, need to be better controlled to create these devices.

Summary:

cQDs and other nanomaterials are at the forefront of today's research in the development of new technologies. In order to exploit their full potential, however, much research is needed in the understanding and controllability of their physical properties and their chemical synthesis. Thus, an area of research initially driven by pure scientific interest is now being cyclically propelled by interest to improve technology and to expand scientific knowledge.

1.5. Thesis outline

Chapter 2 covers theoretical properties of the cQDs, including a partial derivation of the electronic states and the PL properties. Chapter 3 describes the experimental methods for both sample preparation and the PL spectroscopy apparatus for characterization of the samples. Chapter 4 discusses results of PL measurements. Chapter 5 concludes with a summary of results and a brief discussion of possible future work.

Chapter 2 Theory

This chapter discusses theoretical properties of the cQDs which can be related to the experimental results. The electronic states in a bulk semiconductor are first examined. The Hamiltonian for this system is then modified with a finite depth square well (FDSW) model to describe the energy levels of the cQDs. A description of the PL properties as a function of pump intensity (PI) follows to determine the cQDs' quantum efficiency. A description of temperature dependent properties, affecting the band gap and spectral width, is then given. The chapter ends with a discussion of non-radiative PL mechanisms in cQDs.

2.1. Energy levels in bulk semiconductors

The Hamiltonian is first described for the ground state electronic motion in an ideal bulk semiconductor. The ideal crystal is assumed to be infinitely large so that surface properties do not affect the electronic states and the nuclei are periodically spaced in the lattice. The allowed electronic states for this system lie within two bands of continuous levels and are separated by a forbidden region. The magnitude of energy difference between these two bands is called the band gap energy. In the ground state, the valence band energy levels are completely occupied and the conduction band is unoccupied. Excited states involve transitions of electrons from the valence to the conduction band. An excited electron leaves a vacancy, or hole, in the valence band that acts as a particle with opposite charge to that of the electron. Electron-hole pairs exhibit a mutual Coulomb interaction and they can form bound states called excitons.

The Hamiltonian can be expressed by six terms [19]. It contains two kinetic energy terms, one for electrons and another for the nuclei. A third term represents the potential energy of the interaction of nuclei, a fourth for the electron-nucleus interaction potential, and a fifth for the electron-electron interaction. The last term contains additional factors depending on spin, such as spin-orbit interaction.

This Hamiltonian cannot be solved exactly, so it is necessary to make some approximations. The first assumption is that the nuclei are much heavier than the electrons,

so the vibrational motion of the nuclei can be separated from the electron motion. The Hamiltonian is then constructed as follows [19]:

$$H = H_e(\boldsymbol{r_i}, \boldsymbol{R_I}) + H_{ions}(\boldsymbol{R_I}) + H_{e-ion}(\boldsymbol{r_i}, \boldsymbol{\delta R_I}) + H_S, \quad (1)$$

where the first term is the electron motion relative to static nuclei, the second is the nuclei motion, the third is the electron-phonon interaction resulting in changes in the electronic energy due to the motion of the nuclei, and the last describes spin-dependent contributions.

The second approximation further simplifies Eq. (1). Neglecting the nuclei motion in the second term, the first term in Eq. (1) can be simplified by considering the motion of each electron subject to an average potential $V(\boldsymbol{r})$ which contains the electron-electron and electron-nuclei interactions. The Hamiltonian for a single electron is thus given below:

$$H = \frac{p^2}{2m_0} + V(\boldsymbol{r}), \quad (2)$$

where the first term models the kinetic energy of a single electron depending on the momentum operator p and the rest mass m_0.

Bloch's theorem [19, 20] is used to construct the wavefunctions according to the periodicity of the crystal as follows

$$\psi_{n,k} = u_k(\boldsymbol{r}) \exp(i\boldsymbol{k} \cdot \boldsymbol{r}), \quad (3)$$

where the first function, labelled by a wavevector k, models the wavefunction within the unit cell and has the crystal's periodicity. This is modified by the exponential to incorporate the crystal's translational symmetry.

The Hamiltonian must be further modified to model the crystal in an excited state. The first term in Eq. (2) represents the kinetic energy of a free electron in vacuum. In a crystal, the electron motion is modified by the influence of the crystal potential and the interaction with other electrons. The energy dispersion is approximately parabolic near the bottom of the conduction band $E_c(k)$ and top of the valence band $E_v(k)$ as below,

$$E_c(k) = \frac{h^2k^2}{2m_e^*} + E_g \tag{4}$$

$$E_v(k) = -\frac{h^2k^2}{2m_h^*}, \tag{5}$$

where the momentum operator was replaced by the product of Planck's constant, h, and the wavevector. Eq. (4) and (5) consider the excited charge carriers as freely moving particles and incorporate the crystal potential and the interactions with the other electrons into effective masses for the electrons (m_e^*) and holes (m_h^*). The effective masses depend on properties specific to the material, such as the crystal structure, chemical composition, and bonding energies.

In the excited state, the electon-hole pairs can form bound states called excitons. The mutual Coulomb attraction between the electron and hole, screened by the dielectric material between them, is consequently added to the Hamiltonian in the third term below,

$$H = H_e + H_h - \frac{e^2}{\varepsilon\,|\boldsymbol{r_e} - \boldsymbol{r_h}|} + V \tag{6}$$

The first and second terms are kinetic energies from the conduction and valence bands, respectively. The last term incorporates additional interaction potentials. Note that this is not the same term $V(\boldsymbol{r})$ shown in Eq. (2).

2.2. Energy levels in core/shell quantum dots

The simplest case for exciton states in nanocrystals is examined, in which the conduction and valence bands have parabolic dispersions and are doubly degenerate with respect to spin. The Hamiltonian describing the exciton in the cQD is described by modifying Eq. (6) as follows [21],

$$H = \frac{-\hbar^2}{2m_e^*}\nabla_e^2 + \frac{-\hbar^2}{2m_h^*}\nabla_h^2 + \frac{-e^2}{\varepsilon|\boldsymbol{r_e} - \boldsymbol{r_h}|}\nabla_h^2 + V_e + V_h \tag{7}$$

where the first two terms are the one-particle Hamiltonians of the conduction and valence bands, respectively, and the third is the Hamiltonian representing the Coulomb interaction between the electrons and holes screened by the dielectric material between them. The last two terms come from the term V in Eq. (6); they represent confinement potentials on the charge carriers due to dimensions on the order of the exciton Bohr radius. Note that Eq. (7) ignores additional contributions such as spin-orbit coupling and polarization effects from the dielectric mismatch between the cQDs and the surface.

The geometry of the core/shell cQD can be modeled as a FDSW as follows

$$E_g^{(s)} = E_g^{(c)} + V_{oe} + V_{oh}, \tag{8}$$

where $E_g^{(c)}$ is the band gap energy of the core, $E_g^{(s)}$ is that of the shell, and V_{oe} and V_{oh} are the respective electron and hole confining potentials. As the electrons and holes are strongly confined, their mutual Coloumb interaction shown in Eq. (7) can be neglected from the FDSW model. Thus, the PL emission frequency of the cQDs is strongly dependent on both its core and shell properties.

As the electrons and holes are strongly confined, they are treated as individual particles with their own confining potentials as follows:

$$V_e = \begin{cases} -V_{0e}, & 0 \le r_e, r_h < a \\ 0, & a \le r_e, r_h < \infty \end{cases} \tag{9}$$

$$V_h = \begin{cases} V_{0h}, & 0 \le r_e, r_h < a \\ 0, & a \le r_e, r_h < \infty \end{cases}, \tag{10}$$

where a is the radius of the core. The core and shell confinement potentials are illustrated in relation to their band gap energies in Fig. 2.1. The dashed lines within the potential wells are the cQD's valence and conduction band offsets resulting from the confinement potential. For strong confinement, the kinetic energy terms are dominant and the Coulomb potential is thus ignored for this derivation. Note that this potential could be added as a perturbation.

The time-independent Schrödinger equation for the electron is as follows:

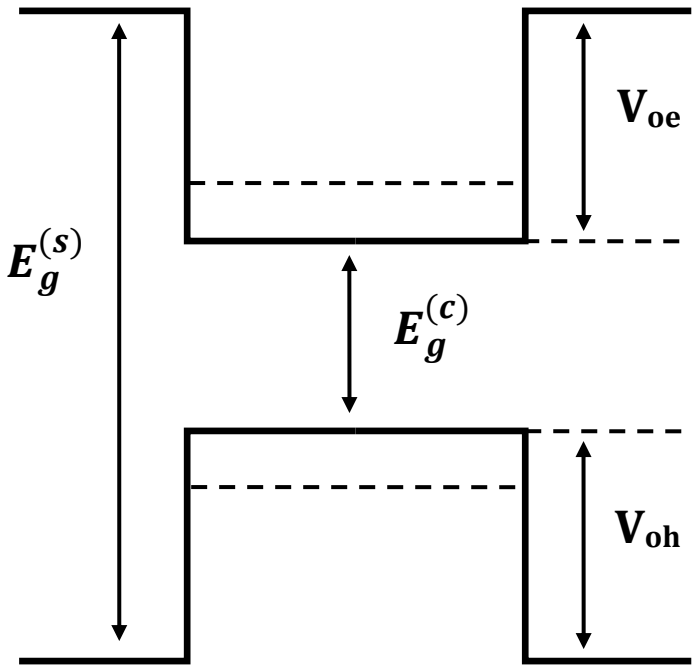

Fig. 2.1: FDSW model for cQD with core band gap energy $E_g^{(c)}$, surrounded by matrix with band gap energy $E_g^{(c)}$, and having confined potentials V_{0e} of electrons and V_{oh} of holes. Figure adapted from [21].

$$\left\{\frac{-\hbar^2}{2m^*}\nabla_e^2 + V_e\right\}\psi = E\psi. \tag{11}$$

Transforming to spherical coordinates and applying the separation of variables technique yields a Schrödinger equation with two separable parts: a radial and angular equation. As the confining potentials are spherically symmetric, they only affect the radial Schrödinger equation, shown below [20,22]:

$$\frac{1}{\rho^2}\frac{d}{d\rho}\left(\rho^2\frac{dR}{d\rho}\right) + \frac{2m^*(E-V)R}{\hbar^2} = l(l+1)\frac{R}{\rho^2} \tag{12}$$

where $l(l+1)$ is the separation constant.

This equation yields solutions for two different regions: (1) $\rho < a$ and (2) $\rho > a$. The electron energy states are examined.

(1) For $\rho < a$, $V = -V_{0e}$:

$$\rho^2 \frac{d^2R}{d\rho^2} + 2\rho \frac{dR}{d\rho} + [(\beta\rho)^2 - l(l+1)]R = 0, \tag{13}$$

where

$$\beta^2 = \frac{2m_c^*}{\hbar^2}(E + V_{0e}) > 0. \tag{14}$$

This has the form of a spherical Bessel differential equation [23,24], with solutions that are a linear combination of spherical Bessel functions of the first and second kind.

(2) For $\rho > a$, V = 0:

$$\rho^2 \frac{d^2R}{d\rho^2} + 2\rho \frac{dR}{d\rho} - [(\alpha\rho)^2 + l(l+1)]R = 0, \tag{15}$$

And

$$\alpha^2 = \frac{-2m_s^*}{\hbar^2}E > 0. \tag{16}$$

This equation has the form of a modified spherical Bessel differential equation [24] whose solutions are a linear combination of modified spherical Bessel functions of the first and second kind.

For simplicity, the ground state, l = 0, is considered. This yields the following two solutions:

$$R(\rho) = A\frac{\sin(\beta\rho)}{(\beta\rho)} + B\frac{\cos(\beta\rho)}{(\beta\rho)}, \quad \rho < a \tag{17}$$

$$R(\rho) = C\frac{\sinh(\alpha\rho)}{(\alpha\rho)} + D\frac{e^{-\alpha\rho}}{(\alpha\rho)}, \quad \rho > a. \tag{18}$$

Boundary conditions are now imposed for Eq. (17) and (18). The first is to set B=0 in Eq.

(17), because otherwise, $\frac{\cos(\beta\rho)}{(\beta\rho)} \rightarrow -\infty$ as $\rho \rightarrow 0$. The second is to set C=0 in Eq. (18), because otherwise $\frac{\sinh(\alpha\rho)}{(\alpha\rho)} \rightarrow \infty$ as $\rho \rightarrow \infty$. This yields the following two expressions:

$$R(\rho) = A\frac{\sin(\beta\rho)}{(\beta\rho)}, \quad \rho < a \tag{19}$$

$$R(\rho) = D\frac{e^{-\alpha\rho}}{(\alpha\rho)}, \quad \rho > a \tag{20}$$

Furthermore, the wavefunction and its derivative must be continuous at the interface between the dot and the shell. This is known as the BenDaniel-Duke boundary condition [25]: ψ and $\frac{1}{m^*}\frac{\partial R}{\partial \rho}$ are continuous at $\rho = a$, where m^* is the effective mass of the charge carrier in the medium. These two conditions yield the following transcendental equation:

$$\frac{m_c^*}{m_s^*}(1 + \alpha a) = 1 - \beta a \cot(\beta a) \tag{21}$$

Knowing the effective masses for the core and shell, Eq. (21) can be solved for α and β, and the electron energy states can be consequently solved. A similar analysis can be done to derive the hole states. The following table shows literature-reported values for electron and hole effective mass values for CdSe [26], CdS [26], and ZnS [27], where m is the free electron mass.

Table 1: Literature-reported electron and hole effective mass values

	m_e^*	m_h^*
CdSe	0.13m	0.3m
CdS	0.18m	0.53m
ZnS	0.42m	0.61m

2.3. Photoluminescence pump intensity dependence

This section discusses the QDs' PL dependence on PI. Two possible types of behaviour may be observed if the PI is varied over an appropriate range: a linear dependence of PL for sufficiently low PIs and a saturation for sufficiently high PIs. These two regimes are defined by the lifetime of the state being pumped, which is in turn defined by the rate of recombination of the excited charge carriers, with respect to the magnitude of the PI, or the pumping rate. In this thesis, only transitions between the ground and first excited state were studied.

In the linear regime, the rate of excitation from the ground state to the first excited state is less than the rate of recombination, so that there are always available states for an excited electron. The measured intensity can be determined as follows [28]:

$$N = D\eta\Sigma P \tag{22}$$

where N is the detected PL power, D is the efficiency of detecting the PL, η is the quantum efficiency, Σ is the absorption cross section of the sample, and P is the intensity of the pump beam. The sample's absorption cross section, assuming non-interacting QDs, is given as follows:

$$\sum = n'\sigma, \tag{23}$$

which depends on the number of QDs pumped, n', and the absorption cross section σ of a single cQD.

Once the rate of pumping becomes larger than that of recombination, the excited state becomes saturated with charge carriers and any further increase of PI will not increase PL. The detected signal in this regime is [28]:

$$N = \frac{D\,\eta}{\tau}, \tag{24}$$

where τ is the lifetime of the excited state.

Using Eq. (22) through (24), the cQD's quantum efficiency and lifetime can be calculated by measuring the PL response as a function of PI if the experimental system's detection efficiency and the sample's absorption cross section are predetermined.

2.4. Photoluminescence temperature dependence

The QDs' PL properties, including the band gap and spectral width, change with temperature. The change in the material's band gap can be modeled with the Varshni equation, which has also been shown to apply to QDs [29] as follows:

$$E_g(T) = E_{g0} - \alpha \frac{T^2}{T+\beta}. \tag{26}$$

Note that α and β in this equation are not the same parameters used in Eq. (14) and (16), but are used because of convention. Eq. (26) is an empirical formula developed by Varshni [30] to model the temperature dependence of the band gap energy $E_g(T)$ of a semiconductor material. The equation has three parameters: E_{g0} is the band gap of the material at 0 K, α is the temperature coefficient, and β is related to the Debye temperature θ_D of the material.

The thermal broadening can be modeled by the following equation:

$$\Gamma(T) = \Gamma_{inh} + \sigma T + \frac{\Gamma_{LO}}{e^{\frac{E_{LO}}{k_B T}} - 1}, \tag{27}$$

which describes excitonic peak broadening in semiconductors and has been shown to work for QDs [29]. In this equation, the full width at half maximum (FWHM) of the spectrum, Γ, is a function of temperature, T. There are four parameters: Γ_{inh} is the inhomogeneous broadening coefficient, σ is the exciton-acoustic phonon coupling coefficient, Γ_{LO} is the exciton- longitudinal optical (LO) -optical phonon coupling coefficient, and E_{LO} is the LO-phonon energy. Boltzmann's constant is k_B.

2.5. Photoluminescence instability phenomena

Absorption of a photon in a semiconductor may not always be followed by radiative recombination of the photogenerated electron-hole pair. Semiconductor nanocrystals have various structural features, including their surface chemistry, that can cause different phenomena upon interaction with light. This section discusses the various types of non-radiative processes that can occur in cQDs and the resulting instabilities that appear in their PL, such as fluorescence intermittency (FI) or blinking, PL enhancement (PLE), PL decay, quenching, or bleaching, spectral diffusion or wandering, and spectral bluing. The causes of these phenomena are not completely understood, however, countless experimental observations and theoretical models provide insight into the photophysical dynamics of the cQDs. Photobleaching phenomena was observed in the PL of the cQDs, shown in the results in Chapter 4, so this section provides some background on the origin of this behaviour.

The PL under continuous optical pumping of a state may exhibit periods during which there is not any light emission from the sample. In this case of FI, the PL intermittently switches between "bright" and "dark" states, or it blinks "on" and "off". FI was initially found by Nirmal et al. in 1996 on individual CdSe cQDs [31]. To date, this phenomenon has been observed in cQDs under different conditions, and analyses of the timescales of the "on" an "off" PL trajectories have shown to commonly follow an inverse power law with time. Variations in these "on" and "off" rates, however, have been observed under different conditions, such as differing cQD structure and environment [10].

During the dark states the cQD is believed to be ionized, during which radiative recombination processes are not favourable. The cQD is ionized by trapping of a photo-excited charge carrier at the core/shell interface, within the shell material, on the cQD surface, or in the surrounding matrix/environment. The emission from a following electron-hole pair is transferred to eject the trapped carrier from the system, resulting in no net photon emission. After the cQD becomes neutralized, it can continue to emit radiatively. This three-carrier non-radiative process is Auger recombination. A charge carrier must overcome an energy barrier to be ejected from the crystal. The Auger process reduces the energy barrier for thermal escape. It is also possible for a carrier to tunnel into a trap state.

Blinking behaviour has also been studied for cQDs in different environments, such as different polymer matricies and gaseous atmospheres [32]. In a gaseous oxygen

environment, shorter on times have been observed which were hypothesized to be a result of oxygen molecules binding to the surface of the cQD which could trap electrons created by an Auger process. It has also been noted that electron-donating ligands or trap sites from incompletely passivated surfaces can affect the blinking kinetics.

Other unstable PL processes are PLE and PL decay. Under continuous optical pumping of a cQD ensemble, the former is an increase and the latter is a decrease in observed PL intensity [32]. A constant cycle of PL decay followed by PLE has commonly been observed in cQDs. PLE can occur in bulk semiconductors having a layer of defects ~ 100 nm from the surface, however, cQDs have a different cause for this phenomenon. PL decay is commonly a cause of photo-induced oxidation of the cQDs.

A possible PLE mechanism is adsorption of water molecules from the environment, which passivates the surface and results in a PL increase; subsequent oxidation processes decrease PL. Another cause is a photoinduced electron-donating ligands, which can migrate to trapped holes in the crystal. PLE has been observed in all types of cQDs: core, core/shell, polymer coated, and bioconjugated. Because PLE is a reversible process, it is difficult to distinguish detection of the different types of mechanisms that can occur.

The phenomenon of PL quenching, or bleaching, is examined in this thesis. Photobleaching is the creation of nonradiative decay channels with optical pumping. This can be either a reversible or non-reversible process. An example of creation of a nonradiative decay path is by photo-induced damage of the structure by breaking a bond in the material. This can serve as a trap site for excited charge carriers and thus PL reduces. Note that the term "damage" implies a physical change in the material's structure, while "bleaching" is a reduction in PL due to an increase in non-radiative decay.

Two final types of PL instabilities are spectral diffusion and bluing which appear in the PL spectrum FWHM. The spectral width from a cQD ensemble is partly due to thermal broadening, which is homogeneous [19]. Inhomogeneous broadening due to the cQD size distribution is also present. Moreover, instabilities in the FWHM can be observed due to random shifts in the peak energy and linewidth of individual dots. Spectral diffusion is a reversible process involving fluctuations of the peak position, while non-reversible blueshifting of the spectrum can also occur [32,19].

Because spectral wandering is reversible, it is not caused by photoinduced chemical modifications within the dot or on the surface. These shifts have been found to be temperature independent, but the amount of shift depends on excitation frequency and intensity. This phenomenon is believed to be caused by a quantum confined stark effect (QCSE), in which a photoinduced localization of charges occurs at the core/shell interface or at the cQD surface forming an electric field that perturbs the electron and hole energy levels. Furthermore, the electronic configuration can be redistributed by charge-hopping between trap sites.

Spectral bluing, an irreversible blue shift in the PL emission wavelength, is believed to be a photo-oxidation process which reduces the cQD size. An observation in FWHM may be due to a complete reduction of the smaller cQDs, while a recover in width may be due to the differing oxidation rates in the larger cQDs [32,19]. Capping the cQDs with an inorganic shell can reduce the rate of photooxidation; however, incomplete capping can result in grain boundaries through which oxygen can diffuse.

Although much work has been done on fabricating cQDs to minimize these PL instabilities, there has also been large interest in better understanding these phenomena to exploit them in various applications. Because the cQDs can be sensitive to their environment, they can be used as chemical or biological sensors to detect, for example, the concentration of free anions in an aqueous environment or the pH, while the reversibility of PLE allows for creating a rewritable cQD film.

Chapter 3 Experimental methods

This chapter discusses the experimental approach used for characterizing the nanocrystals. Over the course of data collection, from preliminary measurements showing qualitative behaviour to later and more quantifiable measurements, both the sample preparation process and the experimental setup were developed. The first part of this chapter discusses the different sample preparation techniques that were used. The second part describes the PL spectroscopy setup that was built to study the samples.

3.1. Sample Preparation

3.1.1. Introduction

This section introduces the original batch of cQD samples suspended in a hexane solution. Four different samples are then described that were prepared by casting the cQDs from the solution onto glass substrates for experimental study by one of three different techniques: drop cast, spin coat, and "drop and drag".

The cQD samples are CdSe/$Cd_{0.5}Zn_{0.5}S$ core/shell structures fabricated by Dr. Claudine Allen's group at Université Laval. The cores, created by solution-phase synthesis, were nucleated in a high temperature organic solvent following injection of precursors. A successive ion layer adsorption and reaction (SILAR) method [9] was used to fabricate 7-monolayers of the shells onto the 4-nm-average diameter cores. The core size was measured from absorption spectra. This resulted in ~ 8.6 nm diameter particles, which were subsequently capped with oleic acid and oleylamine ligands and suspended in hexane. These ligands, which can be very dynamic in air, extend to ~1-1.5 nm from the shell surface. The final estimated diameter of the cQDs is ~ 9.6-10.1 nm. The cQD samples were all used from the sample batch, having an estimated concentration of 20 μM in the solution. The properties of these samples are summarized in Table 2.

Table 3 highlights the aspects of each sample prepared for PL experiments, labelled "Sample 1" through "Sample 4", for easy comparison. Samples 1 and 2 were prepared for initial trials with less control of the cQD distribution. Measurements on these samples,

however, gave sufficient qualitative information about the cQDs to guide further work. Samples 3 and 4 were prepared under more controlled conditions and were thus used to obtain more quantitative information about the QDs.

Different substrate and QD solution preparation mechanisms were employed for each of the samples. One of the first samples created was Sample 1 using a drop casting technique. This produced a very non-uniform QD distribution, so a different technique of spin coating was investigated and Sample 2 was created. This slightly improved the cQD uniformity, but to achieve a reasonably uniform distribution, the QDs were spin coated in a polymethyl acrylate (PMMA) film in Sample 3. To compare the PL properties of Sample 3 with one in which the QDs were not embedded in PMMA, Sample 4 was created using a drop and drag technique to attain a better dot distribution than the distribution produced by the basic drop casting technique.

Table 2: cQD sample properties

Core	CdSe
Shell	$Cd_{0.5}Zn_{0.5}S$
Ligands	Oleic acid & oleylamine
Solvent	Hexane
Original cQD concentration in solvent (µm)	20
Core diameter (nm)	4
Shell outer diameter (nm)	8.6
Approximate extent of ligands in air* (nm)	1-1.5
Total diameter of cQD particle (nm)**	9.6 – 10.1

* Ligands can be very dynamic in air and their length is approximated.

** For calculated values in Table 3 of the prepared samples, the cQD diameter used includes the ligands' extent.

3.1.2. Overview of cQD casting techniques

This section compares the three different techniques used for casting the nanocrystals from colloidal suspension in the solvent onto glass substrates.

(1) Drop casting

Table 3: Properties of prepared cQD samples

Sample	Substrate	Substrate prep	cQD prep	Casting technique	cQD matrix	Substrate surface area (m^2)	cQD solution concentration (µM)	cQD solution volume (µL)	Prepared sample: cQD concentration (mol/L)	Prepared sample: number of cQDs	cQD density (QDs/m^2)	Number of monolayers*	Sample thickness** (µm)
1	Soda lime glass	None	None	Drop	Substrate	1.94×10^{-4}	NA	NA	NA	NA	NA	NA	NA
2	Soda lime glass	Acids	Excess ligands removed, Changed solvent	Spin coat	Substrate	1.94×10^{-4}	NA	50	NA	NA	NA	NA	NA
3	Quartz	Soap, Acids, H2O, Oven	Excess ligands removed, Changed solvent	Spin coat	PMMA	8×10^{-5}	2	50	1×10^{-10}	6.02×10^{13}	7.5×10^{17}	69.3-76.8	0.665-0.776
4	Quartz	Soap, H2O	Ultrasonic bath	Drop and drag	Substrate	8×10^{-5}	2	500	1×10^{-9}	6.02×10^{14}	7.5×10^{18}	693-768	6.65-7.76

* The number of monolayers was found by first estimating the cQDs as cubes. The surface area of one face of the cube was found and multiplied by the number of cQDs on the slide. This total cQD area was divided by the substrate surface area to find the number of monolayers (Number of monolayers = ((Number of cQDs) * (surface area of one cQD)) / (Substrate surface area)).

** Sample thickness = (Number of monolayers) * (cQD diameter)

The most basic technique is drop casting. A drop of the solution is placed on the substrate and the cQDs settle onto the slide as the solvent evaporates. The downside encountered when using this technique is that the solvent containing the cQDs, hexane, has a high volatility and left an extremely non-uniform distribution of dots on the slide. The sample exhibited large QD concentration gradients which was not desirable for experimental analysis.

(2) Spin coating

Spin coating is a common technique used for creating uniform thin films on substrates. A volume of the solution is initially dropped onto the slide which is rotated at a specified speed and time period. By adjusting the sample volume, concentration, rotation speed, and rotation time, the QD distribution can be tuned. A reasonably uniform dot distribution was found with this method by embedding the QDs in a PMMA film on the substrate.

(3) Drop and drag

"Drop and drag" is a modified drop casting technique that was developed in this work in attempt to produce uniform cQD distributions without embedding them in polymer films. A drop of the solution was placed on the slide and a flat edge of another slide was used to drag the solution across the surface. The solvent's volatility and the substrate's small surface area, however, limited the ability to control the distribution of QDs. This technique needs to be further investigated to produce samples of comparable QD uniformity to those embedded in PMMA via spin coating.

3.1.3. Substrate preparation

Table 3 shows that two different types of substrates were used for preparing samples. Samples 1 and 2 were prepared on microscope slides made of soda lime glass. Samples 3 and 4, on the other hand, were prepared on quartz or UV fused silica substrates. Both types of substrates were circular; the soda lime slides had a diameter of 15.7 mm while the quartz slides had a diameter of 10 mm. As sample preparation techniques were further investigated, fused silica substrates were chosen as fluorescence was observed from the less costly soda lime glass slides during PL experiments.

Before preparing QD samples, the substrates were cleaned as described below.

Sample 1:

The soda lime substrate for Sample 1 was not cleaned before preparing the sample.

Sample 2:

The soda lime substrate for Sample 2 was rinsed with ethanol, chloromethanol, and acetone and was dried with compressed air.

Sample 3:

For Sample 3, a thorough process was used to clean a number of fused silica substrates. A 500 mL beaker was filled with a mixture of a general laboratory cleaning detergent (Cole-Parmer Micro-90 cleaning solution) and distilled water. The slides were placed into the beaker on a special holder and the beaker was then placed into an ultrasonic bath for ~ 6 minutes to facilitate the cleaning process.

After ultrasonication, the soap mixture was drained from the beaker. The beaker containing the holder and slides was placed under a running tap of distilled water for 3-4 minutes to remove the soap. Another beaker was filled with ~ 400 mL of acetone. The slides on the holder were lowered into the beaker and the beaker was placed in an ultrasonic bath for another 6 minutes. A final beaker was filled with ~ 400 mL of isopropanyl. The slides on the holder were placed into this beaker and were sonicated for 6 minutes. Because isopropanyl dries very quickly, a mechanical device was used to slowly raise the slide holder out of the beaker to prevent streaking the slides. The slides were then placed in an oven for over an hour and were left to cool before spin coating.

Sample 4:

Due to time constraints, the substrate for Sample 4 was cleaned less vigorously than the one for Sample 3. The UV fused silica substrate was rinsed in a beaker containing a solution of deionised water and detergent. The slide was then rinsed three times in deionised water.

3.1.4. Preparation of samples

All of the samples were prepared from the same batch of $CdSe/Cd_{0.5}Zn_{0.5}S$ cQDs. They were suspended in a solution of hexane with an estimated dot concentration of 20 μM.

Sample 1:

For Sample 1, a drop of an unknown concentration of the solution was placed on the soda lime glass substrate. The solution was taken from a vial of the batch that had been used on a number of previous occasions, and the solvent had evaporated and been refilled many times.

Sample 2:

For Sample 2, a QD solution of unknown concentration (for the same reasons as in Sample 1) was spin coated on the soda lime glass substrate. Since excess ligands hinder the flow of cQDs during spin coating, the cQDs tend to agglomerate and leave a non-uniform distribution on the substrate. Moreover, the volatility of hexane causes rapid flow of the QDs even at moderate to low rotation speeds. The combination of excess ligands and the rapid flow of hexane can produce a very non-uniform sample.

To achieve a more uniform sample upon spin coating, a centrifuge was used to remove excess ligands from the cQDs and to change the solvent to a less volatile one of chlorobenzene. This was done by placing a mixture of 200 µL of the cQDs supended in hexane with 600 µL isopropanyl in a centrifuge at 13,370 rpm (~20,000 rcf) for 5 minutes. Because the QDs are not soluble in isopropanyl, this resulted in precipitation of the cQDs on the sides of the tube, while the solution of excess ligands and isopropanyl was emptied from the tube. Next, 200 µL of chlorobenzene was added to the tube and shaken by hand to suspend the cQDs. To ensure sufficient removal of ligands, the above process was repeated in which 600 µL of isopropanyl was added and the mixture placed in the centrifuge under the same conditions as above. The resulting solution was drained from the tube, and another 200 µL of chlorobenzene was added and was shaken by hand to suspend the cQDs in chlorobenze. This tube was then placed in an ultrasonic bath for 1-2 minutes to ensure all of the QDs were suspended in the solution. A 50 µL volume of the prepared QD solution was pipetted onto a soda lime glass slide, prepared as in Section 4.2.3, and was spin coated at ~2,000 rpm for 30 seconds.

Sample 3:

Sample 3 was prepared by spin coating the cQDs in a similar manner as Sample 2. In this case, the excess ligands were removed and the cQD solvent was changed to a mixture of toluene and PMMA. The procedure of removing excess ligands from 200 µL of the original solution described for Sample 2 was performed, with re-suspension of the QDs in hexane before the second removal of excess ligands. The remaining QDs in the centrifuge tube were mixed with 200 µL of toluene and was shaken both by hand and in a vortex mixer for 1-2 minutes.

The QDs solution was divided into two parts so that spin coating could be tested with both the QDs suspended in toluene and suspended in a mixture of 2.5 % weight of PMMA

in toluene. A 100 μL quantity of the solution was pipetted into a tube labelled "P" indicating the one for the PMMA/toluene solution, and the remaining tube with 100 μL of the QD solution was labelled "T" indicating the one with just toluene.

To change the solvent, 600 μL of isopropanyl was added to each tube and they were placed in the centrifuge at 2,000 rcf for 5 minutes. The excess solution was discarded. To each tube P and T, 1 mL of the tolunene/PMMA and toluene solutions were respectively added so that the QD concentration was reduced by a factor of 10. Each of the P and T tubes were relabelled "P1" and "T1" respectively to indicate the dilution by 10^1. Each tube was shaken with a vortex mixer for ~1-2 minutes and then placed in an ultrasonic bath for 5 minutes to ensure the QDs were evenly suspended.

Dilutions of the QDs by a factor of 10^2 of the original concentration, labelled P2 and T2, were created by taking 100 μL of P1 and T1, respectively, and 900 μL of the corresponding solvent. Each tube was then shaken with a vortex mixer for ~1-2 minutes and then placed in an ultrasonic bath for 5 minutes.

Dilutions of the QDs by a factor of 10^3 of the original concentration, labelled P3 and T3, were created in a similar manner using 100 μL of P2 and T2 and 900 μL of the respective solutions. Each tube was then shaken with a vortex mixer for ~1-2 minutes and then placed in an ultrasonic bath for 5 minutes.

First, trials of spin coating each sample were done on ordinary glass slides. The details, including fluorescence microscope images showing the dot distribution, are discussed in Appendix C. The results showed that the QDs embedded in the polymer film produced the most uniform distribution.

This solution was placed in an ultrasonic bath for 30 minutes before preparing Sample 3 by spin coating ~40-50 μL of the P1 solution onto a UV fused silica slide at 3,000 rpm for 1 minute. .

Sample 4:

Sample 4 was prepared using the drop and drag technique on a UV fused silica slide. The original batch of approximately 20 μM of cQDs was used to create a solution about ten times less concentration by transferring 100 μL of the original QD solution and nine repetitions of 100 μL of hexane into the new vial. This vial was placed in an ultrasonic bath for about ten minutes to separate aggregated QDs.

About 10-15 drops of the solution were placed onto the slide. The solution was dragged after each drop was placed on the slide. As this was one of the first times this technique was performed, there was not much control over the cQD distribution. The hexane evaporated quickly, leaving a much greater QD concentration on the region of the slide where the QDs were initially dropped. Due to the small substrate surface area, much of the QD solution spilled off the slide or went to the bottom of the slide. Also, many of the QDs stayed on the edge of the second slide used to drag the solution on the substrate. A photo of the prepared sample is shown in Fig. 3.1.

3.1.5. Summary

Section 3.1 described the preparation processes for four different samples, labelled Samples 1 through 4, whose attributes are listed in Table 3. The first two samples were prepared for preliminary QD measurements to gather qualitative PL information. There was little control over the final dot distribution on the substrate in these two samples, which is why the final QD density and state is unknown. Samples 3 and 4, on the other hand, were prepared with more controlled techniques. Calculations yielded estimates of a total of ~ 6 x 10^{13} QDs, forming ~ 69-77 monolayers, on Sample 3 and a total of ~ 6 x 10^{14} QDs, forming ~ 690-770 monolayers, on Sample 4. These latter two samples must therefore be QD solids, however a single particle assumption is used for the sample's absorption cross section to determine the quantum efficiency of the cQDs in Chapter 4.

While estimates for cQD densities used for Samples 1 and 2 could not be determined, they were determined for Samples 3 and 4, because during preparation of these samples, all quantities such as solution concentrations and volumes that were used and transferred between each intermediate step were carefully recorded. Given that the sample preparation was a wet chemistry process, however, there are likely large uncertainties in the calculations. An uncertainty in the preparation of Sample 3 is that the amount of the QD solution that spilled off the slide during the spin coating process was unknown. A similar uncertainty in the preparation of Sample 4 is that the amount of QDs that spilled off the slide or adhered to the second slide used to drag the solution was unknown. Moreover, the substrate used to prepare Sample 4 was not cleaned thoroughly, so the QDs may not have adhered to the slides as well as in Sample 3. There are also uncertainties in the original

Fig. 3.1: Photo of Sample 4 under illumination with UV light.

batch of QDs, which was about a year old when preparing Samples 3 and 4. Although the vial in which the QDs were stored was sealed with parafilm, the hexane solution has been observed to evaporate over time. It is also unknown whether some of the cQDs adhered to the inner glass walls of the vials.

Furthermore, there may have been many aggregates and clumping of QDs which shaking or ultrasonication did not remove. The variation in the QD distribution over the substrate is therefore unknown. This uncertainty is particularly prevalent in Sample 4, as it was noted that many of the QDs immediately settled onto the area where they were initially dropped on the slide before they were dragged across the slide. The final estimate of the number of QDs on the slides, therefore, should be treated as a hard upper limit. As this number is inversely proportional to the quantum efficiency as discussed in Chapter 2, a low quantum efficiency value is expected. The resulting calculation of quantum efficiency in Chapter 4 is therefore merely illustrative of the procedure, rather than quantitative assessments.

3.2. Photoluminescence spectroscopy setup

Optical spectroscopy is a common technique used for characterising a material's energy levels. It involves irradiating the material with light – either UV, visible, or NIR – having sufficient energy to excite electronic transitions. If the system relaxes from an excited state to the ground state radiatively, i.e., by emitting light, this phenomenon is called PL. The

luminescent light is studied in the form of a spectrum showing the intensity distribution as a function of frequency or wavelength [33]. These frequencies correspond to energy values that describe the material's band structure.

Section 3.2.1 describes the experimental PL spectroscopy setup. Section 3.2.2 discusses the two types of experimental configurations used to study different types of PL measurements. Section 3.2.3 follows with a discussion of the spectrometer and its settings for collecting data.

3.2.1. Apparatus and alignment

Fig. 3.2 shows the experimental setup. A laser is used to excite, or pump, the sample which is mounted in a cryostat. Luminescence is collected from the sample and is focused onto the entrance slit of a spectrometer. The laser is positioned so that its specular reflection is not directed into the spectrometer. The spectrometer uses a diffraction grating to split the light into its constituent wavelength components and images the spectrum with a multichannel detector.

Throughout the course of measurements, two different cryostats were used. The layout of the components in Fig. 3.2 accommodates the geometry of an older cryostat used for preliminary measurements of Samples 1 and 2 in which the laser was incident at 90° to the sample surface and luminescence was collected at 45°. The layout using a newer cryostat (CIA model ND 110H) used to collect data from Samples 3 and 4 is shown in Fig. 3.3. In this configuration, the laser was incident at ~18.9° to the sample surface and luminescence was collected perpendicular from the opposite side of the sample.

Fig. 3.4 and Fig. 3.5 are photos of the later PL setup containing the newer cryostat and within an enclosure to ensure laser safety protocols. The first photo shows the laser with an electric shutter directly in front of its aperture. A neutral density filter wheel follows, and the beam is subsequently directed to the second part of the enclosure by a mirror, located by the back wall, through a hole on the left wall. In the second part of the enclosure, shown in Fig. 3.5, the beam is directed by a mirror, on the right, to the sample in the cryostat. Luminescence is collected on the left from the cryostat and is consequently directed to the spectrometer's entrance slit, located on the left of the enclosure.

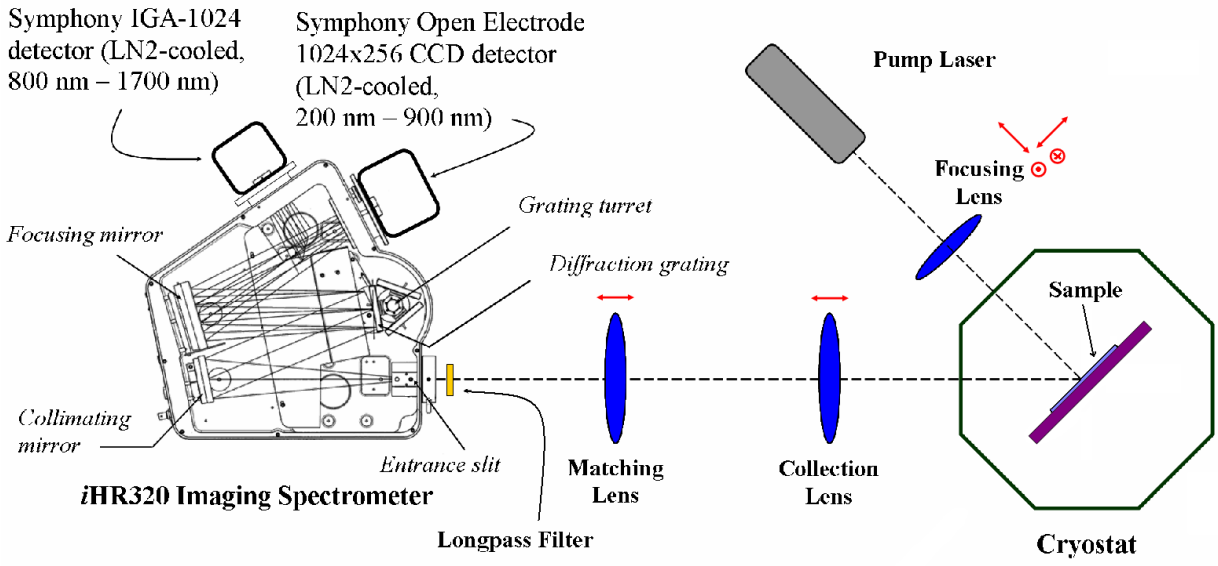

Fig. 3.2: PL spectroscopy experimental setup. Spectrometer image courtesy of Horiba Jobin Yvon [34]. The degrees of freedom in adjustment of the three lenses during alignment of the setup are labelled above the lenses.

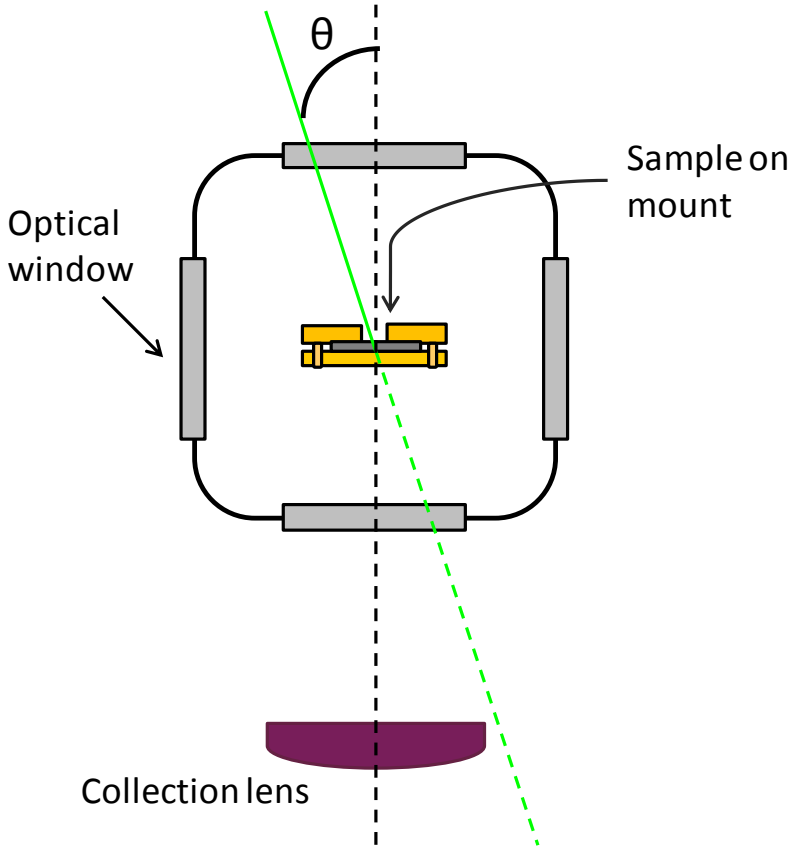

Fig. 3.3: Diagram of pump beam impinging sample in alternate cryostat (CIA model ND 110H) used for PL measurements on Samples 3 and 4. Pump beam is not collected by collection lens.

Fig. 3.4: Photo of pump laser (front of photo) in PL setup. An electric shutter and neutral density filter wheel are subsequently placed in front of the laser's aperture. A mirror (located by back wall) directs the laser to the sample through a hole in the left wall of the enclosure.

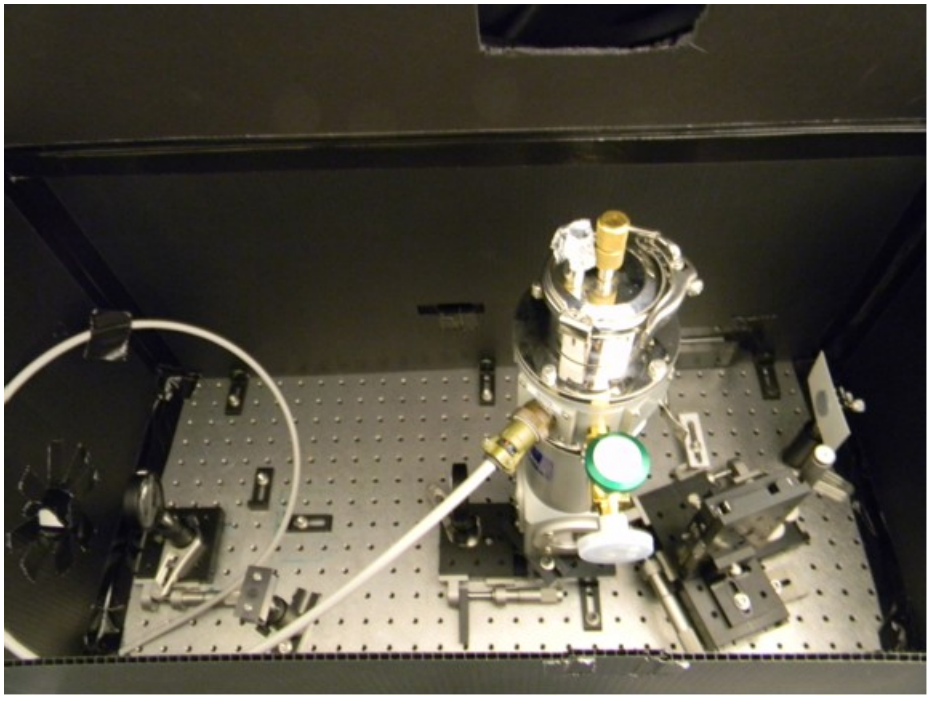

Fig. 3.5: Photo of cryostat in PL setup. Pump beam enters from hole in back wall after reflection off mirror in Fig. 3.4. The beam is directed from the mirror on the right and into the entrance window of the cryostat. PL is collected with a collection lens from the cryostat exit window and is focused onto the entrance slit of the spectrometer at the left of the photo.

A description of each component in Fig. 3.2 follows. A calculation and measurement of the efficiency of detecting light emitted from the sample and transmitted through the entire system to the CCD detector is shown in Appendix B.

(1) Pump Laser

A 500 mW frequency doubled Nd:YAG diode-pumped solid state (DPSS) laser from Dragon Laser was used to pump the sample. Its active medium is a yttrium aluminum garnet (YAG) crystal doped with Nd^{3+} ions. This crystal is pumped by near-infrared emission from a semiconductor diode laser to produce a 1064 nm laser line. This beam then passes through a nonlinear frequency-doubling crystal to produce the output laser line at 532 nm.

The laser was mounted on a lab jack so that the beam height could be adjusted to the height of the spectrometer entrance slit during initial alignment of the setup. This height was not adjusted once the PL setup was installed.

The power of the laser was adjusted between 0.3-380 mW by changing neutral density (ND) filter combinations on a New Focus 5215 dual filter wheel. This filter wheel, positioned directly after the laser aperture, was aligned with the setup and was not removed once installed. The laser power values through each ND filter combination were calibrated with a Newport 918D-SL-OD3 silicon photodiode detector and a Newport 842-PE optical power meter.

An electric shutter was installed directly after the ND filter wheel. It was controlled by a switch to block and unblock the laser beam to pump the sample.

(2) Focusing Lens

For measurements at high pump intensities (~6-7,000 W/cm^2), a 75.6 mm focal length biconvex lens was used to focus the laser beam onto a spot size measured to be ~75 μm by 94 μm (see Appendix C for measurement). It was mounted on three translation stages with micrometer actuators to allow adjustment in axial, lateral, and vertical positions to align this spot with the spot of collection of luminescence.

The lower pump intensities (~0.01-10 W/cm^2) were achieved by removing this lens to excite a broader spot of ~2,120 x 2,260 μm.

(3) Cryostat

The sample was mounted in a cryostat (CIA model ND 110H) designed to allow heating and cooling of the sample between 77-500 K without condensation forming on the sample. It consists of two parts. The upper part is a double walled stainless steel liquid nitrogen (LN2) reservoir. The lower part contains the sample holder and UV fused silica optical windows. The sample is mounted on a copper cold finger to which a high power 50 ohm heater along with a platinum resistance thermometer is attached. The cold finger is also attached to the LN2 reservoir via a thermal link. This link can be adjusted to change the distance between the sample and reservoir to control cooling of the sample when the reservoir is filled with LN2. The heater works in conjunction with the LN2 to adjust the sample temperature, which is monitored with the thermometer.

The inner walls of the reservoir and the lower part of the cryostat need to be evacuated to about 1 milliTorr (0.133 Pa) before filling the reservoir with LN2 to prevent condensation on the sample and windows. A V 81-M turbo pump was used with a DS 42 oil based roughing pump as a foreline pump to evacuate the cryostat. An inverted magnetron Pirani FRG-700 gauge was used to monitor the vacuum level in the cryostat.

Each time the sample was changed or the cryostat was evacuated, the cryostat was removed from the optical table. When it was repositioned on the table, the focusing and collection lenses were readjusted. In the case that the focusing lens was not used, a mirror directing the beam into the cryostat was adjusted by the knobs on its kinematic mount.

(4) Collection Lens

The PL collection lens was a plano-convex lens with focal length of 100 mm. With its focal spot on the sample, this lens collimates the luminescence to be coupled into the spectrometer via a lens matching the instrument's f/#. The collection lens was both vertically and laterally aligned with the path of light inside the spectrometer during the initial installation of the setup. It was mounted on a translation stage with a micrometer actuator to move it along its axial direction to optimise the focus of the collection spot on the sample before collecting data.

(5) F/#-Matching Lens

The matching lens was used to focus the collimated light collected from the sample onto the entrance slit of the spectrometer while matching the f/# or the angle of the cone of light with that of the instrument's entrance optics. When this lens was initially installed, it was aligned

both laterally and vertically with the path of light inside the spectrometer. It was placed on a translation stage to adjust its axial position with a micrometer actuator to optimize the focus on the entrance slit. This adjustment was especially required when introducing extra optical components such as filters between this lens and the entrance slit.

(6) Longpass Filter

An Edmund Optics NT62-984 550 nm longpass filter was placed directly before the entrance slit to reduce the scattered 532 nm laser light entering the spectrometer. The scattered laser light was frequently much more intense than the PL, so this filter was required to avoid saturating the detector. This filter nominally allows only light with wavelengths longer than 550 nm to pass through by attenuating the shorter wavelengths. The filter's transmission curve in Fig. 3.6 shows that it has a sharp cut-off at 550 nm. It has a transmission above 95 % between 552-1650 nm.

(7) Spectrometer

The spectrometer is the instrument that spectrally disperses the PL focused on its entrance

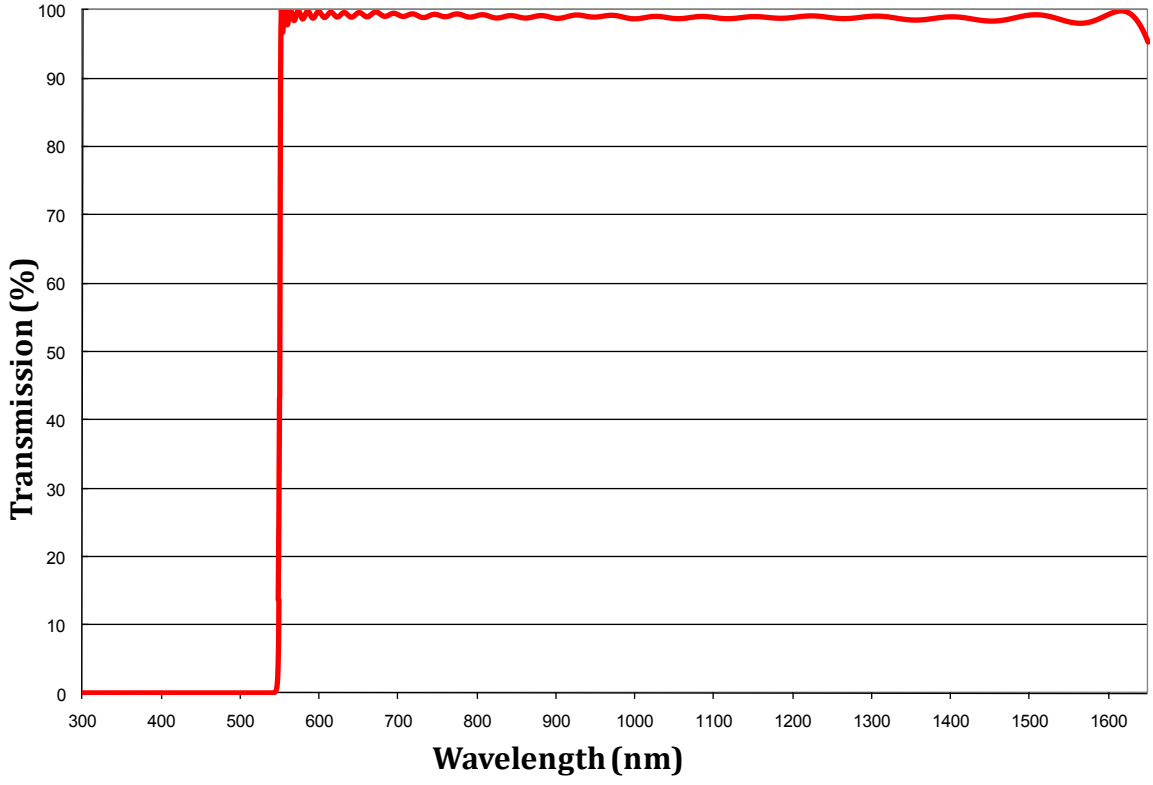

Fig. 3.6: Transmission curve for NT62-984 longpass filter. Data courtesy of Edmund Optics Inc.

slit with a diffraction grating and passes the signal to an optical detector. It is a Horiba Jobin Yvon iHR320 imaging spectrometer and its internal components are described in Section 3.2.3.

(8) CCD Detector

The spectrometer can detect the spectrum with either a silicon charged coupled device (CCD) or an InGaAs (IGA) linear array detector. The PL measurements of the cQDs were done in the visible region of the spectrum and were captured with the Symphony open electrode 1024 x 256 CCD detector. Section 3.2.3 further discusses the operation of the detector.

Alignment procedure:

Each time the cryostat was reinstalled in the setup, after evacuation and/or changing the sample, the focusing and collection lenses were aligned along their axial directions as shown in Fig. 3.2 and mentioned above. These lenses were aligned by observing the maximum detected signal from the sample. The general alignment procedure before collection of datasets is outlined as follows.

1. The focusing lens' height, lateral position, and then axial position were adjusted to achieve a maximum signal. For studies at low PIs when a focusing lens was not used, the knobs on a kinematic mirror mount directing the beam to the cryostat were each slightly adjusted.
2. The axial position of the PL collection lens was then aligned to achieve a maximum signal.
3. Steps 1 and 2 were repeated to optimize alignment of the pump and PL collection spots.
4. The F/#-matching lens was slightly adjusted to optimize the focus of the collected luminescence onto the entrance slit.

3.2.2. Experimental arrangements

The arrangement of the PL spectroscopy setup in Fig. 3.2 was slightly adjusted to collect data under two different conditions: (1) high PIs and (2) low PIs. The two setups are described below.

(1) High pump intensities

To achieve high PIs, the PL setup shown in Fig. 3.2 was used with a focusing lens. From this arrangement, two types of data sets were attained: PL as a function of exposure of the sample to the pump and PL as a function of PI. In the former, a spectrum was repeatedly acquired after a specified time interval while the sample was continuously pumped at a constant PI. In the PI dependent measurements, on the other hand, a spectrum was acquired at various PIs.

(2) Low pump intensities

To achieve low PIs, the focusing lens in Fig. 3.2 was removed so that a broader area on the sample was excited. This allowed for collection of temperature-dependent PL datasets at particular PIs, as the pump spot was so broad that thermal expansion of the sample holder with temperature change, which moves a new region of the sample into the excitation beam, was negligible.

3.2.3. The spectrometer

This section describes the configuration and operation of the spectrometer. Two types of spectrometers, monochromators and spectrographs, are first distinguished. The configuration of the Czerny-Turner spectrograph used for this work is then introduced. This leads into a discussion on each of the components in the instrument: an entrance slit, a collimating mirror, a diffraction grating, a focusing mirror, an exit plane, and an optical detector. Finally, a description of the various settings that were adjusted to tune the detection of the PL is given.

Monochromators and spectrographs:

An optical spectrometer creates an image of the input on its entrance slit in the form of a spectrum at its exit. There are two types of spectrometers: monochromators, which pass one frequency at a time through its exit slit, or spectrographs, which pass a band of frequencies to an exit plane. The Horiba Jobin Yvon iHR320 spectrometer is the latter type with the option of sending the signal to one of two multichannel photodetectors: a charge coupled device (CCD) or InGaAs array.

Czerny-Turner spectrograph:

There are many possible designs of the internal optics in a spectrometer. Ours has the most

common Czerny-Turner configuration, shown Fig. 3.2. A larger view of the spectrometer optics is shown in Fig. 3.7.

The Czerny-Turner configuration has five main components: the entrance slit, a collimating mirror, a diffraction grating, a focusing mirror, and an exit plane (or an exit slit for a monochromator) [34]. Light focused at the entrance slit is sent to a collimating mirror. The collimating mirror passes the light to a diffraction grating at an angle of incidence α. The dispersed light, at an angle of diffraction β, is sent to a focusing mirror. This focuses the diffracted light onto an exit plane and is detected by a multichannel detector.

As much light as possible is coupled from the sample into the entrance slit of the spectrometer. The coupling optics are chosen so that the half angle of the cone of light entering the spectrometer matches the numerical aperture or f-number (f/#) from the entrance to the next internal component, which is a collimating mirror.

The collimating mirror collimates and directs the light to a diffraction grating. One of three gratings mounted on a turret can be selected to disperse the signal. If the f/# of the light entering the spectrometer has been correctly chosen, the light will just underfill the grating area to average over as many rulings as possible while not losing any signal.

The f/# of an optical component is the ratio of its focal length f to the diameter D of light incident on the component [33,34]:

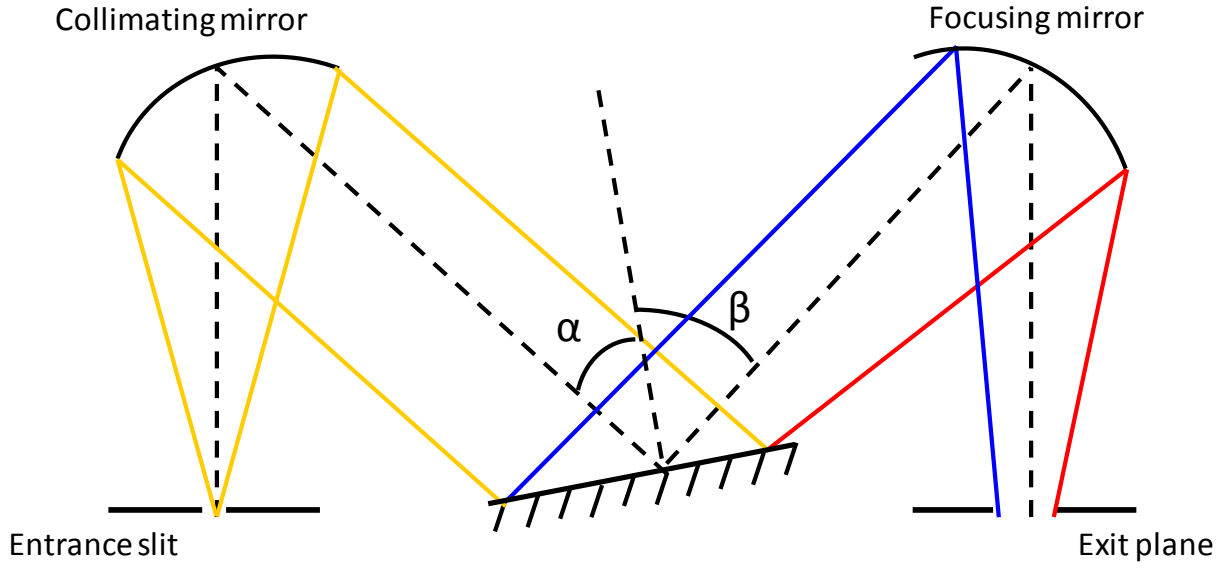

Fig. 3.7: Czerny-Turner spectrometer configuration. Figure adapted from Horiba Jobin Yvon [34].

$$f/_{\#} = \frac{f}{D}. \tag{28}$$

Equation (28) shows that the PL light must not be focused onto the entrance slit with an f/# smaller than that of the spectrometer's internal entrance optics, which is f/# = 4.1 for this system. The light would otherwise overfill the gratings, leading to stray light and signal degradation.

The throughput of light can also be reduced if the entrance slit size is smaller than the spot size of the light focused on the slit. In this case, the slit acts as an aperture stop and limits the amount of light entering the spectrometer.

Once the light is passed to the grating, the geometry of the grating determines how the light is dispersed. A diffraction grating consists of equally spaced grooves along its surface. The groove width is on the order of the wavelength of light, so that when encountered with light, each groove acts as a point source. At any angle from the normal, the resulting diffracted light is a superposition or interference of all waves at that point.

Constructive interference can only occur for waves of the same frequency and phase. Waves of the same frequency from neighbouring grooves add constructively if their path difference at a point in the far field is an integer multiple of the wavelength of light. This results in intensity maxima occurring at different directions or angles of diffraction β for each wavelength, giving a spectrum. For an angle of incidence α, the grating equation is given by [33,34]:

$$\sin(\alpha) + sin(\beta) = kn\lambda \tag{29}$$

where n is the groove density, λ is the wavelength, and k is an integer value known as the order of diffraction. Note that the diffracted light intensity is distributed among the different orders, or occurrences of constructive interference.

The gratings chosen for this spectrometer are planar and work in reflection mode. The spectrometer images their first order diffracted light. The gratings are also all blazed in first order, meaning that the groove profile is designed to concentrate the intensity of diffracted light into a particular non-zero order.

All measurements discussed in Chapter 4 were taken with the third grating designated Grating III on the turret. Fig. 3.8 shows the relative efficiency curve for this grating, model 530 24 from Horiba Jobin Yvon. This is a theoretically generated curve for first order diffracted light from the grating. It shows the efficiency profile for both TE (transverse electric) and TM (transverse magnetic) polarized light. This grating is a holographic plane grating blazed at 500 nm and has a groove density of 1200 grooves/mm. The grating groove density is related to its spectral range, which is the size of the window of wavelengths that can be scanned from an order at a time. Grating III has a spectral range of 60 nm.

Multichannel detectors:

The diffracted light is passed from the grating to a mirror that focuses the spectrum onto an exit plane. The grating's position can be changed to select the angles of diffracted light sent to the detector. A multichannel detector allows simultaneous detection of various wavelengths, while in monochromators a single channel detector is placed at the exit slit to detect one wavelength at a time. In this spectrometer, one can choose either a CCD or InGaAs array detector. To detect PL from the nanocrystals the CCD imaging detector was used. The CCD can detect wavelengths in the range of ~200-1000 nm, while the InGaAs

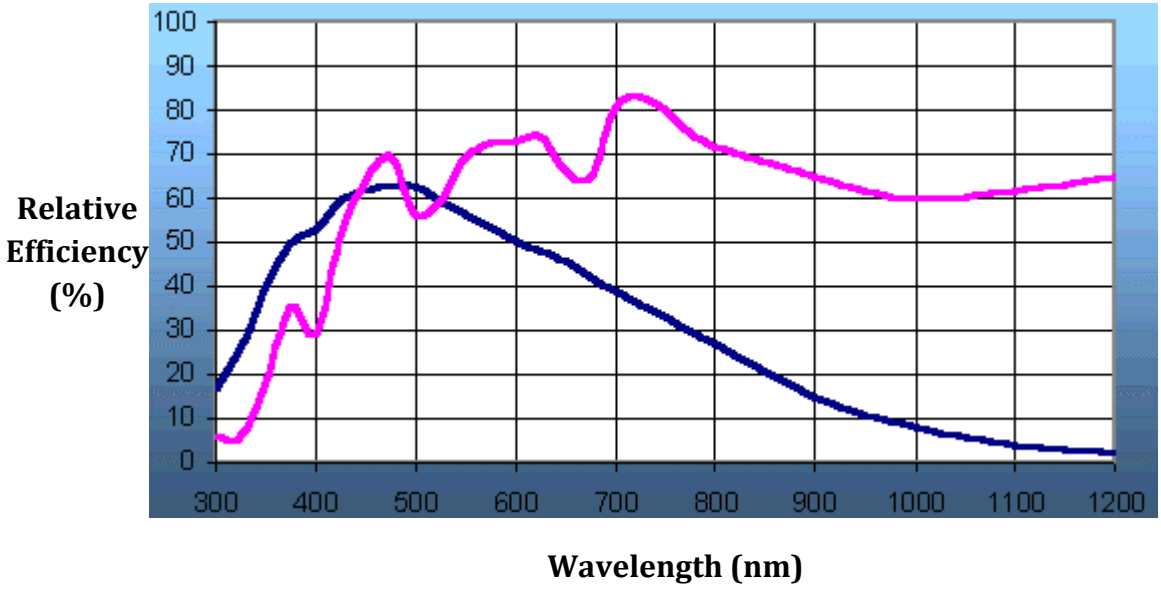

Fig. 3.8: Grating III (model 530 24) relative efficiency curves for TE (navy) and TM (magenta) polarized light. Figure adapted from Horiba Jobin Yvon [34].

array can detect wavelengths in the range of ~1000-1600 nm.

The CCD detector has a two dimensional array of pixels, or capacitors. Under illumination, photoelectrons are created and are trapped within a potential well created by an applied voltage. An image, or spectrum, is created by transferring charge from pixel to pixel. Each column of pixels corresponds to one wavelength, so the sum of electrons in that column is proportional to the number of incident photons at a particular wavelength. This gives a spectrum of the intensity of light in units of counts of electrons (or photons).

Electrons created by thermal energy are a source of noise in these detectors. For this reason, both of the detectors are cryogenically cooled so that they can measure low light levels. The CCD detector is cooled to 140 K and the InGaAs array is cooled to 170 K. Fig. 3.9 shows the quantum efficiency curves for the CCD detector used to study the nanocrystals. The literature [34] states that the detector has a quantum efficiency of about 40 % at 25 °C.

Spectrometer settings for data collection:

It was previously mentioned that all measurements were taken with Grating III and the CCD detector. This section describes the other various spectrometer settings that were adjusted for data collection: entrance slit width, CCD exposure time, CCD dark current subtraction, grating orientation, and averaging spectra. The spectrometer data acquisition, incidentally, was integrated with Origin software, which was consequently used to analyse and graph all

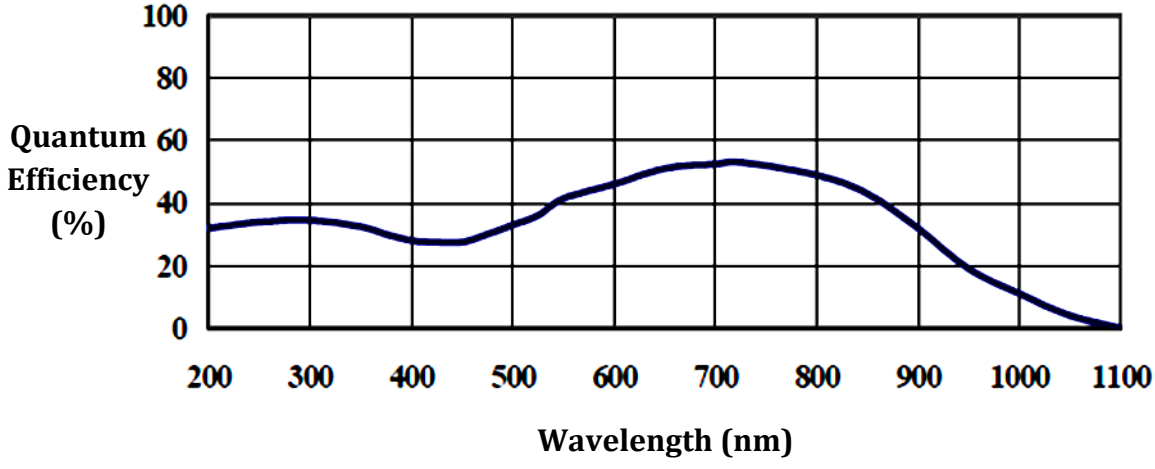

Fig. 3.9: Symphony open electrode 1024x256 CCD detector quantum efficiency curve. Figure adapted from Horiba Jobin Yvon [34].

the data shown in Chapter 4.

1. The entrance slit width is computer controlled and can be set between 0 - 2 mm in steps of 2 μm. For the high PI measurements a slit width of 0.05 mm was used to give the best resolution (see Appendix D), while the low PI measurements yielding weaker PL signals, used a slit width of 0.5 mm to collect more light.

2. The CCD exposure time is the amount of time that the CCD array is illuminated while capturing the spectrum and is controlled by a shutter. This setting was adjusted according to the signal strength; low signals are dominated by noise while signals that are too high saturate the detector. The exposure time can be set to as short as 0.001 seconds and for as long as 49.71 days. Exposure times below 0.1 seconds were not used as there is a larger uncertainty in achieving these times with the shutter.

3. The CCD detector has a feature that can subtract the detector's dark current arising from thermal noise from the spectrum. When this setting is selected, the spectrometer takes a scan of the dark current with the CCD shutter closed and subtracts this signal from a subsequent spectrum taken with the shutter open under the same conditions.

4. Before collecting each spectrum, the desired window of wavelengths to scan was specified. This was done by choosing two different types of orientations of the grating: "position" or "range". The position option places the grating at a central wavelength. The window size of the captured spectrum depends on the spectral range of the grating, which was mentioned to be about 60 nm for Grating III. The range setting, on the other hand, allows one to enter an interval of wavelengths to scan. If this interval is larger than the grating's spectral range, the grating is rotated to capture portions of the spectrum at a time. These portions, or acquisitions, are each collected at the specified CCD exposure time and are "stitched" together to

create the spectrum. To capture the full PL spectrum from the cQDs, the spectrometer stitches together three acquisitions.

5. The spectrometer software can average spectra over a specified number of accumulations. This is useful for reducing noise in low signal levels.

Chapter 4 Results

PL measurements pertaining to transitions between the ground and first excited states of $CdSe/Cd_{0.5}Zn_{0.5}S$ cQD ensembles are presented and analysed in this chapter. Results show insight into bleaching processes, the quantum efficiency behaviour, the temperature dependence of the PL peak position, and phonon assisted spectral broadening.

Results are reported for four samples, where preparation methods were described in Chapter 3. The experimental setup used was also described in Chapter 3. Three distinct regimes were investigated: PL dependence on strong PI, PL dependence on weak PI, and PL dependence on temperature at weak PI.

Initial PL measurements were undertaken with high PI to determine the onset of significant bleaching, that is, of nonlinear PL dependence on PI. These were first done by monitoring the temporal change in the PL due to fixed high PI on different samples. Later measurements examined this behaviour on one sample for low PIs. Bleaching behaviour was observed for samples excited by high PIs, while fairly stable signals were observed when testing at the lowest. Subsequently, the nonlinear PL was measured over an extended range of high PI to investigate the bleaching process.

Measurements of PL were undertaken with low PI for several different pump intensities in order to generate datasets in the linear regime. For each PI, data were collected over an extended temperature range. Since the QD response (quantum efficiency, peak shift, and phonon processes) should be independent of PI in the linear region, the results at different PIs were averaged for enhanced accuracy.

Various pump powers were selected via neutral density filters to carry out the PI-dependent PL measurements. The sample was only exposed to the laser while acquiring spectra by opening the electric shutter and each spectrum was collected with minimum possible detection times to prevent any residual bleaching.

Adjustment of the sample's temperature was achieved using the cryostat and temperature controller as described in Chapter 3. As for the PI-dependent measurements, the laser shutter was only opened while collecting spectra and detection times were set to a minimum.

An overview of a few typical features observed in the spectra, that are characteristic of either the sample's properties or experimental artefacts, is given in the next section. This

section ends with a brief discussion on uncertainties in the data. The remainder of the chapter discusses the PL results, the first set of which were taken with high optical pumping to study bleaching phenomena. The next datasets were taken at low pump intensities to avoid significant bleaching for study of temperature-dependent behaviour. Three different types of results are studied from these latter measurements: the quantum efficiency scaled by the absorption cross section, the material's peak energy position variation with temperature, and thermal broadening arising from carrier-phonon coupling.

4.1. Spectral shape

A typical PL spectrum from an ensemble of cQDs is shown in Fig. 4.1. Three qualities can be immediately identified in this plot: the broad linewidth, the asymmetric shape, and two small abrupt shifts in PL intensity. The two former aspects relate to PL properties of the

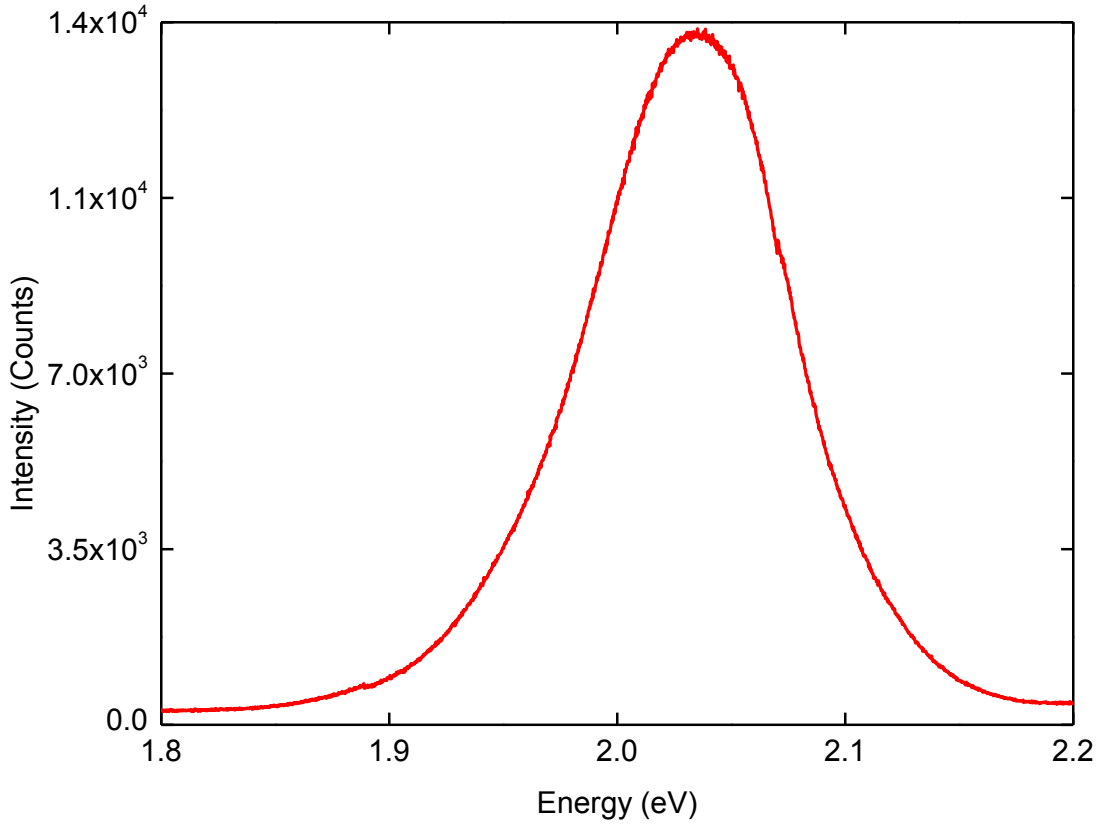

Fig. 4.1: PL spectrum of Sample 4. The sample was cooled to 80 K and pumped at 9,981 mW/cm^2.

cQDs, while the latter is an experimental artefact due to stitching.

The PL from QDs having a particular size is ideally a single frequency energy, however, its line width is homogeneously broadened due to different factors, including phonon scattering. Inhomogeneous broadening in a QD ensemble results from the distribution in QD sizes, as fabrication produces an inevitable variation in the QD size. The collective PL is thus a superposition of individual dot spectra, taking form of a Gaussian with a random distribution centred about a mean PL intensity.

The asymmetry suggests that the spectrum is in fact a superposition of more than one Gaussian peak. According to refs. [29,35], this may be attributed to Förster resonance energy transfer (FRET) between dots of different sizes. Also, in a sample of closely spaced QDs, it is possible that fluorescence energy from the smaller dots can excite larger ones. This agrees with the observation of more PL at the tail of lower energies.

Two stitching errors are observed in this spectrum: a decrease in PL counts at 1.889 eV by 10.8 %, and an increase in PL at 2.070 eV by 2.14 %. To collect the full spectrum, three acquisitions of Grating III were stitched together at the positions of the abrupt shifts in PL. These jumps occur due to a slight misalignment of the CCD array. This detector was aligned as best as possible so that its pixel array was square with the diffracted light from the grating. A slight misalignment results in improper illumination of pixels at the wavelength boundaries captured by the detector.

One last point to address concerning this plot is that error bars are not shown, because they are much smaller than the curve's line thickness. Uncertainties in the detected PL counts follow counting statistics, so the uncertainty is the square root of the detected counts value. This chapter also shows PL data plotted as a function of other variables: as a function of PI, time, and temperature. Error bars in these variables are not shown for the reason that they are on the order of the symbol size.

4.2. High pump intensities

PL measurements collected at high PIs using the focused pump beam in experimental arrangement (1) mentioned in Chapter 3 showed bleaching behaviour. Section 4.2.1 reports preliminary PI dependent measurements of Samples 1 and 2 which portray unmistakable

saturation curves. Section 4.2.2 shows later, more quantifiable, investigations of Samples 3 and 4 in which both sample exposure dependent and PI dependent measurements show bleaching.

4.2.1 Saturation curves

Preliminary measurements over an extended range of PIs have shown saturation, as those shown in Fig. 4.2 for Samples 1 (red circles) and 2 (blue right triangles). The PL spectra were collected with increasing PI. The peak intensity of each spectrum is plotted as a function of PI. The peak intensities are normalized to the maximum values in the respective datasets. The PI values are in arbitrary units, because the pump beam spot size on the sample was not measured before collecting these datasets.

These measurements clearly show the two anticipated linear and saturation regimes for PI dependent measurements described in Chapter 2. The cQDs' quantum efficiency and

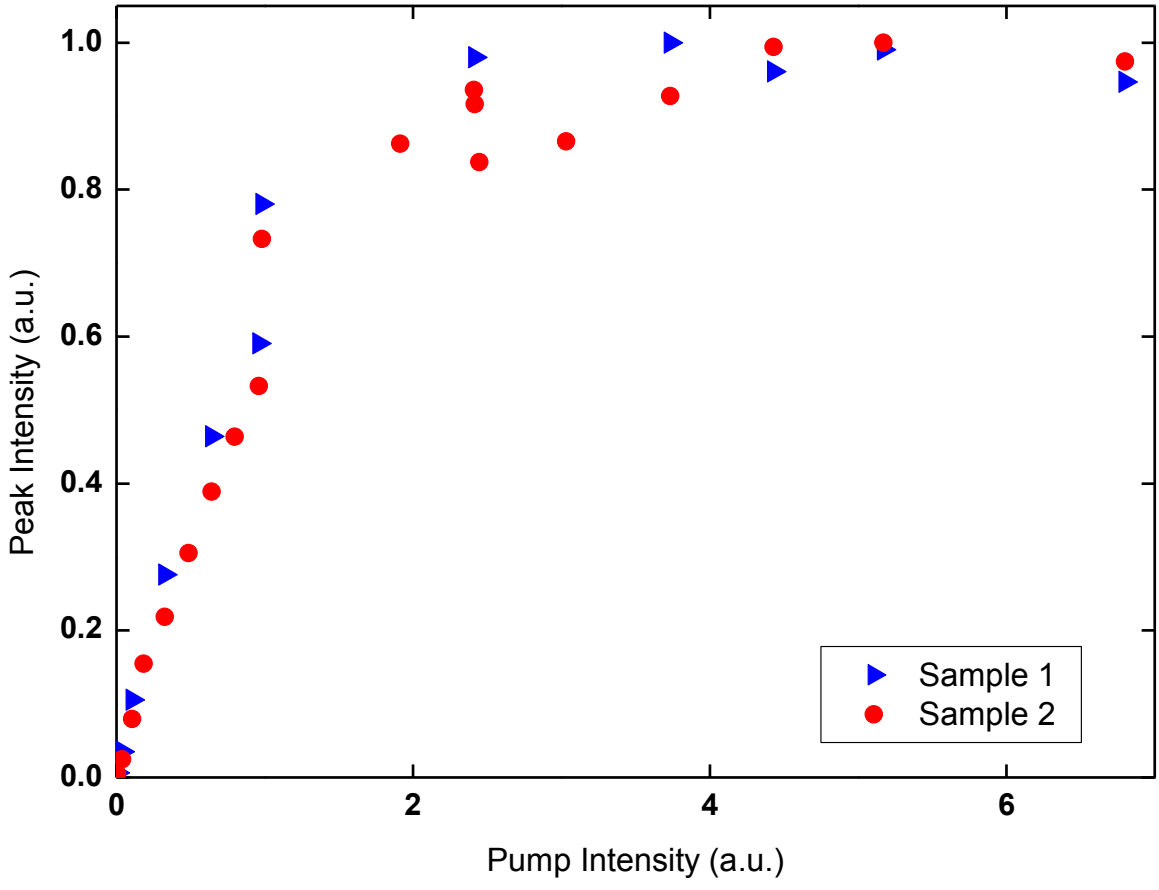

Fig. 4.2: Saturation curves for Samples 1 (red circles) and 2 (blue right triangles).

consequent lifetimes values could not, however, be extracted due to the inability to estimate the number of QDs pumped. As mentioned in Chapter 3, these two samples were prepared amongst early trials during which drastically non-uniform QD distributions resulted after casting unknown amounts of QDs onto the slide. Adding this to the uncertain spot size, the number of cQDs pumped in these measurements is completely unknown.

Later measurements, shown in the following section, showed that the QDs exhibit bleaching at high PIs. This knowledge that the cQDs exhibit bleaching adds another uncertainty to the data in Fig. 4.2, in that the fraction of cQDs pumped that had bleached from pumping on previous occasions is unknown. The same spots on the samples had been previously exposed to the laser on a number of occasions. The samples had likely been heavily bleached before collecting the data in Fig. 4.2.

4.2.2 Bleaching analysis

After taking preliminary measurements at high PIs on Samples 1 and 2 shown in the previous section, Samples 3 and 4 were prepared having an estimable number of dots on the substrate with more uniform distributions, especially for Sample 3. This section shows the bleaching behaviour observed in these samples at high PIs.

PL was monitored from the cQDs at room temperature in three different external environments under continuous exposure to the highest PI of 6,802 W/cm^2. This data is shown in the curves of black squares in Fig. 4.3 for (a) Sample 3 in air, (b) Sample 4 in air, and (c) Sample 4 in vacuum. Plot (a) shows the peak PL intensity as a function of exposure time, while plots (b) and (c) show integrated PL as a function of exposure time. Note that on previous occasions, the integrated PL showed a linear relationship with the PL peak intensity, and thus the plots in Fig. 4.3 can be compared without ambiguity. Before taking the measurement in Plot (a), the sample spot had been previously exposed to the laser. In the other two plots, the test was done on unexposed regions of the sample.

The data in all three cases was collected with the CCD exposure time set to 0.1 seconds. This exposure time was set to minimize bleaching within a scan. Keep in mind that three or four acquisitions composed each scan, so the time that the sample was exposed to the laser for each spectrum was longer than 0.1 seconds.

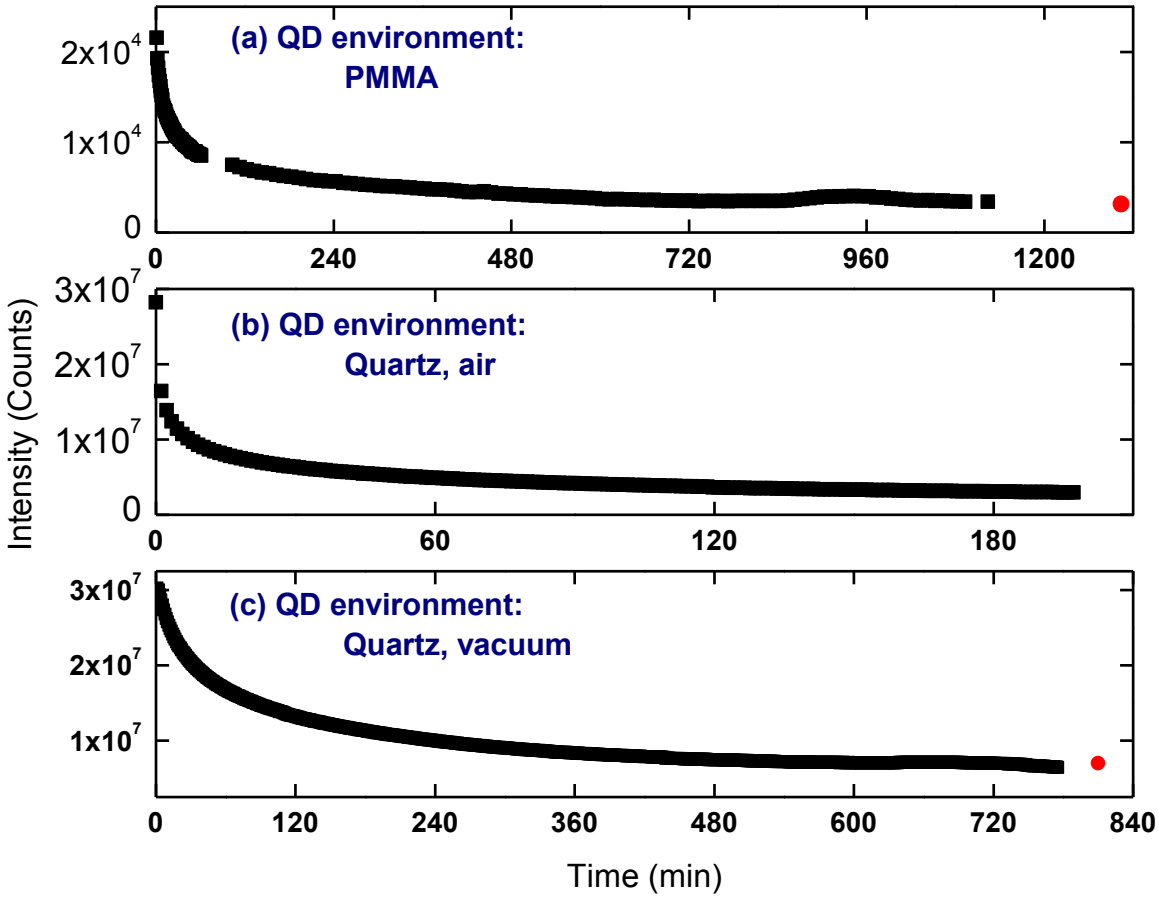

Fig. 4.3: PL as a function of sample exposure to continuous PI of 6,802 W/cm^2 (curves shown by black squares). PL bleaching is shown in three different sample environments: (a) Sample 3 in air, (b) Sample 4 in air, (c) Sample 4 in vacuum. The red circles in (a) and (c) show that the PL intensity does not recover after the sample had not been exposed to the laser for 3 hours and 35 minutes, respectively.

In Fig. 4.3 (a), the PL peak intensities were determined with Origin's "Peak Finder" tool which gave the value of the highest data point in each spectrum. As the spectra were not very noisy and the signal was large enough that cosmic rays were not apparent, this method gives reliable PL peak values.

In Fig. 4.3 (b) and (c), the integrated PL was determined by summing the data points under the spectra with Origin's "Column Statistics" tool. The spectra did not have any noticeable cosmic rays, so the uncertainty in these peak data points is minimal.

All three samples show bleaching in PL. Samples 3 in air and 4 in vacuum were tested for PL recovery after not pumping for about 3 hours and 35 minutes, respectively. The red data points in plots (a) and (c) show no recovery. Recovery has not been observed in these samples on any of the timescales investigated.

A LEICA GZ6T microscope was used to view Sample 3 after the measurement in Fig. 4.3 (a) as a rough check for signs of damage to the sample after pumping at a high PI. Fig. 4.4 is a photo taken with an eyepiece camera of the sample mounted on the cryostat. Within the resolution of the microscope, there are not any dark spots observed to indicate damage to the sample.

Additional bleaching behaviour is observed in PI-dependent PL at high PIs. Fig. 4.5 shows hysteresis in the plots of the peak intensity count rate as a function of PI for (a) Sample 3 at 78.5 K in vacuum and (b) Sample 4 at room temperature in air. In both cases, the samples had not been previously exposed to the laser. Measurements were first collected with increasing PI from 5.74 to 6,800 W/cm^2 (black squares) and then decreasing back to 5.74 W/cm^2 (red circles).

The samples were only pumped during collection of the spectra in Fig. 4.5. A beam block was used to block the laser between the Sample 3 measurements and the laser electric shutter was closed between the Sample 4 ones. The acquisitions of each scan in the Sample 3 spectra were taken with CCD exposure times between 0.1 to 0.5 seconds, while the Sample 4 ones were taken with 0.1 or 0.2 second exposure times.

The peak intensity values were determined differently in each dataset: the Sample 3 spectra were smoothed, while the Sample 4 ones were fitted to Gaussian functions. The

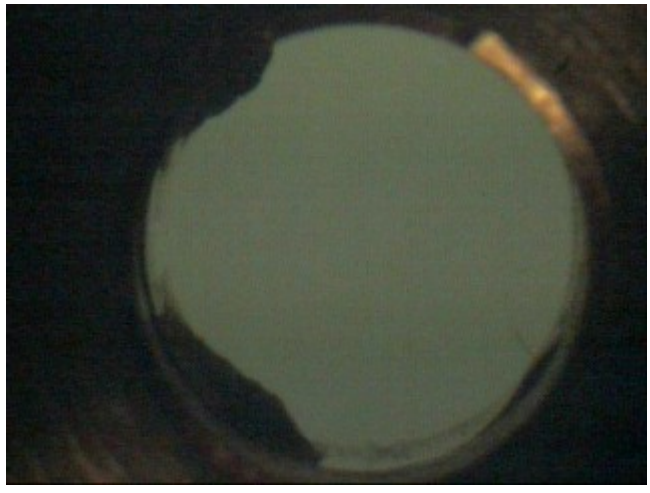

Fig. 4.4: Microscope photo of Sample 3, mounted in cryostat, after bleaching test in Fig. 4.3 (a). After high PI pumping for several hours, dark areas cannot be observed, within the resolution of the microscope, to suggest sample damage. Note that the green colour is due to light scattering and is not significant to the sample's optical properties.

smoothing was done with a fast Fourier transform (FFT) filter that sampled a window of 50 points, while the spectra typically had about 4,000 – 5,000 points. The peak height was then manually selected with Origin's data reader tool. It was noted that this smoothing sometimes lowered the height of the peak; however, these shifts were not observed to be larger than 1 or 2 %.

The Gaussian fits were done to approximately the top 10 % of the spectrum. The fits gave a value for the centre wavelength position along with a set of data points generating a Gaussian curve. The peak value corresponding to the centre wavelength position was used as the peak height.

Both Samples show similar behaviour in Fig. 4.5. Preliminary measurements, taken with multiple cycles of increasing and decreasing PI, have shown decreasing PL for

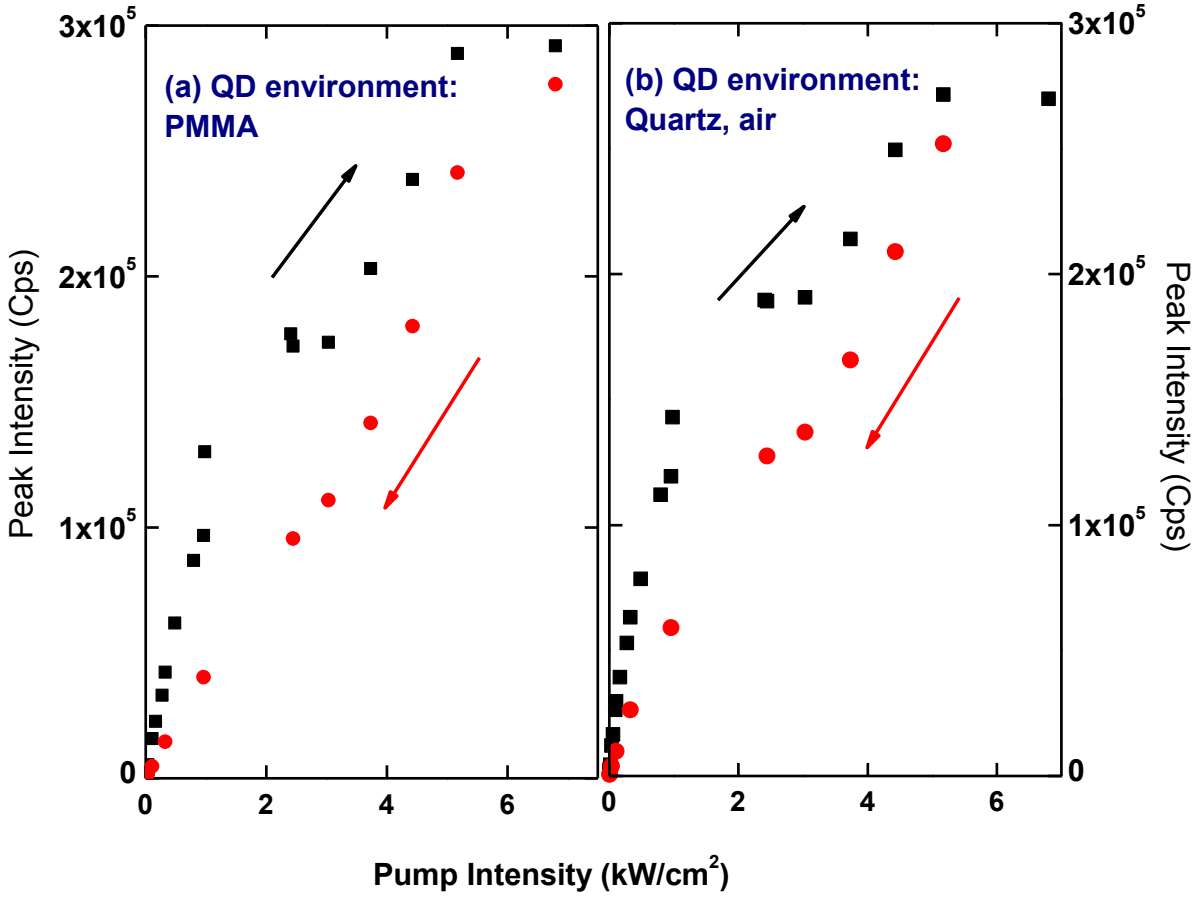

Fig. 4.5: PL peak versus PI for the QD samples in two different external environments: (a) Sample 3 at 78.5 K in vacuum and (b) Sample 4 at room temperature in air. Black squares are increasing pump power measurements while red circles are decreasing.

successive cycles. The hysteresis in the PL dependence on PI demonstrates non-reversible bleaching. The increasing PI data in Fig. 4.5 show three different regimes. Below ~2 kW/cm^2 is a quasi-linear regime where moderate bleaching takes place, as bleaching is seen at ~ 0.01 kW/cm^2 in the following section of bleaching tests in Fig. 4.6. Further increase in pumping to ~5 kW/cm^2 shows nonlinear behaviour. This nonlinear behaviour is indicative of bleaching. As more cQDs are bleached, the population of non-bleached dots changes. Furthermore, as different cQDs bleach differently, the PL behaviour is non-reversible when the measurement is repeated, which is demonstrated by the decreasing PI data. The minor plateau between 2 and 4 kW/cm^2 suggests that a damage threshold has been reached, and is hypothesized to be a result of strain relaxation at the core/shell interface, as this behaviour disappears upon decreasing PI. The third regime shows a second plateau above 5 kW/cm^2. This may be due to saturation of the first excited state, however, it is possible that another damage threshold has been reached. The same trend of bleaching behaviour exhibited by the cQDs in two different external environments indicates that the cQD shell sufficiently passivates the core and that non-radiative mechanisms must take place within the core and/or shell structures.

4.3. Low pump intensities

To avoid bleaching behaviour, the temperature dependent PL of Sample 4 was studied at low pump powers using the unexpanded beam in experimental arrangement (2) discussed in Chapter 3. Data was acquired at pump powers of approximately four different orders of magnitude: 8.46, 155, 1,410, and 10,000 mW/cm^2. Note that the highest PI, 10,000 mW/cm^2, is almost a factor of 2 larger than the lowest PI of 5.74 W/cm^2 studied in the previous section at high PIs. Thus, it was anticipated that this highest PI would show bleaching.

Section 4.3.1 shows sample exposure time dependent PL measurements at room temperature which only demonstrate significant bleaching at the highest PI. The next sections discuss results of temperature dependent PL datasets at each PI. Section 4.3.2 introduces the temperature dependent data. The sample's quantum efficiency behaviour is explored in Section 4.3.3. Section 4.3.4 studies the temperature dependence of the PL peak

position and the last section, Section 4.3.5, shows thermal broadening resulting from phonon scattering in the PL spectra.

4.3.1 Bleaching tests

Fig. 4.6 shows integrated PL as a function of time for continuous pumping of the sample in vacuum at (a) 8.46 mW/ cm^2 (black squares), (b) 155mW/ cm^2 (red circles), (c) 1,410 mW/ cm^2 (green up triangles), and (d) 10,000 mW/ cm^2 (blue down triangles). For (a), the sample temperature was the ambient room temperature, which was ~ 296 - 297 K. For (b), (c), and (d), the sample temperature was set by the cryostat heater at 305 K. For easy comparison of the features in all four curves, the data in (a) and (b) are scaled by factors of 200 and the data in (c) is scaled by a factor of three.

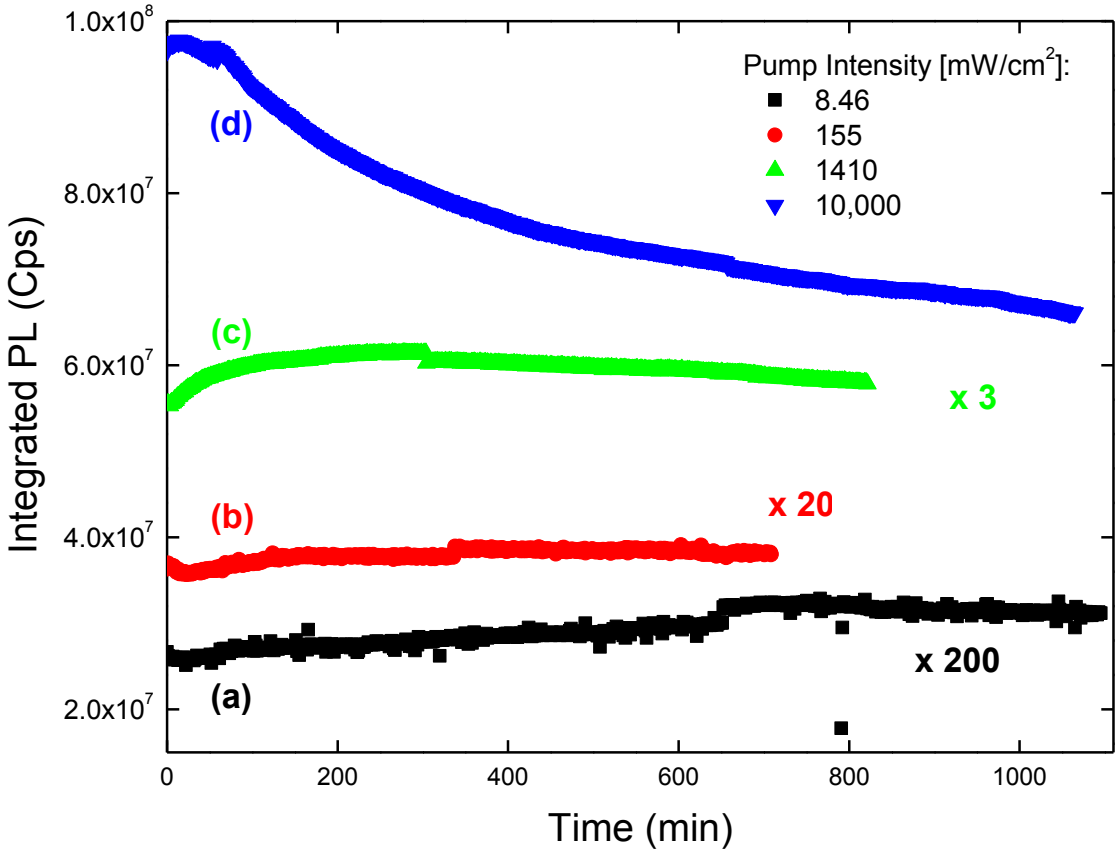

Fig. 4.6: PL stability tests for Sample 4 at low PIs: (a) 8.46 mW/ cm^2 (black squares), (b) 155 mW/ cm^2 (red circles), (c) 1,410 mW/ cm^2 (green up triangles), and (d) 10,000 mW/ cm^2 (blue down triangles). All measurements were done in vacuum at room temperature in (a) and at 305 K in (b), (c), and (d). To easily compare the features of each curve, the three lower PI datasets are scaled by the corresponding factors indicated on the plot.

Different CCD exposure times were used to collect the acquisitions in each dataset: 2 seconds for (a), 0.2 seconds for (b) and 0.1 seconds for each (c) and (d). These exposure times were chosen to collect the spectra within a small time interval while still achieving a reasonable signal to noise level.

The integrated PL values were determined by summing all of the intensity data points in one spectrum. This sum was then normalized with respect to the CCD exposuretime to get the total count rate. The data are noisy due to failure to remove many cosmic rays which become more apparent at longer CCD exposure times and lower signal levels. The time periods over which the PL was monitored were: ~18.2 hours in (a), ~11.8 hours in (b), ~13.7 hours in (c), and ~17.7 hours in (d). The PL at the three lower PIs is fairly stable, while the highest PI shows definite evidence of bleaching.

Although the PL is fairly stable with low PI pumping, the plots do show a few anomalies that are distinct from the noise. Plots (a) and (b) each slow a slight drop in PL at the very beginning before a gradual increase. Sudden increases in PL by small fractions are also observed by ~6 % after about 10.9 hours in (a) and by ~ 2.5 % after about 5.6 hours in (b). In (c), however, the PL suddenly decreased by ~ 1.9 % after about 5.1 hours of pumping.

It is unlikely that the abrupt increases and decreases are caused by enhancement and bleaching processes in an ensemble of QDs. These shifts may be explained by sudden changes in optical pumping: a drift in laser power may have resulted from a change in line voltage, which has been noted to occur during overnight hours in the laboratory's building. The laser power has been measured with a Newport 918D-SL-OD3 silicon photodetector and a Newport 842-PE power meter to be stable over 40 minutes within the resolution of the readings on the meter. A power measurement has not been done, however, over a longer time period. Alternatively, a shift in the alignment of the setup may have been caused by vibrations in the room.

Some other more gradual changes are observed in the three low PI curves. Curve (c) shows a gradual increase in PL by ~10.8 % from initial exposure to the point of sudden decrease after about 5.1 hours. It is possible that this is caused by PL activation or enhancement. From this point after the jump at ~5.1 hours, the PL gradually decreases by ~4 % to the end of the measurement at ~13.7 hours which may be explained by bleaching.

The highest PI measurements in curve (d) shows definite evidence of bleaching. For about the first hour the PL is fairly constant. Over the entire time of data collection of ~17.7 hours, the PL decreases by ~32 %.

4.3.2 Photoluminescence temperature dependence

Temperature dependent PL data was collected between 80-360 K at the four low PIs for Sample 4: With the exception of the highest PI data, the PL was shown to be fairly stable over many hours in the previous section and is thus used to study the quantum efficiency behaviour and the temperature dependence of the cQDs in the next sections. All of the low PI data, both the stability tests and temperature dependent PL, were collected from the same spot on the sample with increasing PI. The stability tests, followed by the temperature dependent measurements, were first collected using the lowest PI and then the second lowest PI. Due to time constraints, the temperature dependent spectra were acquired before performing the stability tests.

Although the sample spot was not deliberately changed between all measurements, it was calculated that the sample spot had shifted during collection of temperature dependent data due to thermal expansion of the cryostat's thermal link and copper sample mount. This calculation is discussed below.

Thermal shift of sample position:

As mentioned in Chapter 3, the sample is mounted in the cryostat on a copper holder which is attached to the LN2 reservoir with a steel thermal link. As the temperature of the sample mount and thermal link increase, they thermally expand. The expansion in the vertical direction brings different regions of the sample into the pump spot. As the sample did not have a uniform dot density, different dot densities are pumped at different temperatures. To study the temperature dependence, all of the PL data must be collected from a particular dot density region.

The one-dimensional thermal expansion equation, below, was used to calculate the change ΔL in the vertical length L of the copper and steel materials over a temperature change ΔT:

$$\Delta L = L\, \alpha\, \Delta T, \tag{30}$$

In this equation, the parameter α is the linear thermal expansion coefficient characteristic of the material. Copper has a value of 17 x 10^{-6} / C°, while steel has a value of 11 x 10^{-6} / C° [36]. The copper mount was estimated to have a vertical dimension of 2.50 in., while the steel thermal link's height was estimated to be 1.50 in. It was found that the sample shifts by ~420 μm, over a 80-360 °C temperature range and by ~300 μm over 80-280 °C. This shifts the spot that was pumped by the focused beam by ~ 4.5 times and 3.2 times over the respective temperature ranges, but only shifts the unfocused spot by ~ 19 % and 13 %, respectively.

The PL data observed above 280 °C with the unfocused beam was inconsistent with that below this temperature. Above room temperature, there was not any LN2 in the cryostat and the sample had most likely shifted by about the calculated ~19 % value. At the different temperatures below room temperature, there was LN2 in the cryostat and the sample was unlikely to shift much from one measurement to another.

Temperature dependent spectra:

The temperature dependent PL data between 80-280 K are shown, from lowest to highest PI, in Fig. 4.7-Fig. 4.10, respectively. During the temperature dependent measurements, the laser shutter was only opened while collecting spectra. Each spectrum was averaged over a number of accumulations due to the low signal levels. Each accumulation stitched together scans from three grating acquisitions to capture the frequency range of the PL spectra. The conditions under which the temperature dependent PL spectra were collected in Fig. 4.7 - Fig. 4.10 are summarized in Table 4. The approximate time per scan, which is also the same time period that the sample was exposed to the laser, was measured with a clock.

Note the presence of cosmic rays as intense narrow peaks in some of the spectra in Fig. 4.7 - Fig. 4.10. They are especially more apparent in the measurements with lower signal levels and taken over longer CCD exposure times. Negative peaks in the spectra are a result of cosmic rays that occurred in the CCD dark current signal that was subtracted from the spectrum. Many of the very large cosmic rays were removed from these plots for the analysis.

The lowest PI data was first taken with increasing temperature from 300-360 K, then decreasing from 330-80 K. The spectra between 80-280 K, representative of the same

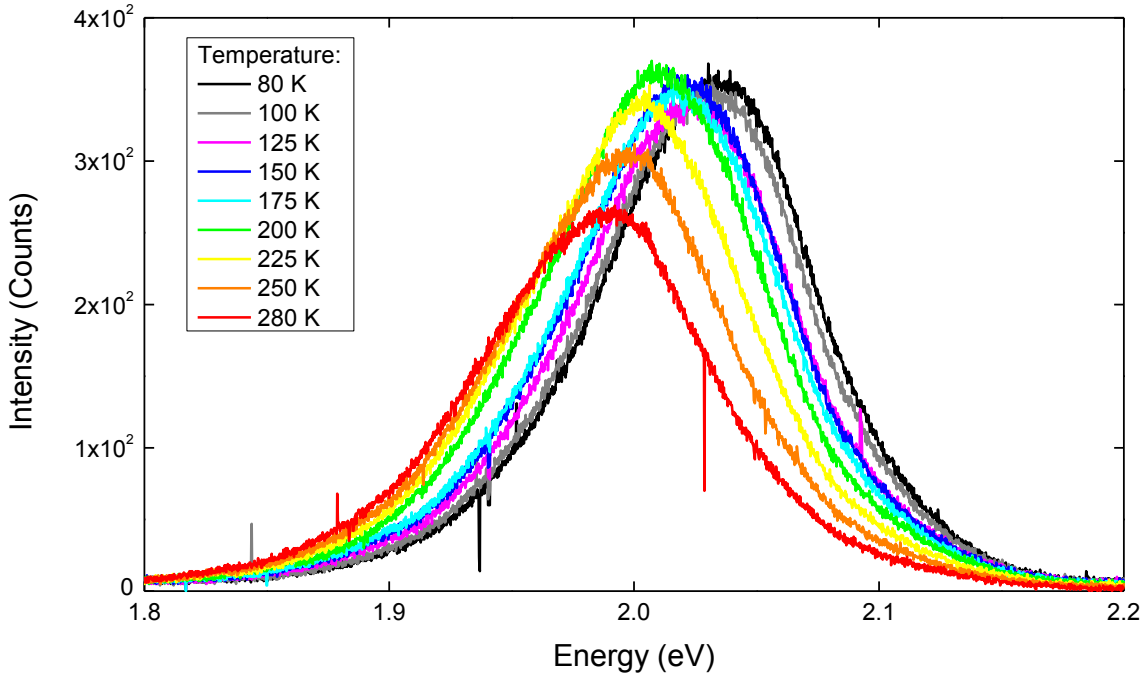

Fig. 4.7: PL spectra of Sample 4 acquired at 8.46 mW/cm^2 pumping and sample temperatures between 80-280 K.

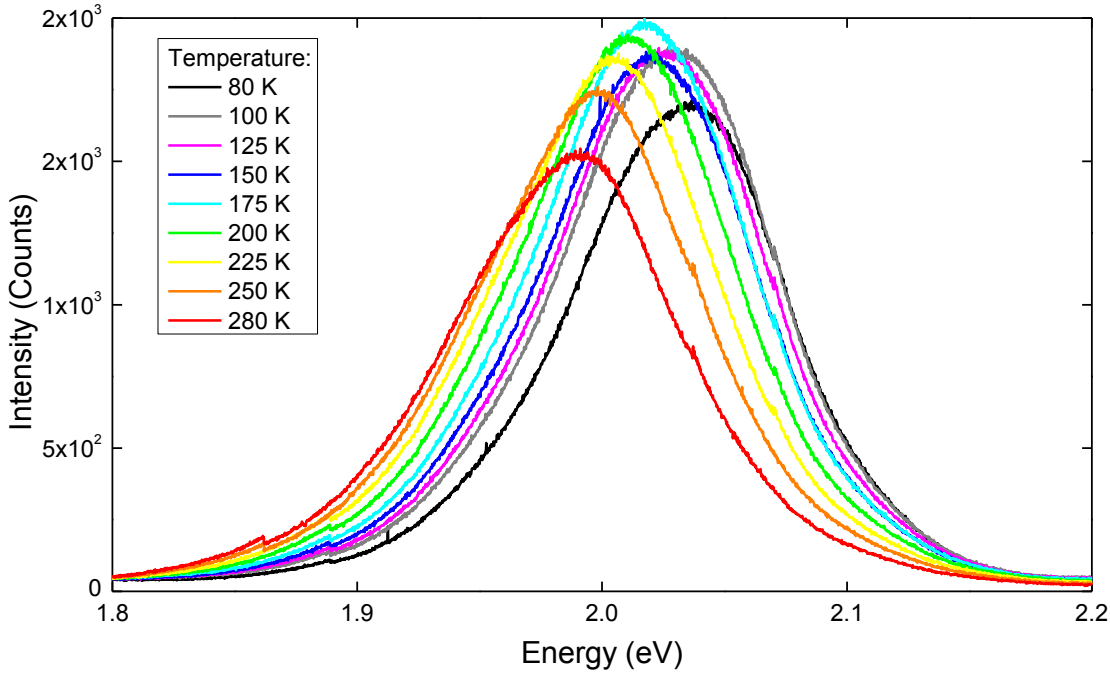

Fig. 4.8: PL spectra of Sample 4 acquired at 155 mW/cm^2 pumping and sample temperatures between 80-280 K.

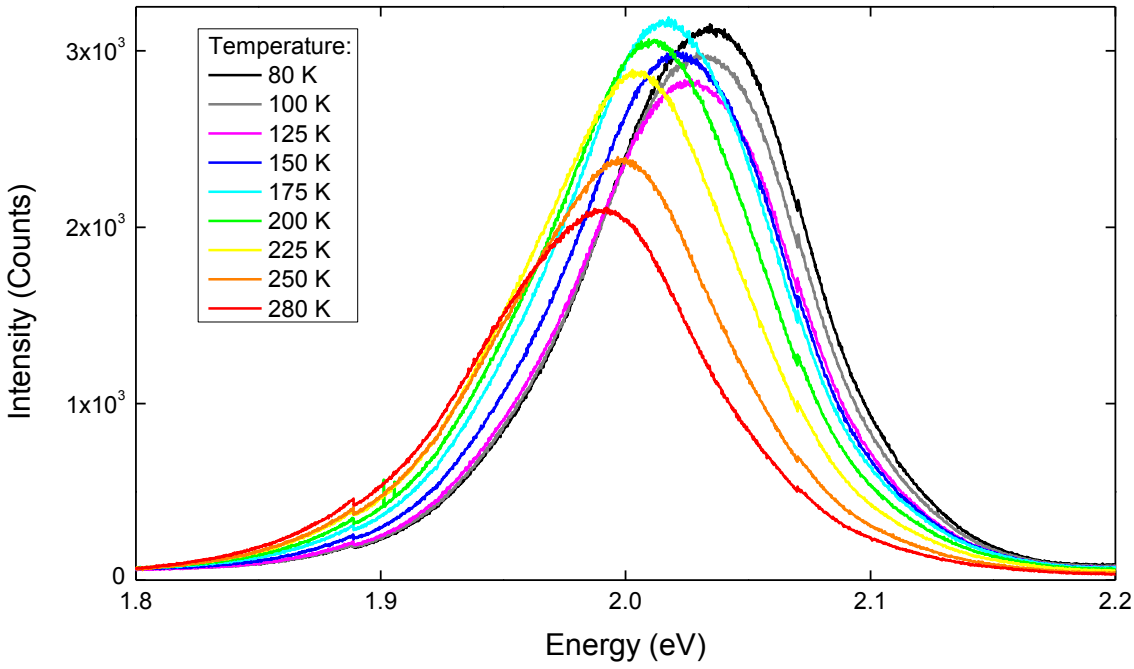

Fig. 4.9: PL spectra of Sample 4 acquired at 1410 mW/cm^2 pumping and sample temperatures between 80-280 K.

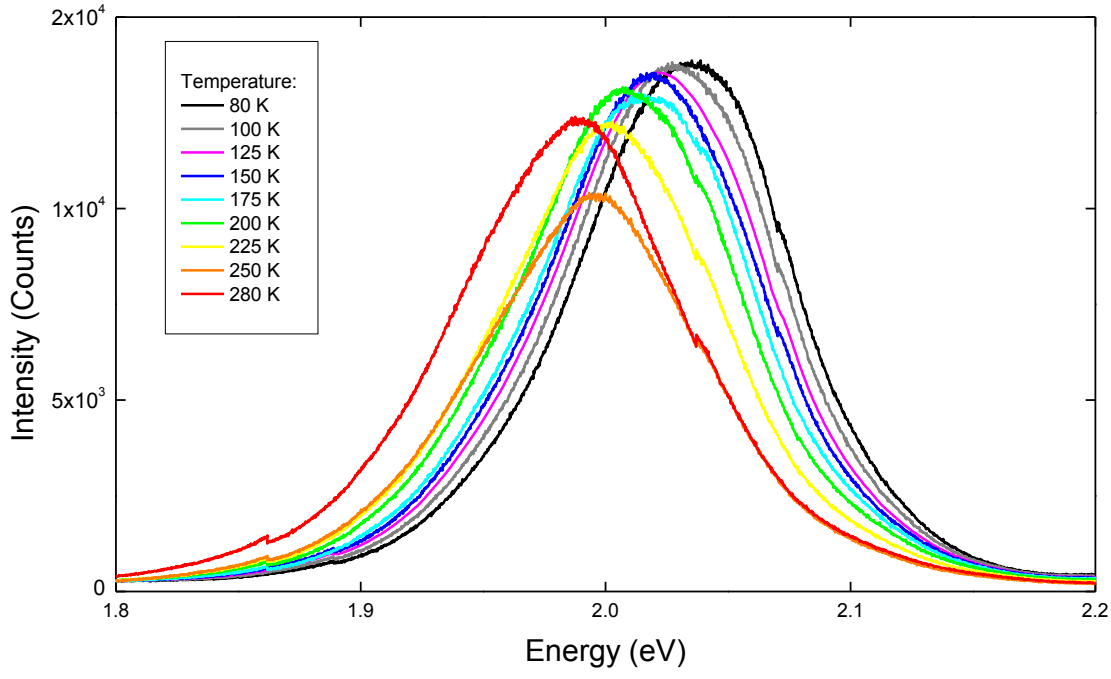

Fig. 4.10: PL spectra of Sample 4 acquired at 10,000 mW/cm^2 pumping and sample temperatures between 80-280 K.

Table 4: Data acquisition conditions for temperature dependent PL spectra

Plot	PI (mW/cm^2)	Accumulations	Grating acquisitions	CCD exposure time (sec)	Approximate time per scan (sec)
Fig. 4.7	8.46 ± 0.25	10	3	2	185
Fig. 4.8	$(1.552 \pm 0.046) \times 10^2$	10	3	0.5	91
Fig. 4.9	$(1.413 \pm 0.042) \times 10^3$	10	3	0.1	68
Fig. 4.10	$(1.001 \pm 0.030) \times 10^4$	2	3	0.1	13

sample spot, are shown in Fig. 4.7. Each spectrum was averaged over ten scans while acquisitions of each scan were taken with CCD exposure times of 2 seconds. The PL signals at the lowest PIs were so weak that background signal from the surrounding environment could not be completely eliminated within the enclosed PL setup. Scans of the background signal were consequently taken with the laser shutter closed and were manually subtracted from the PL spectra in this lowest PI dataset.

The second lowest PI data was first taken with increasing temperature from 300-360 K, then decreasing from 330-80 K. Afterwards, a measurement was repeated at 125 K. This second trial at 125 K had a peak intensity that was about 14 % lower than the first trial. Furthermore, its peak intensity was ~4.5 % lower than that of the preceding spectrum taken at 80 K. Each spectrum was averaged over ten scans while acquisitions of each scan were taken with 0.5 second CCD exposure times. The spectra collected between 80-280 K are shown in Fig. 4.8.

The third lowest PI data was first taken with increasing temperature from 80-360 K, then decreasing to 330 K. Afterwards, a second trial was taken at 300 K, which increased in PL from the first by ~ 14 %. Each spectrum was averaged over ten scans while acquisitions of each scan were taken with 0.1 second CCD exposure times. The spectra collected between 80-280 K are shown in Fig. 4.9.

The data at the highest PI were first collected by increasing temperature from 300-360 K and then decreasing from 330-80 K. Trials were repeated afterwards at 125 and 225

K. The second trial at 125 K had a peak intensity that was 7 % lower than the first, while the second trial at 250 K had a peak intensity that was 1 % larger and thus not very significant. This suggests that bleaching was not significant during these two scans at 250 K; however, it is unknown whether the PL was stable between these scans as it is possible that both enhancement and bleaching could have been present. Fig. 4.10 shows the spectra between 80-280 K. Each spectrum was averaged over two scans while acquisitions of each scan were taken with 0.1 second CCD exposure times.

Characteristic temperature dependent behaviour observed in the spectra in Fig. 4.7-Fig. 4.10 are a decrease in peak energy and spectral broadening with increasing temperature. These features are investigated further in Sections 4.3.4 and 4.3.5, respectively.

4.3.3. Quantum efficiency temperature dependence

The quantum efficiency was calculated based on the energy that was emitted by the cQDs versus the energy absorbed from the laser. This is similar to finding the number of photons emitted versus those absorbed. The relationship between detected PL and PI given by the expression in Eq. (22) in Chapter 2 was used. The total detected PL power was plotted as a function of PI at each temperature. This relationship was modelled by Eq. (22) for the linear regime, in which the slopes of these plots are a product of: the detection efficiency of the experimental setup, the cQD quantum efficiency, and the sample absorption cross section. The detection efficiency was both calculated and measured, as reported in Appendix B. The sample's absorption cross section can be determined by Eq. (23), taking the estimate of the number of cQDs pumped in the measurements and multiplying it by a single particle absorption cross section value. This is an isolated particle assumption, not strictly valid in our case, but sufficient to illustrate the methodology.

The total PL power under each spectrum, for the temperature dependent PL data shown in Fig. 4.7-Fig. 4.10 from 80-280 K, is plotted as a function of PI in Fig. 4.11. The total PL power was found by first converting the wavelength data on the horizontal axes of the acquired spectra into photon energies in units of eV. The detected count values were multiplied by their corresponding photon energies to find the energy detected at each frequency. The total detected PL energy was found by summing all the energy data points under the spectrum. The total detected power under each spectrum was finally found by dividing the total energy by the CCD exposure time.

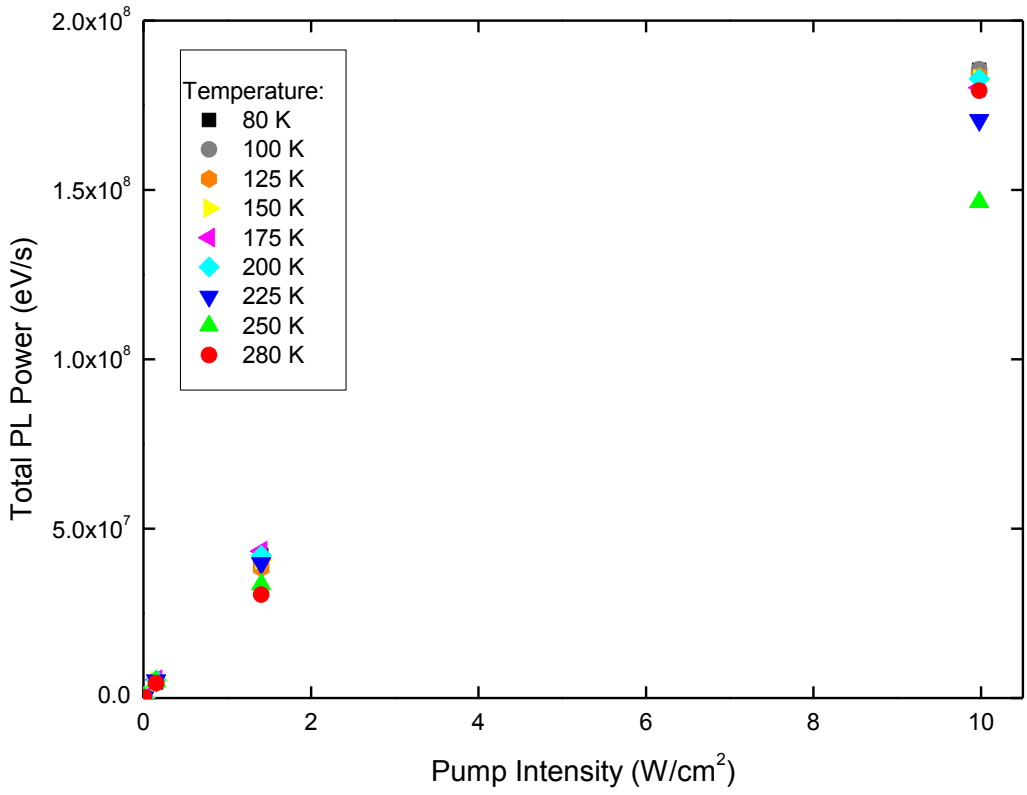

Fig. 4.11: Total PL power as a function of PI for low pump intensities of Sample 4.

To differentiate the two lowest PI data points, the data in Fig. 4.11 are shown on logarithmic axes in Fig. 4.12. Both of these figures suggest that the relationship between the total PL power and PI is linear for these low PI values and that the relationship can be represented by Eq. (22) with N as the total PL power and P as the PI. It was noted in Fig. 4.3; however, that bleaching was present at the highest PI of 10,000 mW/cm^2. The relationship between the three lowest PI data was thus compared to that between all four PI data by means of linear fits in Origin to determine whether the bleaching in the highest PI data was significant. These linear fits were forced through the origin by definition that PL requires optical pumping of the sample.

Fig. 4.13 shows three sample linear fits that were performed on the three lowest PI data in Fig. 4.11 on log-log plots for easy comparison of the three data points. The best fit that gave a minimum slope error is shown in (a), which was the fit through the data taken at 80 K. The worst fit is shown in (b) for the 250 K data, in which the second lowest PI data

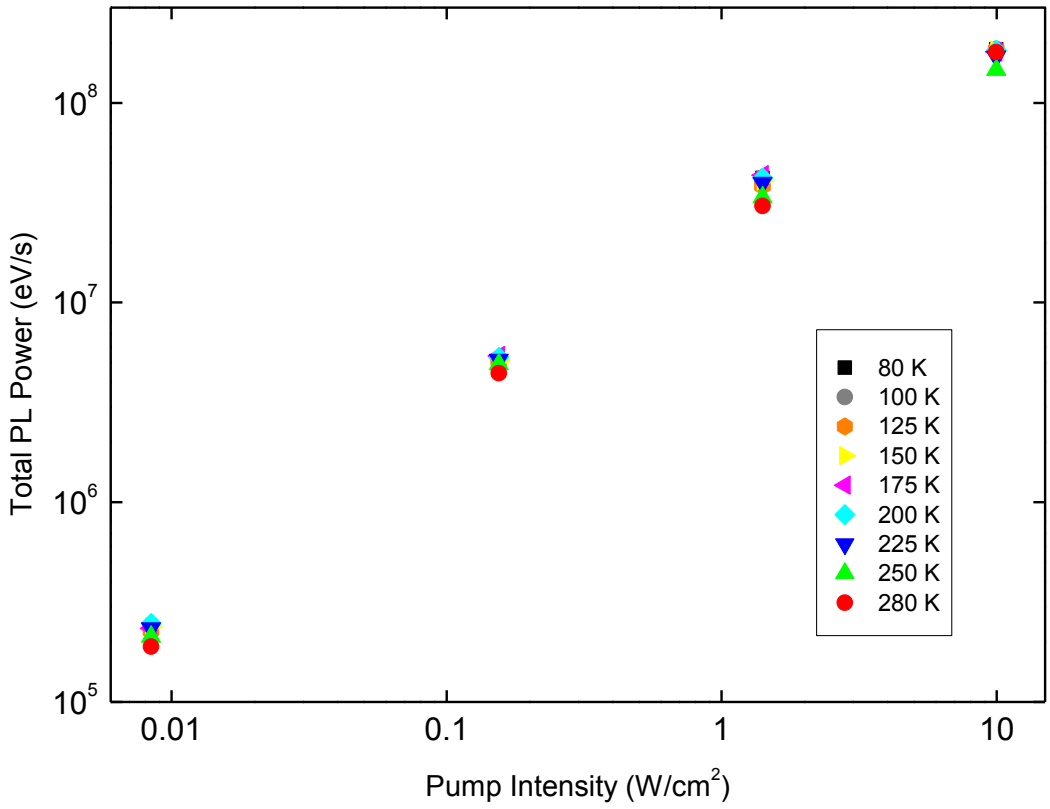

Fig. 4.12: Log-log plot of total PL power as a function of PI for low pump intensities of Sample 4.

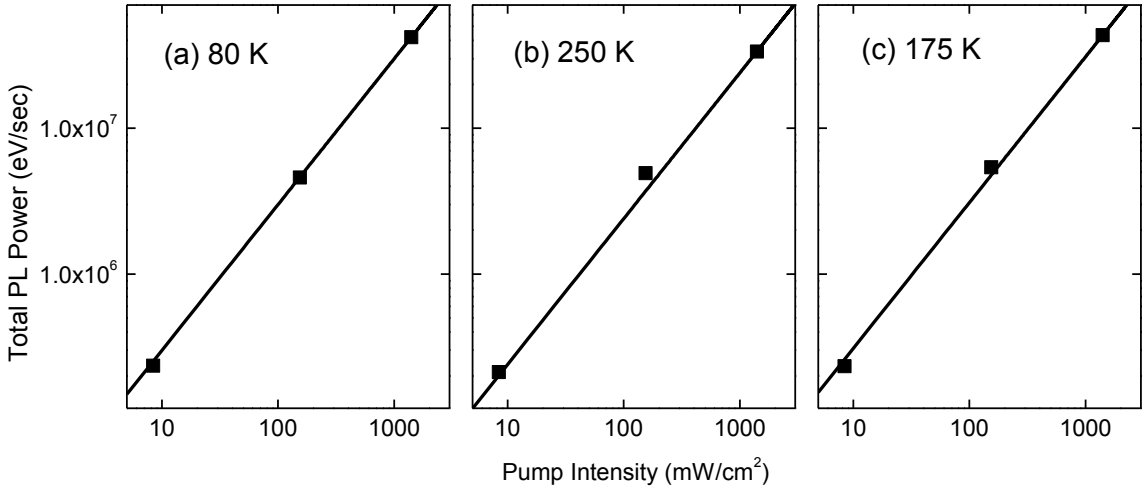

Fig. 4.13: Representative linear fits through the three lowest PI PL data of Sample 4, shown in Fig. 4.11 and Fig. 4.12, of the (a) best, (b) worst, and (c) typical fits. Data is shown on log-log plots.

deviates from the fitted line. A typical fit is shown in (c) for the 175 K data. In this latter plot, the second lowest PI data point has a smaller deviation from the fitted line than the point in (b); however, all three plots show that the lines fit the data fairly well.

The temperature dependence of the slopes obtained from the linear fits through the non-bleached total PL power versus PI data, at the three lowest PIs, is shown in Fig. 4.14. These slopes are normalized with respect to the maximum value. The error bars come from the slope uncertainties resulting from the linear fits. The linear regression analysis, done in Origin, determines these uncertainties statistically by calculating the scatter in the data points about the fitted line.

As this data is representative of the linear regime, Eq. (22) shows that the slope, m, of each linear fit is given by the product $m = D\sum\eta$. The vertical axis of this plot can therefore be described as the relative quantum efficiency scaled by the detection efficiency and the absorption cross section. If the absorption cross section was known for this cQD sample, the quantum efficiency η could be calculated. We first present a qualitative

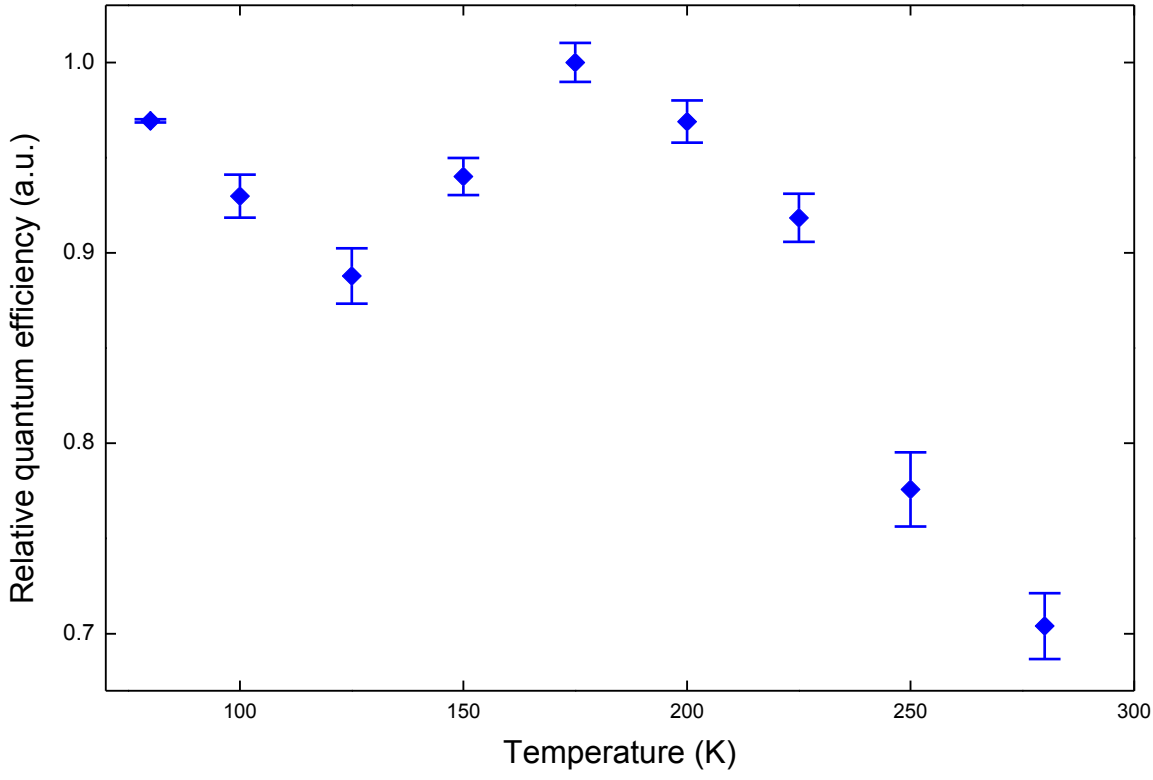

Fig. 4.14: Temperature dependence of the cQD quantum efficiency for Sample 4 scaled by the sample absorption cross section.

discussion on the temperature-dependence of the quantum efficiency. A sample calculation of the quantum efficiency using an absorption cross section for a single cQD particle follows.

The data suggest the presence of at least two different temperature-dependent non-radiative processes. The first regime, from 77-180 K, shows a strong fluctuation about a nominally constant level. The second regime, from 180-280 K, appears quasi-exponential. The first thermally activated process is possibly due to carrier trapping at the core/shell and shell/ligand boundary, as argued by Valerini et al. [29]. The second process arises due to thermal escape from the QD via phonon scattering. The fluctuations in the lower temperature regime may be a result of temperature-dependent FRET behaviour between the closely packed cQDs.

Sample quantum efficiency calculation:

A sample quantum efficiency calculation is now shown. As previously stated, the slope in Eq. (22) is equal to $m = D\Sigma\eta$, from which η can be calculated as follows for a given slope:

$$\eta = \frac{m}{Dn'\sigma} \tag{31}$$

Note that this equation uses the relation in Eq. (23) for the sample`s absorption cross section.

Fig. 4.14 shows that the highest quantum efficiency of the circles occurs at 175 K. This data point had a slope of

$$m = 30874 \frac{\text{eV/s}}{\text{W/cm}^2} = (4.947 \pm 0.050)\text{x}\, 10^{-12}\ \text{cm}^2. \tag{32}$$

Equation (B-18) showed that the calculated detection efficiency was D_{Calc} = 9.93 x 10^{-4}. Equation (B-23), on the other hand, showed that the measured detection efficiency was D_{Meas} = 8.40 x 10^{-5}. The experimental detection efficiency is used in the quantum efficiency calculation as it represents the observed and not predicted behaviour. Also, the calculated value included numerous assumptions and used grating and CCD efficiency curves that were most likely inaccurate representations of their behaviour.

One last factor that must be considered in the detection efficiency is the reduction of the collection of PL from the pump spot size. The sample was pumped with a broad beam

of size A_P = 3.74 x 10^{-6} m^2 (see Appendix C for the measurement of this spot). The PL, on the other hand, was collected from a 100 mm focal length planoconvex lens. Although the collection spot size was not measured, the measured spot size of the 75.6 mm focal length focusing lens, also shown in Appendix C, is used as an approximation. The collection spot has size A_C = 5.54 x 10^{-9} m^2, and the detection is therefore,

$$D = \frac{A_C}{A_P} D_{Meas} = 1.24 \text{ x } 10^{-7}. \quad (33)$$

The number of cQDs pumped was n' = 2.83 x 10^{13}. This value was determined by using the values found in Chapter 3 for the estimated number of cQDs on the slide of n = 6.02 x 10^{14} and the slide area covered by the QDs, A_S = 8 x 10^{-5} m^2, along with the measured pump beam spot area A_P as follows,

$$n' = \frac{A_P}{A_S} n = 2.84 \text{ x } 10^{13}. \quad (34)$$

Although the sample consisted of tightly-spaced cQDs, the single-particle absorption cross section given in the literature [37] for CdSe cQDs below was used as an approximation.

$$\sigma = (5.50 \text{ x } 10^5) a^3 \, cm^{-1} = 4.40 \text{ x } 10^{-15} \text{ cm}^2, \quad (35)$$

The parameter a is the cQD radius, which is 2 nm for the samples used in this work.

The quantum efficiency was therefore found by substituting Eq. (32) – (35) into Eq. (31) to give:

$$\eta = 3.21 \text{ x } 10^{-4}. \quad (35)$$

This unrealistically low value may be solely due to an inappropriate value of the absorption cross section. Its calculation is included purely as an illustration of the analysis methodology.

4.3.4. Band gap temperature dependence

The PL spectra in Fig. 4.7-Fig. 4.10 show a general trend of increasing peak energy position with decreasing temperature. This relationship is plotted in Fig. 4.15, for the PI data at (a) 8.46 mW/cm^2 in black squares, (b) 155 mW/cm^2 in red circles, (c) 1410 mW/cm^2 in green up triangles, and (d) 10,000 mW/cm^2 in blue down triangles. Solid symbols represent first trials of data collected at the corresponding temperature and PI, while hollow ones show second trials at particular temperatures.

The individual peak energy position data points were determined by first smoothing the data with an adjacent averaging method and then fitting the top ~10-20 % of the smoothed spectra to a peak function. As the spectra have non-Gaussian shapes, most of them were fit to an asymmetric curve. The Asymmetric double sigmoidal (Asym2Sig)

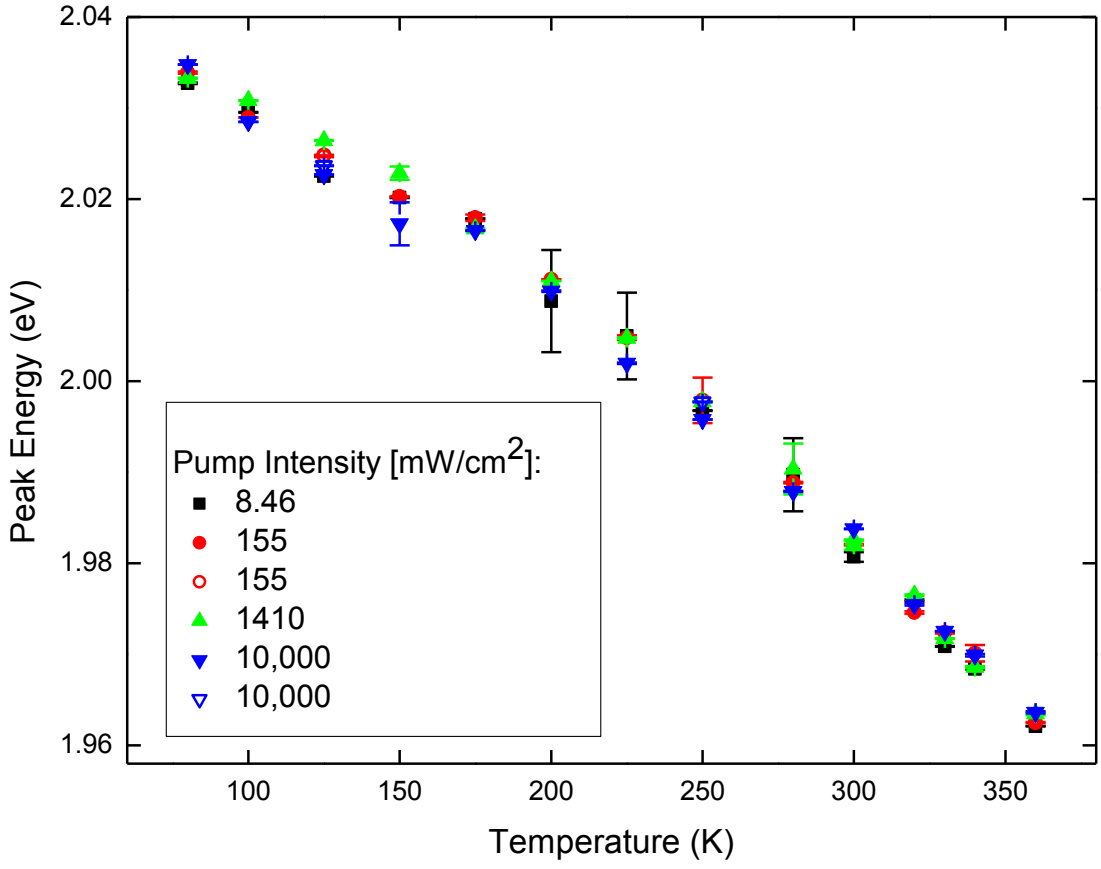

Fig. 4.15: PL peak energy position as a function of temperature for low PI data of Sample 4: (a) 8.46 mW/cm^2 in black squares, (b) 155 mW/cm^2 in red circles, (c) 1410 mW/cm^2 in green up triangles, and (d) 10,000 mW/cm^2 in blue down triangles. Solid symbols show initial trials of measurements undertaken at the indicated PI and temperatures. Hollow symbols show repeated trials.

function gave the best fit to most of the spectra, and is given by the following equation:

$$y = y_0 + A\left(1 + e^{-(x-x_c+w_1/2)/w_2}\right)^{-1}\left(1 + e^{-(x-x_c-w_1/2)/w_3}\right)^{-1}, \quad (36)$$

where x and y are the independent and dependent variables, respectively. This function has six parameters: the vertical offset given by y_0, the amplitude by A, the horizontal centre position by x_C, and three width values w_1, w_2, and w_3, where w_2 and w_3 determine the asymmetry of the peak. The value of x_C was used as the peak energy position. Samples of fitting the Asym2Sig function to some of the spectra are shown in Fig. 4.16 - Fig. 4.19.

The error bars in Fig. 4.15 come from the deviation in the fitted peak positions the spectral data. The larger error bars in some of the peak positions are due to the difficulty in finding an appropriate asymmetric function to best fit the data. The worst fit is shown in Fig. 4.16, typical fits are shown in Fig. 4.17 and Fig. 4.18, and the best fit is shown in Fig. 4.19. Fig. 4.16 shows the spectrum taken at 200 K for a PI of 8.46 mW/cm^2 with a rather high uncertainty of 6 x 10^{-3} eV in its peak position, while the uncertainties from the other three spectra are one or two orders of magnitude lower. The uncertainty in Fig. 4.16 was consequently determined manually, by examining the fitted and smoothed curves with respect to the spectrum to estimate the range within which the peak position was located. This manual determination of peak position uncertainty was performed for a few of the spectra for which the ASym2Sig function did not accurately parameterize the data.

The data in Fig. 4.15 were averaged over all PIs and fit to the Varshni function, shown in Eq. (26), by a nonlinear least squares curve fitting algorithm in Origin. The averaged data and fitted curve are shown in Fig. 4.20. The Varshni parameters given by the fit, along with the accepted literature values [29] for bulk CdSe, are listed in

Table 5. This table shows that the PL data from our QDs give a band gap energy value at 0 K of 2.0395 ± 0.0001 eV, which is larger than the bulk CdSe value of 1.85 eV. The large value for the cQDs is in agreement with the fact that the confinement energy increases the band gap energy.

The cQDs' value for α was (3.70 ± 0.05) x10^{-4} eV/K and for β was 266 ± 9 K, which each lie within the range of the corresponding accepted literature values for bulk CdSe and

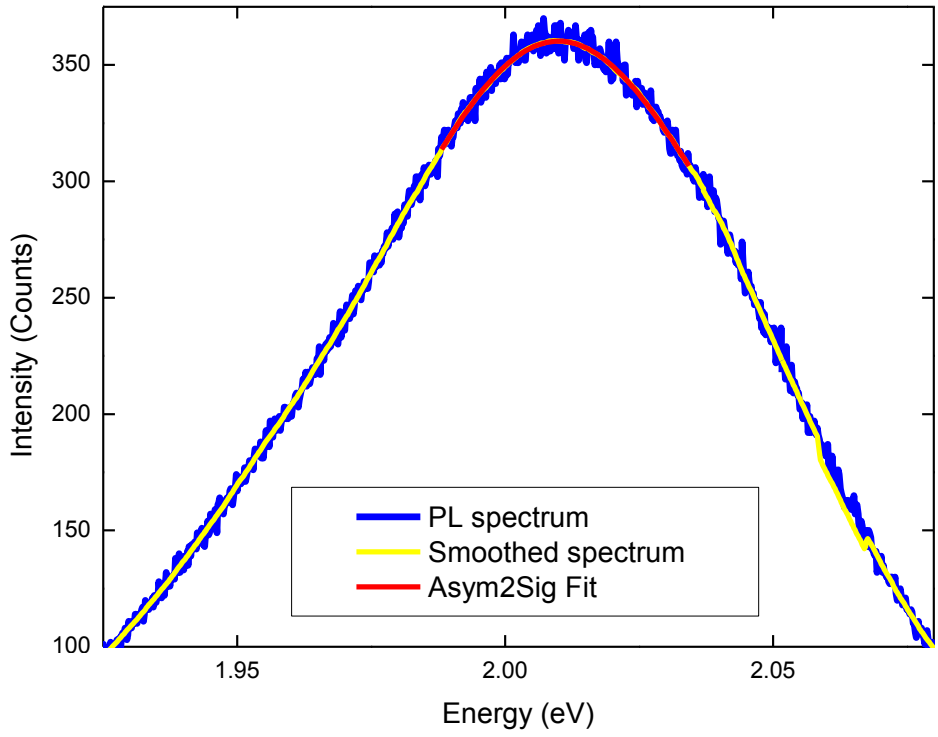

Fig. 4.16: Worst fit for PL spectrum at 200 K of Sample 4 under 8.46 mW/cm^2 PI. PL spectrum in blue, smoothed data in yellow, and ASym2Sig fit in red. Peak position uncertainty ± 6 x 10^{-3}eV.

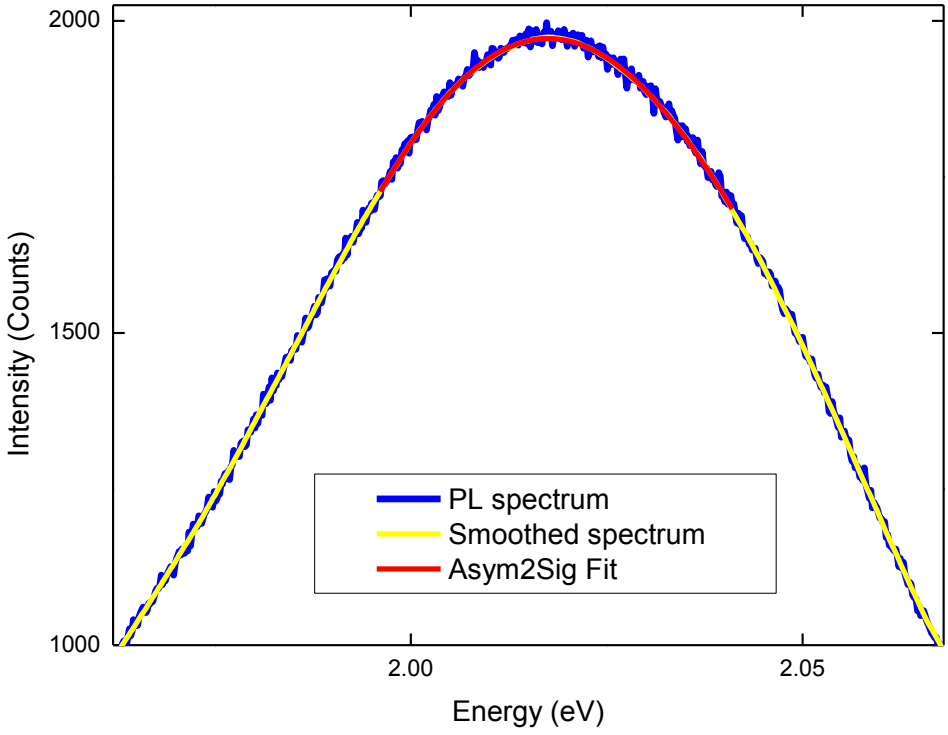

Fig. 4.17: Typical fit for PL spectrum at 175 K of Sample 4 under 155 mW/cm^2 PI. PL spectrum in blue, smoothed data in yellow, and ASym2Sig fit in red. Peak position uncertainty ± 4 x 10^{-4}eV.

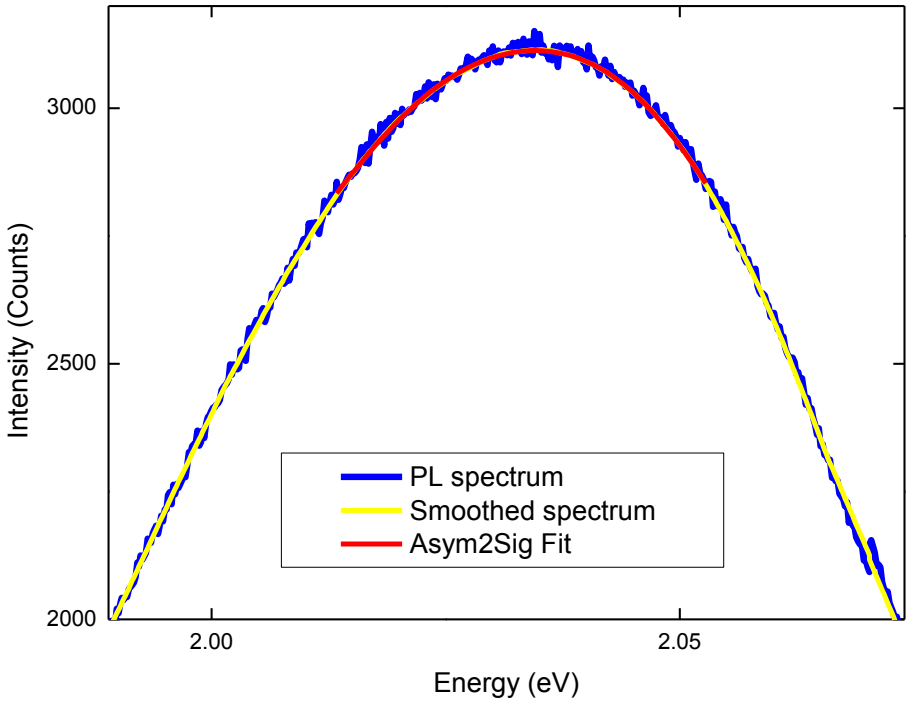

Fig. 4.18: Typical fit for PL spectrum at 80 K of Sample 4 under 1410 mW/cm^2 PI. PL spectrum in blue, smoothed data in yellow, and ASym2Sig fit in red. Peak position uncertainty was ± 8 x 10^{-5}eV.

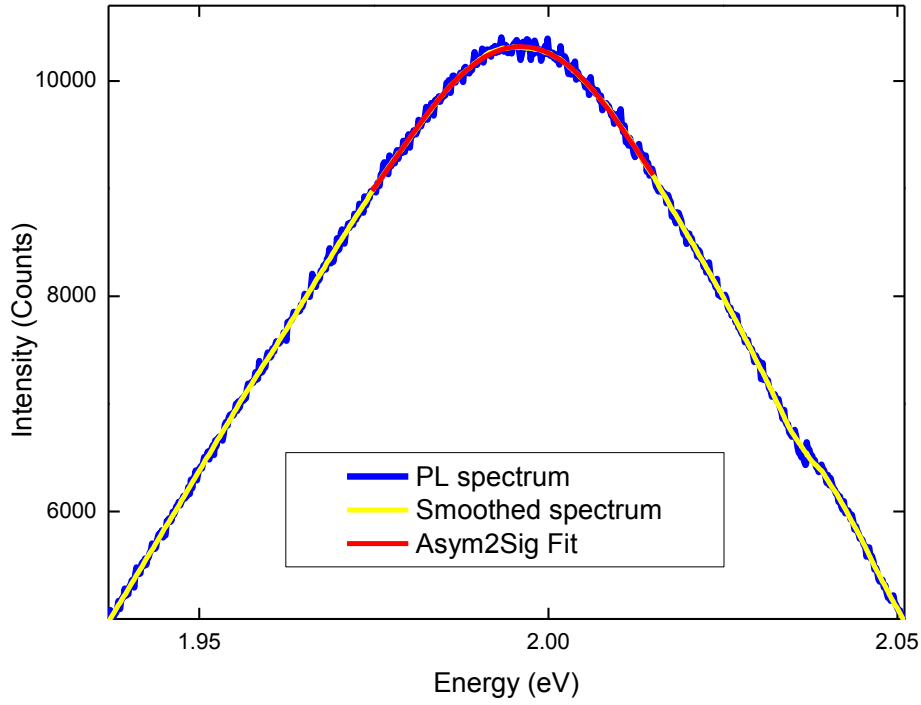

Fig. 4.19: Best fit for PL spectrum at 80 K of Sample 4 under 10,000 mW/cm^2. PL spectrum in blue, smoothed data in yellow, and ASym2Sig fit in red. Peak position uncertainty was ± 1 x 10^{-5}eV.

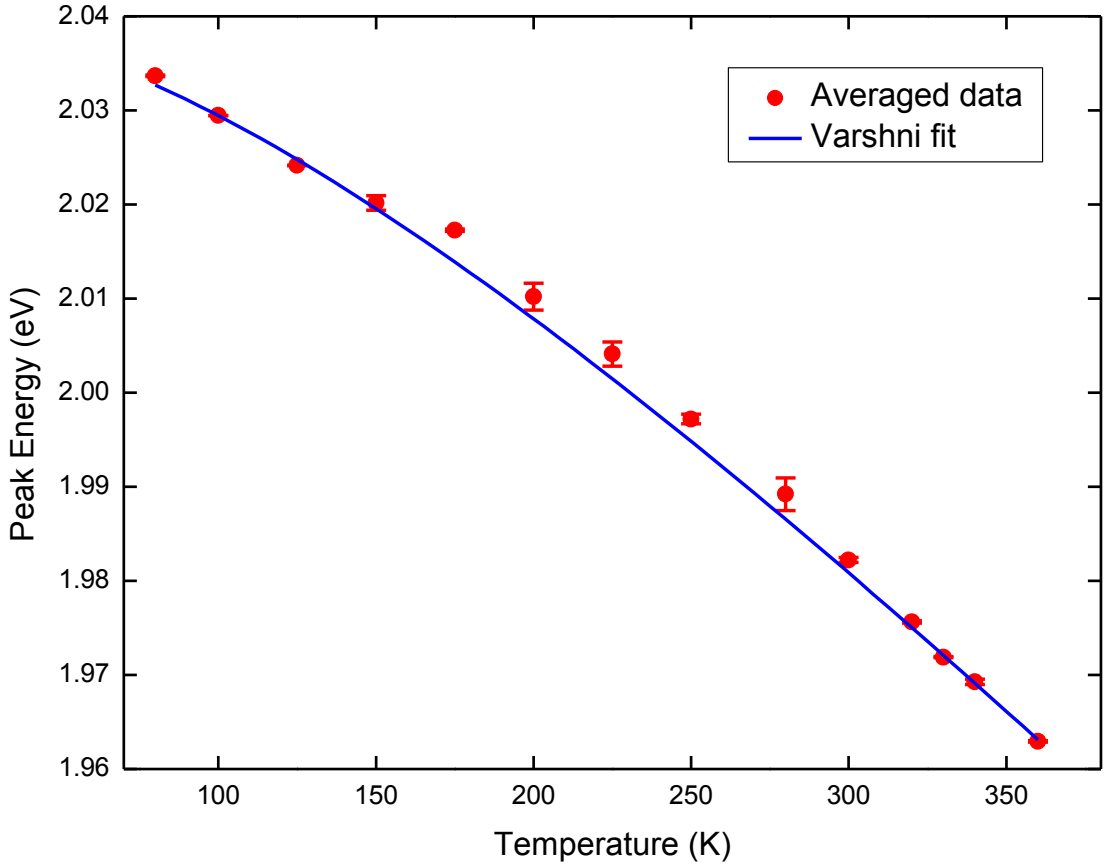

Fig. 4.20: PL peak position as a function of temperature. Average peak energy positions are shown by red circles while the blue line is a fit of the data to the Varshni equation.

Table 5: Varshni fit to PL data.

Parameter	**Fitted values**	**Bulk CdSe values**
Eg(0) [eV]	2.0395 ± 0.0001	1.85
α [eV/K]	(3.70 ± 0.05) x10^{-4}	(2.8 – 4.1) x10^{-4}
B [K]	266 ± 9	181 - 315

they also agree with results for CdSe/ZnS cQDs embedded in polystyrene [29]. The agreement with the bulk parameters indicates that the shift in energy with temperature is due to the change of band gap of CdSe with temperature due to thermal expansion of the lattice and carrier-phonon scattering [30]. The confinement energy of the QD, therefore, does not change with temperature.

This conclusion is supported by calculations by Valerini et al. [29] on CdSe/ZnS QDs embedded in polystyrene. They first demonstrate that impact of the maximum QD volume change with temperature over 45-300 K is about 0.5 meV, which is negligible compared to the observed energy shifts. Secondly, they have calculated the change in barrier potential on the QD due to differing temperature dependences of the CdSe core and the shell ZnS band gap energies under the finite square well model. They found a value of about 20 meV over the same 45-300 K temperature range. Assuming the CdSe/$Cd_{0.5}Zn_{0.5}S$ cQDs would give a similar value, this can also be considered a negligible shift in energy.

Note that the uncertainties from the fit are calculated due to the scatter in the data. The uncertainty in the band gap energy at 0 K is four orders of magnitude lower than the first significant digit of E_{g0}. The fit resulted in a small uncertainty for this value, because the fit more easily converges to this parameter. The small uncertainty on this value is expected to be unrealistic, and a more suitable value for E_{g0} would be 2.04 ± 0.01 eV. Lower temperatures would need to be investigated to more accurately determine E_{g0}.

The fitting process used an instrumental weighted fit to reduce the Chi-square value by the inverse of the square of the peak energy uncertainties. The resulting reduced Ch-square value from this fit was ~110 and is much larger than the expected value of 1. This may indicate that lower temperatures need to be investigated to obtain a better fit to the Varshni model, or that another model may better represent the temperature dependence of the PL data.

4.3.5. Thermal broadening

The PL spectra in Fig. 4.7-Fig. 4.10 showed evidence of spectral broadening with increasing temperature. This relationship is plotted in Fig. 4.21, for the PI data at (a) 8.46 mW/cm^2 in black squares, (b) 155 mW/cm^2 in red circles, (c) 1410 mW/cm^2 in green up triangles, and (d) 10,000 mW/cm^2 in blue down triangles. Solid symbols show first trials taken at the corresponding temperature and PI, while hollow symbols are repeated measurements at select temperatures.

The FWHM values were determined by using the spectra that were smoothed with the adjacent averaging method. The peak heights of the smoothed spectra were found using Origin's data reader tool. The energy positions of the values at the half height of the peak were similarly determined and the FWHM values were consequently found.

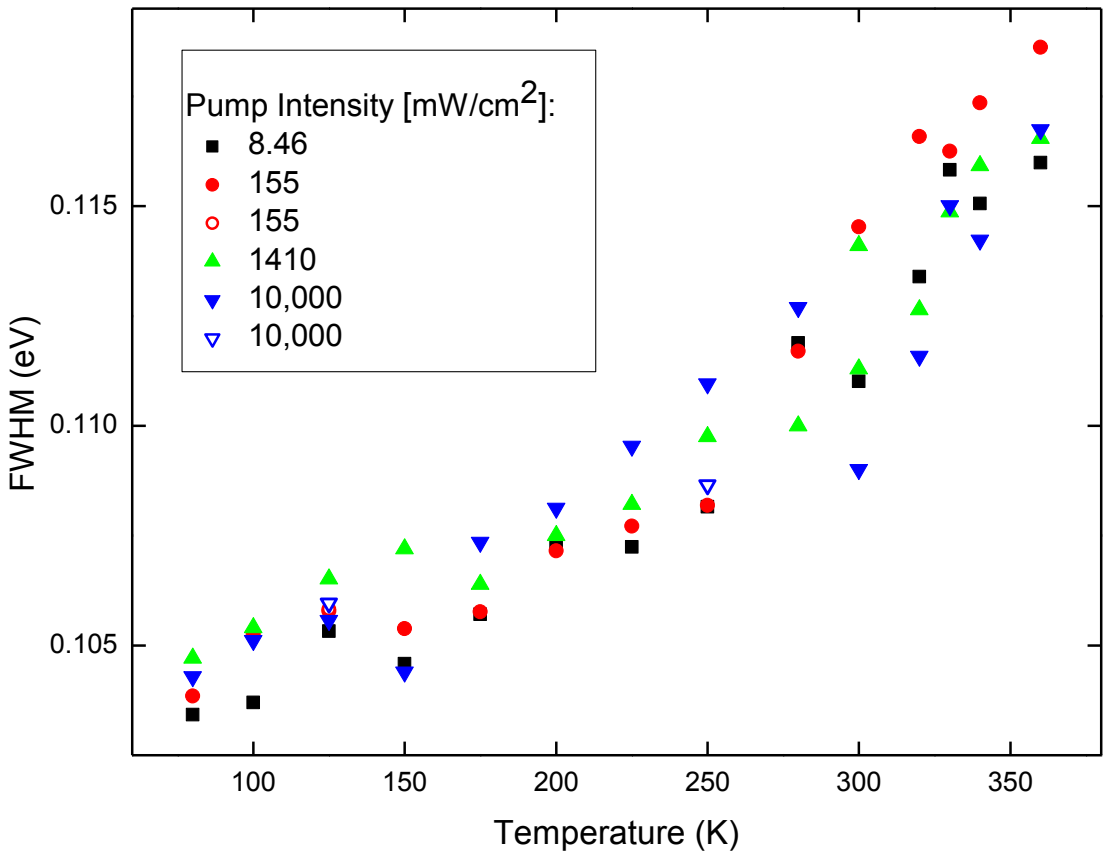

Fig. 4.21: PL spectra FWHM of Sample 4 as a function of temperature for low PI data: (a) 8.46 mW/cm^2 in black squares, (b) 155 mW/cm^2 in red circles, (c) 1410 mW/cm^2 in green up triangles, and (d) 10,000 mW/cm^2 in blue down triangles. Solid symbols show initial trials of measurements undertaken at the indicated PI and temperatures. Hollow symbols show repeated trials.

Fig. 4.22 shows the FWHM of the PL spectra, averaged over all low PI spectra, versus temperature. As the FWHM data are rather scattered at each PI in Fig. 4.21, the error bars in Fig. 4.22 come from the standard deviation in the data. The averaged FWHM data points shown by red circles were fit, using Origin's nonlinear least squares curve fitter, to the function in Eq. (27) describing excitonic peak broadening in semiconductors. The fit is shown by the blue curve. An instrumental weighted fit was done to reduce the Chi-square value by the inverse of the square of the FWHM uncertainties.

The parameters for the fit of the data to Eq. (27) are given in Table 6. Table 6 shows that the inhomogeneous broadening coefficient was found to be 103 ± 1 meV. This parameter depends only variations in the sample such as in dot size, shape, composition, etc. and does not depend on temperature.

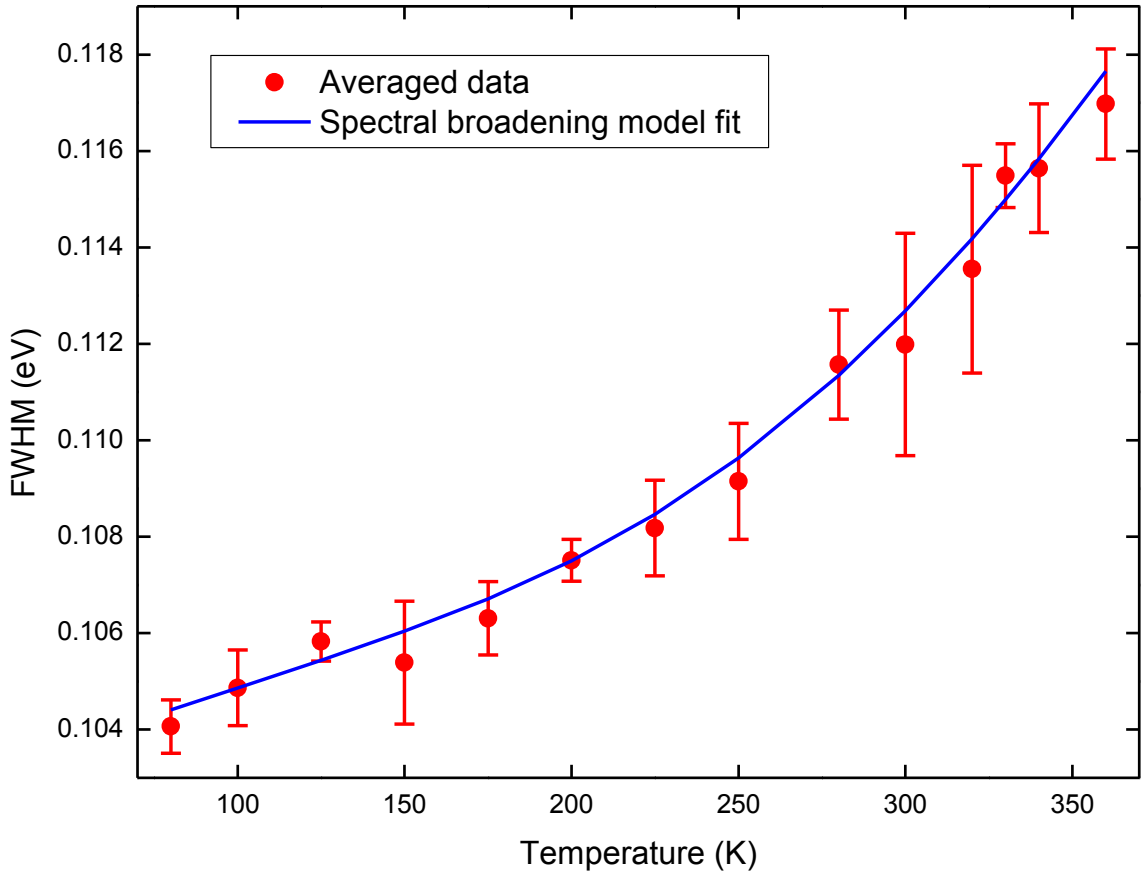

Fig. 4.22: FWHM of PL spectra of Sample 4 at various temperatures. Peak energy positions are red circles while the blue line is a fit of the data to a function describing excitonic peak broadening. The FWHM data points are averaged over those from spectra at the four low PI values.

Table 6: Spectral broadening function fit.

Parameter	**Fitted values**	**Bulk CdSe values**
Γ_{inh} [meV]	103 ± 1	---
σ [ueV]	20 ± 9	8
Γ_{LO} [meV]	400 ± 400	100
E_{LO} [meV]	110 ± 70	26.1

The other three terms come from phonon coupling mechanisms. The acoustic phonon coupling coefficient was found to be 20 ± 9 μeV, which departs from the accepted value for bulk CdSe of 8 μeV. An LO-phonon coupling coefficient was found to be 300 ±

500 meV, while the accepted value for the bulk material is 100 meV. The phonon energyassociated with the LO-phonon coupling was found to be 110 ± 70 meV, which is considerably higher than the accepted value for the bulk material of 26.1 meV.

The large uncertainties on these last two parameters make the values from the fit questionable. As the fit more easily converges to the inhomogeneous broadening coefficient, larger uncertainties are produced on the other parameters.

The larger value of σ found for the cQDs than for the bulk material is in agreement with experimental and theoretical work in the literature that acoustic phonon coupling should increase with quantum confinement [29]. Previous experimental and theoretical work also state that the quantum confinement should decrease longitudinal optical phonon coupling [29]. The value found for Γ_{LO} agrees with the accepted value for bulk CdSe within its uncertainty, however, the value for E_{LO} is much larger than the bulk value.

The Chi-square value for this fit was 0.3254, which is smaller than the expected value of ~1. A reason for this poor fit is that lower temperatures need to be investigated to more accurately determine the parameters. Moreover, the method used to determine the FWHM values of the peaks, which, suitable for finding the FWHM of Gaussian curves, is not necessarily accurate for finding the width of an asymmetric peak. If the PL peaks are indeed a convolution of two or more peaks, then finding the true width of the central peak requires a different method.

This fit, however, gives a suitable value for the inhomogeneous broadening coefficient which (although not done here) can be used to determine the QD size distribution.

Chapter 5 Conclusions and future work

The PL of CdSe/$Cd_{0.5}Zn_{0.5}S$ core/shell cQDs was studied for this thesis. A FDSW model in Chapter 2 predicted that the electronic states depended on the confinement potential due to the core and shell composition and structure. The PL showed nonlinear dependence on high PIs and gave insight into different bleaching regimes. PI-dependent PL for weak pumping showed a linear regime, from which relative cQD quantum efficiency values were determined. Temperature-dependent PL data at low PIs showed a PL peak position change with temperature and thermal broadening.

The PL temporal behaviour under constant, strong PI pumping showed significant bleaching for cQD samples in different environments: embedded in a PMMA film, on a quartz substrate in air, and on a quartz substrate in vacuum. Further PL measurements taken over a range of high PIs showed hysteresis with different bleaching regimes: a quasi-linear regime for lower PIs, a nonlinear regime beyond this showing a possible damage threshold, possibly the cause of strain relaxation at the core/shell interface, and either a second damage threshold or possible saturation at the highest PIs. These regimes were seen for the samples in two different external environments: embedded in a PMMA film and on a quartz substrate in air. The fact that similar behaviour was seen in each environment indicates that the shell sufficiently passivates the core and that PL bleaching is not caused by interactions of the charge carriers with the environment. Thus, non-radiative processes must have taken place within the core and shell structures.

All of the samples studied in this thesis were from one batch of a particular strained core/shell system. To determine the origin of the bleaching processes, one could fabricate different batches of cQDs with varying core and shell properties; for example, intentional defect sites could be placed in the core in one batch and in the shell in another. The PL can be compared from each batch to see if they exhibit the same or different type of behaviour. In addition, the saturation regime could be determined by investigating the PL at higher optical pumping.

The quantum efficiency is four to five orders of magnitude lower than expected. This is believed to be mainly due the use of a single particle absorption cross section value for a sample of closely spaced cQDs. The number of cQDs that were pumped during PL measurements was based on an estimated hard upper limit of cQDs that were on the slide. It is also possible that wavefunctions from neighbouring cQDs were interacting during PL, for instance, through FRET processes, as the high cQD concentration formed an estimated ~700-800 monolayer cQD solid. Thus, the higher than expected absorption cross section used gives a low quantum efficiency value. The qualitative behaviour of the relative quantum efficiency temperature dependence, however, showed a relationship with two regimes: a stable value below ~180 K, with some fluctuations, and a decrease above this temperature. Below 180 K, it is believed that carrier trapping at the core/shell interface and/or at the shell/ligand boundary and FRET processes dominate, while the decrease at the higher temperatures is believed to be due to an increase in phonon-carrier scattering.

To more accurately determine a quantitative quantum efficiency value, future work can include determining a better estimate of the absorption cross section. This can be experimentally determined by measuring the laser power incident and scattered from the sample. Also, the sample preparation technique can be improved using more dilute cQD solutions to create a single cQD monolayer of non-interacting cQDs. One way to optimize spin coating onto fused silica slides, which have a slippery surface, is to put silica powder onto the slide and bake it before spin coating. This creates a rougher surface which would reduce the rapid flow of the cQD solution on the slide.

The temperature-dependent PL peak position change over 80-360 K was fit to the Varshni expression. The parameters from the fit agreed reasonably well for those of bulk CdSe, showing that temperature dependence of the quantum confinement is negligible. The FWHM temperature dependence, on the other hand, was fit to an excitionic peak broadening expression which did not yield plausible values for the three parameters contributing to homogeneous broadening. The inhomogeneous broadening coefficient for the sample, however, was determined from this fit and could be used to determine the cQD size distribution in the sample. Once the size distribution is known, the inhomogeneously broadened spectrum could be theoretically generated, and the parameters relating to homogeneous broadening of the spectrum in Eq. (27) could be more accurately determined.

The variation of the PL peak energy position and FWHM with temperature could be examined over lower temperatures for more accurate determination of the temperature dependence. Temperatures as low as ~45 K could be achieved by pumping the LN2 in the cryostat with a vacuum pump, while temperature down to ~ 4 K could be achieved by placing the sample in a liquid helium flow cryostat. Investigating lower temperatures would particularly aid in obtaining more accurate parameters for the excition-acoustic phonon coupling coefficient, the excition-LO-phonon coupling coefficient, and the LO-phonon energy from the FWHM temperature dependence.

This study of a specific strain engineered core/shell cQD sample with a CdSe core and a shell structure in between that of CdS and ZnS provides insight into the sample's bleaching behaviour, quantum efficiency temperature dependence, peak position temperature dependence, and phonon scattering contribution to thermal broadening. These types of strain engineered shells are still in their early stages of research. It is important to realize the potential of these structures, such as the tunability of optical properties by only changing the strain between the core and shell and not the material composition. As was mentioned earlier, these samples can be further investigated by fabricating "extreme cases" by intentionally introducing certain properties, such as defect sites, into a particular location in the structure to study their effect on the cQD PL properties. It is also important to investigate new types of fabrication methods to be able to control specific cQD properties. Furthermore, exploring sample preparation techniques can allow one to understand how to control the cQD distribution on a given substrate. The work presented in this thesis, therefore, can be expanded upon for many possible directions of research with colloidal nanocrystals.

Appendix A Optimising spin coating for Sample 3

This section discusses the process of optimising spin coating conditions for preparation of Sample 3, in which the cQDs were embedded in a PMMA film. This sample was prepared among many trials, the first set of which were prepared on soda lime glass substrates to compare conditions such as rotation speed, cQD dilution, and solvent choice (toluene or a tolune/PMMA mixture), on the sample uniformity. In this first sample set, the ones having cQDs embedded in PMMA were more uniform. A second set of cQD samples, including Sample 3, were then spin coated in PMMA on quartz slides. Note that the soda lime glass slides were not cleaned and they were cut into 1 x 1 cm squares, while the quartz slides were circular with a 1 cm diameter and were cleaned according to the procedure described in Chapter 3 for cleaning the substrates for Sample 3. Although the first set of samples had different substrates, they gave a general idea of the final sample distribution.

The prepared samples were viewed with an Olympus 1X71 fluorescence microscope with a 488 nm excitation laser and a 100X, 1.3 N.A. oil immersion lens. Although this system could not give images resolving the individual cQDs, it still served useful to determine the dot distribution uniformity to within resolution of a few hundred nanometers. This appendix shows some photos of some of the prepared samples taken with this microscope. The dimensions of these pictures are 31 x 31 μm, which is smaller than the dimensions of the focused pump beam that was measured to be ~ 75 x 94 μm (see Appendix C). The bright spots in the photos represent areas of high cQD densities while the dark areas are regions with very low densities or lack of cQD coverage.

1) Comparison of spin coating cQDs in a toluene versus a toluene/PMMA mixture on soda lime glass

Four samples were made with the square soda lime glass substrates. The solutions P1, T1, P2, and T2 described in Chapter 3 (Section 3.1.4) were each placed in an ultrasonic bath for ~ 5 minutes to ensure the cQDs were uniformly distributed. In each case, the substrate was positioned so that it was centred on the vacuum holder of the spin coater and 60 μL of the cQD solution was dispensed onto the slide to completely cover the surface. The spin coater

was then immediately turned on for 1 minute at 3,000 rpm. Images of the prepared samples are shown below.

a) **P1:** The sample prepared with P1 was highly concentrated and looks fairly uniform within the resolution of the microscope. The sample had many regions that looked very similar to that in Fig. A.1. Figure A.1 is an image showing one of the most uniform areas of the sample. Figure A.2, on the other hand, shows one of the least uniform areas of the sample. The bright spots, indicating regions of higher cQD concentration, are relatively uniformly distributed in Fig. A.1. Figure A.2 shows some dark patches of low concentrations or no cQDs that are not as uniformly distributed as in Fig. A.1. As most of the sample looked similar to Fig. A.1, we concluded that the spin coating conditions in this case produced a reasonably uniform dot distribution.

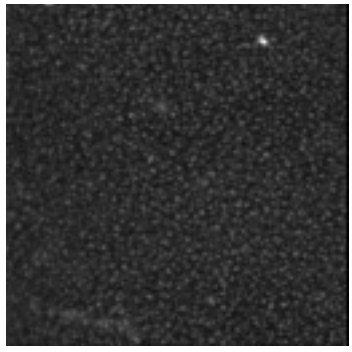

Fig. A.1: A 31 x 31 μm snapshot of a more uniform region of the sample prepared with P1 and the ordinary glass substrate. Most of the sample had a dot distribution similar to that shown in this picture.

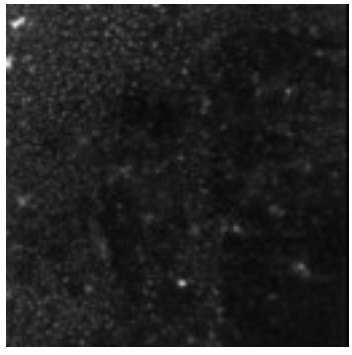

Fig. A.2: A 31 x 31 μm snapshot of one of the least uniform regions of the sample prepared with P1 and the ordinary glass substrate.

b) **T1:** The sample prepared with T1 was very nonuniform with some very low concentrated regions and some highly concentrated regions. Figure A.3 shows a region of the sample with some very bright streaks of high cQD densities next to large dark areas of low or lack of cQD coverage. Figure A.4 shows a region with very low cQD coverage. Comparing the two figures, the region of the sample in Fig. A.3 has many more cQDs than the region in Fig. A.4, so the magnitude in PL from these two regions will differ substantially at a given excitation intensity.

T1 and P1 were solutions with the same cQD concentration, however, under the spin coating conditions used, P1 produced a much more uniform sample than T1. We conclude that the addition of PMMA in P1 made the solution more viscous and allowed the cQDs to be distributed more easily at 3,000 rpm.

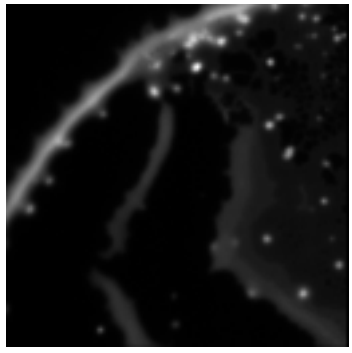

Fig. A.3: A 31 x 31 μm snapshot of one region of the sample prepared with T1 and the ordinary glass substrate. It shows large clumping of cQDs with streaks of high concentrations of cQDs next to areas of very low cQD concentrations.

Fig. A.4: A 31 x 31 μm snapshot of a region of the sample prepared with T1 and the ordinary glass substrate. This region has almost no cQD coverage.

c) **P2:** The sample prepared with P2 looked fairly uniform. It was similar to P1, but not as concentrated. There were some regions of higher concentrations than others, but

the changes in concentration from one region to another were not very drastic and were similar to that shown between Fig. A.1 and A.2 for the sample prepared with P1. Pictures were not taken for this sample.

d) **T2:** The sample prepared with T2 was very nonuniform. Figure A.5 shows a region with a streak of high cQD concentration within a large area of very low cQD coverage. Figure A.6 shows a more uniform area of cQD distribution, which did not occur as frequently on the sample as with those prepared with PMMA. Comparing these two figures with those of the samples prepared with P1 (Fig. A.1, A.2) and T1 (Fig. A.3, A.4) illustrates the lower cQD concentration in the solutions diluted by a factor of 10^2.

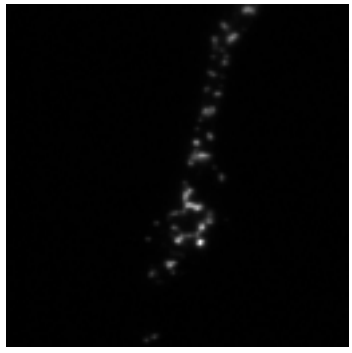

Fig. A.5: A 31 x 31 μm snapshot of a region of the sample prepared with T2 and the ordinary glass substrate. This region has almost no cQD coverage with some clumping in a streak of high cQD concentration.

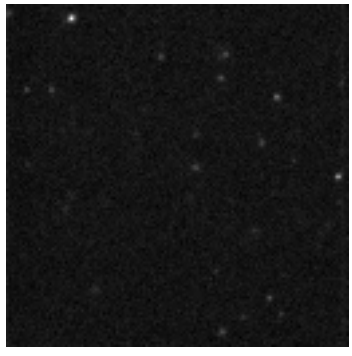

Fig. A.6: A 31 x 31 μm snapshot of a region of the sample prepared with T2 and the ordinary glass substrate. This region has a more uniform cQD distribution than in Fig. 5. Few areas on the sample had a uniform distribution.

Overall, we conclude that the addition of PMMA in the toluene solution dramatically improves the uniformity of the dot distribution. We cannot determine whether the sample is truly uniform due to the resolution of the microscope.

2) Spin coating cQDs in toluene/PMMA mixture on quartz

The fused silica substrates were prepared as in Chapter 3 and were allowed to cool after removed from the oven. Based on the results in the first sample set previously discussed only the P1 and P2 solutions were used. The samples prepared with these solutions still showed some clumping of cQDs, so the solutions were placed in an ultrasonic bath for 30 minutes before spin coating them onto the fused silica slides.

First, two samples were spin coated, each using ~ 40-50 μL of P1 on the fused silica slides at 3,000 rpm for 1 minute. A smaller quantity of solution was used than in in the previous sample set due to the smaller substrate surface area. The slides had the same diameter as the o-ring on the vacuum holder of the spin coater and a thin ring of PMMA formed on the bottom outer edge of the slide. One of these samples, viewed with the fluorescence microscope, showed a fairly uniform distribution. It is assumed the other sample had a similar cQD distribution. Figure A.7, which is representative of most regions of the sample, shows a uniform cQD distribution within the resolution of the microscope. Figure A.8 shows one of the least uniform areas of the sample. In comparison with one of the least uniform areas of the sample prepared with P1 on the ordinary glass substrate in Fig. A.2, Fig. A.8 appears to be more uniform.

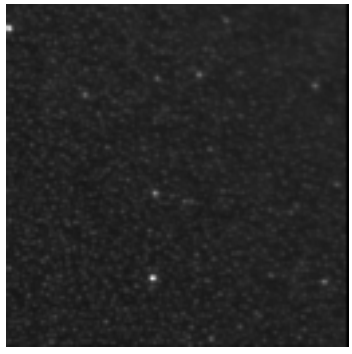

Fig. A.7: A 31 x 31 μm snapshot of a region of the sample prepared with P1 and a fused silica substrate. This region seems very uniform and represents most of the sample regions.

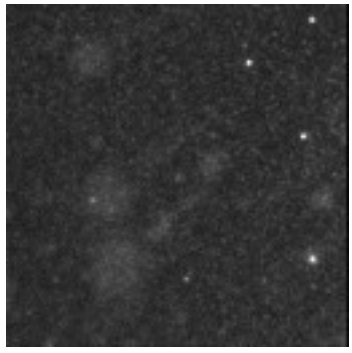

Fig. A.8: A 31 x 31 μm snapshot of a region of the sample prepared with P1 and a fused silica substrate. This region represents one of the least uniform areas of the sample, but still seems fairly uniform.

Another sample was then prepared with P1 under the same conditions as for the above two samples. This later sample is labelled "P1-2", while the sample that was not imaged in the two that were previously prepared is labelled "P1-1". The P1-2 sample is the one that was experimentally tested on and is referred to as Sample 3 in this thesis.

Next, two samples using P2 were prepared with the fused silica substrates under the same conditions as samples P1-1 and P1-2. One of the P2 samples was imaged with the fluorescence microscope and looked very uniform. Figure A.9 shows one region that is representative of most of the sample. Within the resolution of the microscope, a region was not found that noticeably differed from Fig. A.9. Thus, it was concluded that the other sample prepared with P2 is very uniform.

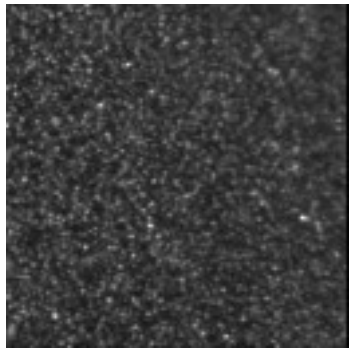

Fig. A.9: A 31 x 31 μm snapshot of a region of the sample prepared with P2 and a fused silica substrate. This region seems very uniform and represents most of the sample. A region that differed significantly from this one could not be found on the sample.

3) Summary

The results reported in this appendix have shown better sample uniformity for spin coating the cQD solutions P1 and P2 onto fused silica slides in comparison to ordinary glass substrates. Possible improvements in sample uniformity may be because the fused silica

slides were more thoroughly cleaned and also that the cQD solutions were placed in an ultrasonic bath for a longer time period of 30 minutes instead of 5 minutes to loosen any cQD aggregates. Another difference is that the circular quartz slides may have been more favourable for spin coating than the square shaped soda lime slides, however, if this factor was at all effective, it was probably very minor.

Appendix B Photoluminescence setup detection efficiency

It was shown in Equation (22) in Chapter 2 that the detected PL from the sample depends on a parameter *D*, which is the efficiency of detecting the signal. In Chapter 3 the experimental setup was described, which uses many components to transmit the signal from the sample to the CCD detector. The signal degrades along this path. This appendix shows a calculation of the transmission of light through the external optics from the sample to the spectrometer. It then shows both calculated and experimentally determined values for the transmission of light within the spectrometer from its entrance slit to the CCD detector.

B.1 Calculated detection efficiency

The transmission of the PL signal is calculated through both the external optics and the internal spectrometer optics. Note that the spectrometer's etendue is not considered in this calculation, but previous calculations comparing the amount of light the spectrometer is able to accept with the amount focused on its entrance slit showed that the PL from the sample limits the etendue. While etendue calculations require determining both the area onto which light is focused or from which it is imaged and the solid angle this spot subtends, the calculations shown in this section only consider the half angle of light at the entrance slit.

1. External spectrometer optics throughput:

Fig. B.1 shows the entrance optics used to collect and couple light from the sample (S) to the spectrometer entrance slit (ES). The marginal rays of transmitted light are shown by the red dotted lines. The source S is the light emitted from the cQD sample in the cryostat. The fraction of emitted light that is collected by the lens L2 is first calculated, which is limited by the cryostat window flange F. The transmission of light through the cryostat window, collection lens L2, matching lens L3, and the longpass filter LWP are then calculated. This is followed by a calculation of the dimensions of the focused PL light S′ on the entrance slit ES. Finally, the transmission of the light at S′ through the entrance slit is calculated. A number of assumptions are made in the calculations throughout this document and are listed in Table 7 for easy reference.

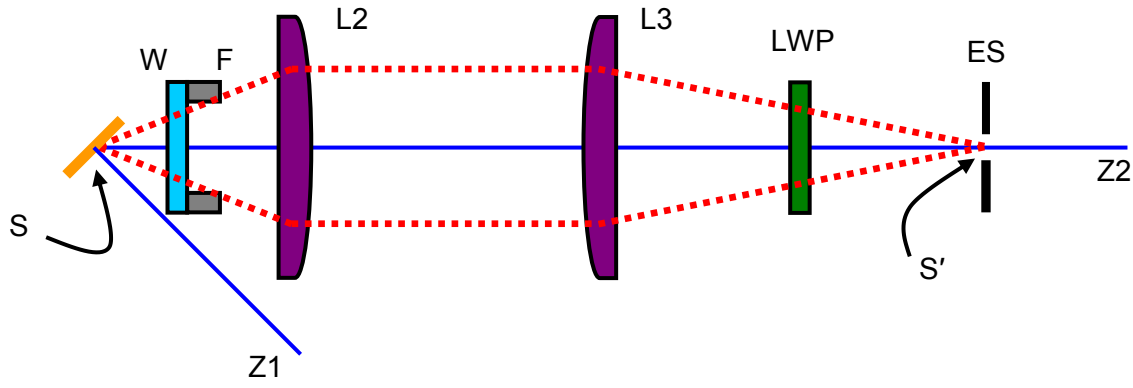

Fig B.1: Diagram of entrance optics used to transfer light from the sample to the spectrometer entrance slit. S – source, W – cryostat collection window, F – outer flange on cryostat collection window (limiting aperture for collection of light from crystat), L2 – PL collection lens, L3 – f/# matching lens, LWP – long wavepass filter, S′ - image of source at entrance slit, ES – entrance slit, Z1 – excitation axis, Z2 – collection axis. Red dotted lines show the marginal rays of luminescence collected from the sample.

Table 7: Assumptions in detection efficiency calculation

Assumption Number	Location in Setup	Description	Justification
1	S	Assume S is point-like	The distance between S and W is much greater than the Rayleigh range of the PL collection spot. Geometric optics can be used.
2	S	Assume PL is emitted uniformly over 4π sr	Light is emitted randomly from the sample.
3	S	Assume S is at centre of the cryostat	If S is not at the centre, its distance from the centre of the cryostat is negligible compared to the distance between S and W.
4	S	Assume change in optical path of light through W is negligible	The thickness of W is much smaller than the distance between S and W.
5	W, L2, L3	Assume all light rays encounter first and second surfaces at normal incidence	The paraxial approximation holds for small angles of incidence.
6	W, L1, L2	Assume no absorption losses so that all of the light not reflected is completely transmitted	Conservation of power.

7	W	Assume W is made of BK7 glass	The material of W is unknown. It is likely made of less expensive BK7 of refractive index 1.51 than fused silica with a refractive index that is less than 1 % smaller.
8	W, L2, L3	Assume reflections that are above second order are negligible	The reflectance is much smaller than the transmission between air and BK7.
9	L2, L3	Assume light is collimated between L2 and L3	The incident rays are within the paraxial approximation and spherical aberrations can be ignored.
10	L2, L3	Assume all light rays encounter spherical surfaces at normal incidence	Incident rays are within the paraxial approximation, the radii of curvature are large, spherical aberrations can be ignored.
11	LWP	Assume transmission value compensates for losses due to reflection from the second surface or that this surface has a broadband antireflection coating.	Transmission value is high that any other losses are not significant.
12	S′	Assume S′ is magnified from S by the ratio of the focal lengths of L3 to L2	L2 is placed at a distance f2 from S, and L3 is placed at a distance f3 from ES under Assumptions 2, 3, 9, and 12. The angles subtended from L2 to S and L3 to S′ are small enough that the paraxial approximation holds
13	LWP	Assume change in optical path length through LWP is negligible	The thickness of LWP is much smaller than the distance between L3 and ES.
14	S′, ES	Assume S′ has a non-Gaussian intensity distribution in that its intensity is zero outside its calculated dimensions	The calculated width of S′ contains 86 % of the light of a Gaussian beam. The width of ES is also wider than the width of S′.
15	S′, ES	Assume the total flux of S′ that falls within the dimensions of ES is accepted at the entrance of the spectrometer.	The light focused by L3 falls within the acceptance angle of the spectrometer, i.e., L3 matches the spectrometer's f/#.
16	S′	Assume that the PL is	The PL setup alignment was

		focused on the centre of ES	optimized.
17	M1, M2	Assume representative reflectance values for non-UV coated mirrors	Typical reflectance values for various types of mirrors were compared.
18	M1, M2	Assume no reflection losses between the mirror and its coating	The representative reflectance value is considerably high that any losses would be minimal.
19	G	Assume G has the same coatings as M1 and M2	This is unknown, but it is assumed for this calculation.

(1) Source (S) collection limiting aperture:

Figure B.1 shows that the fraction of light collected by L2 from S is limited by F. The solid angle Q_F subtended by the limiting aperture F on a sphere centered at S, as shown in Fig. B.2, can be calculated to determine the fraction of the total emitted light that is collected by L2 due to F (see Table 7: Assumptions 1, 2). The clear aperture of F is a disk with a measured radius a=9.5 mm at a distance b=59 mm from S (see Table 7: Assumptions 3, 4). The solid angle subtended by the projection of the disk onto a sphere of radius b centered at S is calculated as follows:

$$Q_F = \iint \frac{\hat{n}\overrightarrow{dA}}{b^2} = 2\pi b\left(\frac{1}{b} - \frac{1}{\sqrt{b^2+a^2}}\right) = 0.0799\ sr \qquad \text{(B-1)}$$

where $\hat{n}$ is a unit vector from the origin and $\overrightarrow{dA}$ is the differential area element on the disk. The fraction of radiant flux emitted over 4π sr from S that is collected by L2 is found to be

$$t_F = \frac{Q_F}{4\pi} = 0.00636. \qquad \text{(B-2)}$$

(2) Transmission through cryostat window (W):

As reflection losses take place upon propagation of light from one medium to another, the transmission of PL light through W is calculated using the Fresnel equations [14] for

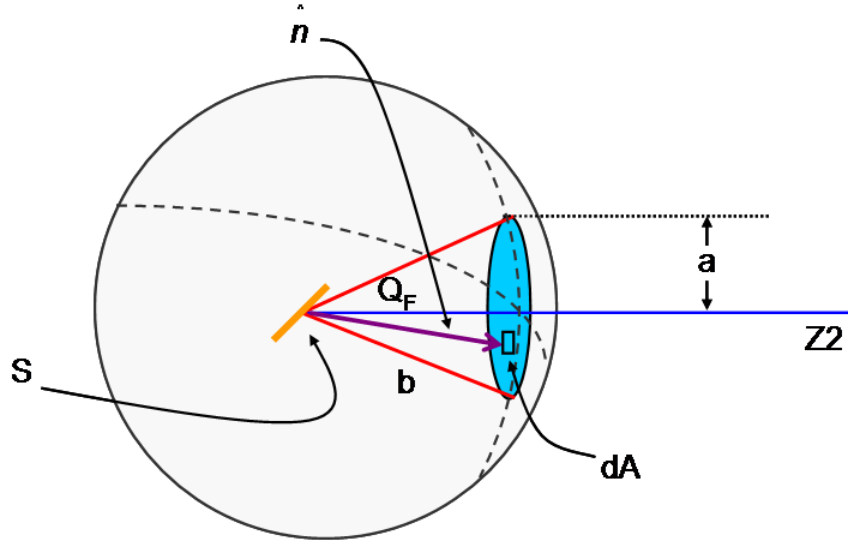

Fig. B.2: Solid angle Q_F subtended by projection of disk defining clear aperture in F of radius a onto a sphere of radius b centered at S. The vector $\hat{\boldsymbol{n}}$ is a unit vector from the origin and $\overrightarrow{dA}$ is the differential area element on the disk.

reflectance and transmittance. As the light incident on W was calculated to fall within a cone of half angle 0.16 rad, the reflectance for normal incidence (see Table 7: Assumption 5) is:

$$R = \left(\frac{n_1 - n_2}{n_1 + n_2}\right)^2, \tag{B-3}$$

where n_1 is the refractive index of the medium of incidence and n_2 is that of the medium of transmission. Assuming no losses under absorption (see Table 7: Assumption 6), the transmittance T can be found from:

$$T = 1 - R. \tag{B-4}$$

Applying Eq. (3) and (4) to the first and second interfaces (see Table 7: Assumption 7, 8), the total transmission of light through the W is found to be

$$t_W = 0.919. \tag{B-5}$$

(3) Transmission through collection lens (L2):

L2 is a plano-convex lens made of BK7 glass. Using Eq. (B-3) and (B-4), the transmission through L2 is calculated to be (see Table 7: Assumptions 5, 8, 9)

$$t_{L2} = 0.919. \tag{B-6}$$

(4) Transmission through coupling lens (L3):

L3 is a plano-convex lens made of BK7 glass. Using Eq. (B-3) and (B-4), the transmission through L3 is calculated to be (see Table 7: Assumptions 5, 8-10)

$$t_{L3} = 0.919. \tag{B-7}$$

(5) Transmission through longpass filter (LWP):

The LWP whose transmission curve is shown in Fig. 3.6 is an interference filter designed to transmit light with wavelengths longer than ~550 nm. Using transmission data supplied with the filter, an average transmission value was taken over the interval between 552 – 750 nm, where the cQD PL spectrum occurs. This average was calculated to be (see Table 7: Assumptions 8, 11)

$$t_{LWP} = 0.992. \tag{B-8}$$

(6) Image (S') of S on entrance slit (ES):

The excitation axis Z1 is perpendicular to the sample, while the collection axis Z2 is at 45º from Z1. The excitation spot on the sample is calculated in Appendix C to be circular with diameter 33.9 μm. Viewed along Z1, the spot has a height h=33.9 μm and width w=33.9 μm. The height of the spot viewed along Z2 is equal to h: h'=33.9 μm. The width viewed along Z2, however, is the projection of w at 45º: $w' = w\cos(45°)$ = 24.0 μm.

The image S′ of S occurs at ES and is magnified by the ratio f_3/f_2, where f_2 = 100 mm is the focal length of L2 and f_3 = 200 mm is the focal length of L3 (see Table 7: Assumptions 12, 13). The width and height of S′ is calculated to be: w'' = 47.9 μm and h'' = 67.8 μm respectively. The width of ES used during collection of PL spectra was at least as

large as w_{ES} = 50 μm, so the transmission of S′ through ES is 100 % (see Table 7: Assumptions 13-16):

$$t_{ES} = 1. \tag{B-9}$$

(7) Entrance Optics summary:

The total transmission of radiant flux from S to ES through the entire system of entrance optics is given by the collective transmissions calculated from Eq. (B-1), (B-2) and (B-5)-(B-9) to be:

$$t_{Entrance} = t_F\, t_W\, t_{L2}\, t_{L3}\, t_{ES} = 0.00494. \tag{B-10}$$

2. Spectrometer internal throughput:

Figure B.3 shows the optics used inside the Czerny-Turner spectrograph to transfer light from S′ at ES to the CCD detector at the exit plane. The components in this diagram are listed below. The image S′ at the entrance slit (ES) is directed to the collimating mirror (M1), which subsequently directs the light to the selected grating (G) on the grating turret (T). The dispersed light is sent to the focusing mirror (M2) which focuses the light onto the CCD detector (CCD). The InGaAs (IGA) detector was not used for measurements in this thesis.

(1) Reflection from collimating mirror (M1) and focusing mirror (M2):

The reflectivity from M1 and M2 is unknown. It is assumed for this calculation that the reflectance is flat over a broad wavelength range of ~200-2,000 nm, the working range of the spectrometer, and that it is insensitive to angle of incidence and polarization of light. As the instrument is an imaging spectrometer, it is assumed that the mirror must also have a high surface flatness (lamba/10 to lambda/20) to preserve wavefronts and a tight scratch dig (40-20 to 60-40) to reduce scatter.

Information was gathered on the reflectance of various types of mirrors manufactured by Newport Corporation. It was found that broadband mirrors are not commonly fabricated with as high reflectance values as for narrowband mirrors. The mirror having a reflectance

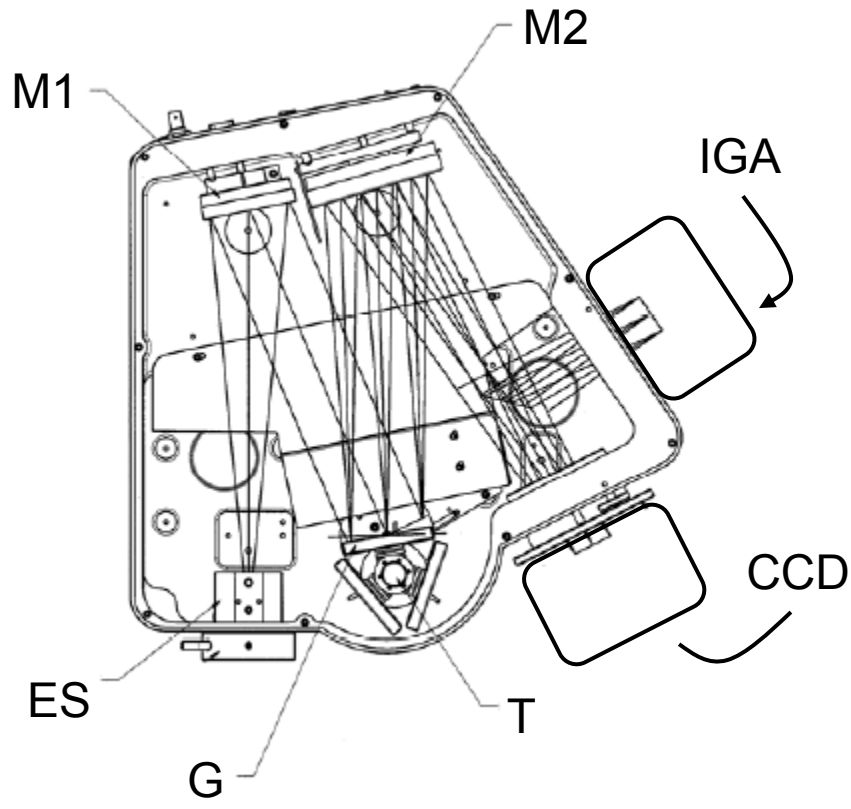

Fig. B.3: Diagram of interior spectrometer optics used to disperse light from spot S′ at entrance slit and image its spectrum at the CCD detector in the exit plane. Image courtesy of Horiba Jobin Yvon [34]. ES – entrance slit (the point at which S′ is formed), M1 – collimating mirror, G – selected grating on turret, T – grating turret, M2 – focusing mirror, CCD – CCD detector, IGA – InGaAs detector.

over the closest wavelength range to that of the spectrometer's was one with a protected silver coating, with a reflectance of 96 % over 480-2,000 nm. This value is taken as a representative reflectance for M1 and M2 (see Table 7: Assumptions 17, 18):

$$t_{M1} = 0.96 \tag{B-11}$$

$$t_{M2} = 0.96. \tag{B-12}$$

(2) Diffraction efficiency of grating (G):

The relative diffraction efficiency curves for TE and TM light for G are shown in Fig. 3.8. The PL from the cQDs has previously been measured to be vertically polarized, so the TE curve is used. An average diffraction efficiency is estimated for the interval 550 – 750 nm over which the PL spectra occur. Because data points for the curves in Fig. 3.8 were not

available, a digitizing software tool was used to extract numeric data. The average diffraction efficiency was found to be (see Table 7: Assumption 19)

$$t_G = 0.449. \tag{B-13}$$

(4) Efficiency of CCD detection:

The CCD detector's efficiency is found by combining the fraction of light illuminating its "active" area of detection with the quantum efficiency specifications of the device. Light illuminates an area of 26.6 x 6.7 mm at the exit plane giving an imaging area of A_i = 178.22 mm^2. Each pixel, having dimensions of 26 μm x 26 μm, have an area of: A_p = 676 μm^2. The detector has 1024 horizontal and 255 vertical usable pixels, so the active area of detection is A_a = 176.52 mm^2. Thus, the fraction of incident light that illuminates the active area on the detector is

$$t_A = \frac{A_a}{A_i} = 0.990. \tag{B-14}$$

Fig. 3.9 shows a sample quantum efficiency curve for the CCD detector at 25° C. Note that the detector is being used at 140 K (-133° C), however, this data is used for this calculation as it is the only information available on the quantum efficiency for the detector. A digitizing software tool was used to extract the data points on this curve. Averaging the quantum efficiency values over 550-750 nm, the wavelength range over which the PL spectra occurred, the estimated quantum efficiency is

$$t_{QE} = 0.490. \tag{B-15}$$

Thus, the fraction of light that the CCD detects under illumination is

$$t_{CCD} = t_A\, t_{QE} = 0.485. \tag{B-16}$$

(6) Spectrometer Throughput Summary:

The total transmission of light within the spectrometer is calculated with Eq. (B-11) - (B-13) and (B-16) to be

$$t_{Spectrometer} = t_{M1}\, t_G t_{M2} t_{CCD} = 0.201. \quad \text{(B-17)}$$

3. Total calculated detection efficiency:

Equation (B-10) showed that 0.00494 of the light emitted by the sample at S enters the spectrometer at ES and Eq. (B-17) showed that 0.201 of the light at ES is detected at CCD. The total throughput of radiant flux from S to CCD is thus calculated to be

$$t_{System} = t_{Entrance}\, t_{Spectrometer} = 0.000993, \quad \text{(B-18)}$$

or, 0.0993 %.

B.2 Measured detection efficiency

The internal spectrometer throughput from ES to CCD was experimentally measured and compared with the value of 20.1 % in Eq. (B-17).

Experimental Setup:

The experimental setup is shown in Fig. B.4, in which a power measurement of the 532 nm Nd:YAG laser before entering the spectrometer was compared with the total power under the recorded spectrum by the CCD detector. The four labelled paths in this diagram are described below:

1 – The laser is incident at ~ 45° on a soda lime glass slide.

2 – A fraction of the incident laser light is transmitted through the glass slide.

3 – The fraction of the incident laser light is reflected from the first surface of the glass slide. This light is focused onto the entrance slit of the spectrometer.

4 – The light focused onto the entrance slit is transmitted through the spectrometer and is detected by the CCD detector.

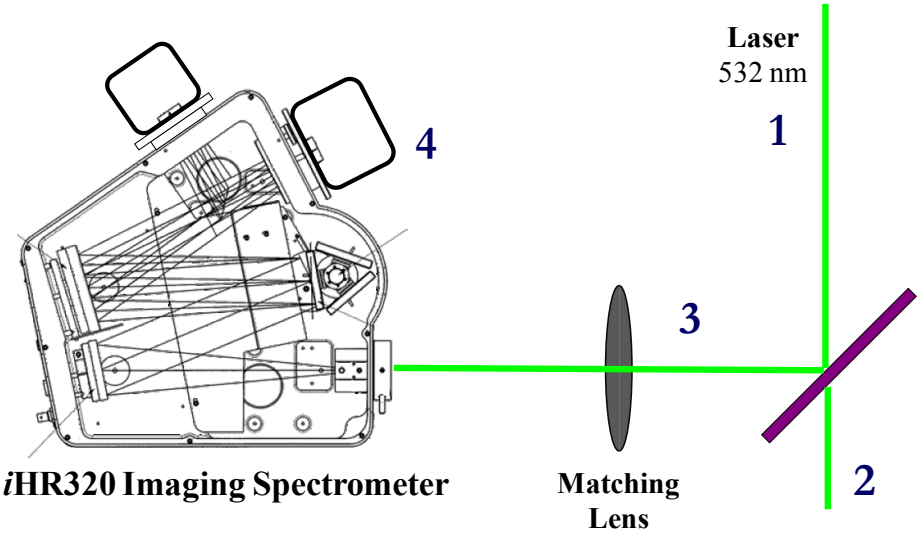

Fig. B.4: Experimental setup for determining spectrometer detection efficiency. Spectrometer diagram courtesy of Horiba Jobin Yvon [34].

Measurement and results:

1) The laser power was measured at **1** after attenuation by a neutral density filter wheel whose optical density value was fixed throughout the experiment. The power at **1**, measured with a Newport 818P-001-12 thermopile detector and an 842-PE power meter, was $P_1 = 518\ \mu W$.

2) Due to the thermopile detector's inaccuracy at lower optical powers, a stable measurement of the laser power was not achieved at **3** under the same conditions as in the previous step. The optical power measured at **1** was thus used with a calculation of the reflectance of light from the glass slide to determine the laser power at **3**. The angles of the incident beam **1** and reflected beam **3** were approximately measured as $\theta_i = 45°$ and $\theta_r = 45°$, repectively. The refractive index of the soda lime glass is taken to be 1.52. The laser light has previously been measured to be vertically polarized (perpendicular to the plane of incidence). The Fresnel equation for the reflectance of TE polarized light is [14]

$$R = \frac{n_1 \cos(\theta_i) - \sqrt{1 - \left(\frac{n_1}{n_2}\right)^2 \sin^2(\theta_i)}}{n_1 \cos(\theta_i) + \sqrt{1 - \left(\frac{n_1}{n_2}\right)^2 \sin^2(\theta_i)}} \qquad \text{(B-19)}$$

where n_1 is the refractive index of the medium of incidence and n_2 is the refractive index of the medium with the transmitted light. Using Eq. (B-19), the reflectance is calculated to be R = 0.0967 or 9.67 %.

3) The laser power at **1** was attenuated by three calibrated neutral density filters having attenuation factors of 911, 1250, and 90.0 (to avoid saturating the CCD detector). The power of the attenuated light at **1** becomes $P_1' = 5.08\times10^6$ μW. The reflectance found in the previous step is used to calculate the power of light at **3** before incidence upon the f/# matching lens: $P_3' = 4.91\times10^{-7}$ μW. The transmission of light through the matching lens found in Eq. (7) as 91.9 % is used to calculate the power of light entering the spectrometer: $P_3'' = (0.919)P_3' = 4.51\times10^{-7}$ μW, or

$$P_3'' = 2.81 \text{ x } 10^6 \text{ eV/s.} \qquad \text{(B-20)}$$

4) A spectrum of the laser was collected at a CCD exposure time of 10 seconds using the widest entrance slit of 2.24 mm to capture the power of the entire focused beam. The dark current signal from the CCD detector was automatically subtracted from the spectrum. The recorded spectrum is shown in Fig. 2.

   The spectrum in Fig. B.5 has a peak centered around 2.33 eV (~ 532 nm). Smaller peaks that extend below 2.32 eV and above 2.34 eV, which did not appear in spectra acquired at shorter exposure times, can be attributed to non-Gaussian components in the beam. A background scan at 0.1 sec exposure time showed a constant signal centered around 0 counts with magnitude below 10 counts. A background scan at a 10 second exposure time, however, was not taken.

5) The total power under the spectrum in Fig. B.5 was found by first finding the total energy of light recorded at each data point by multiplying the intensity value in counts by the corresponding energy. The total energy under the spectrum was

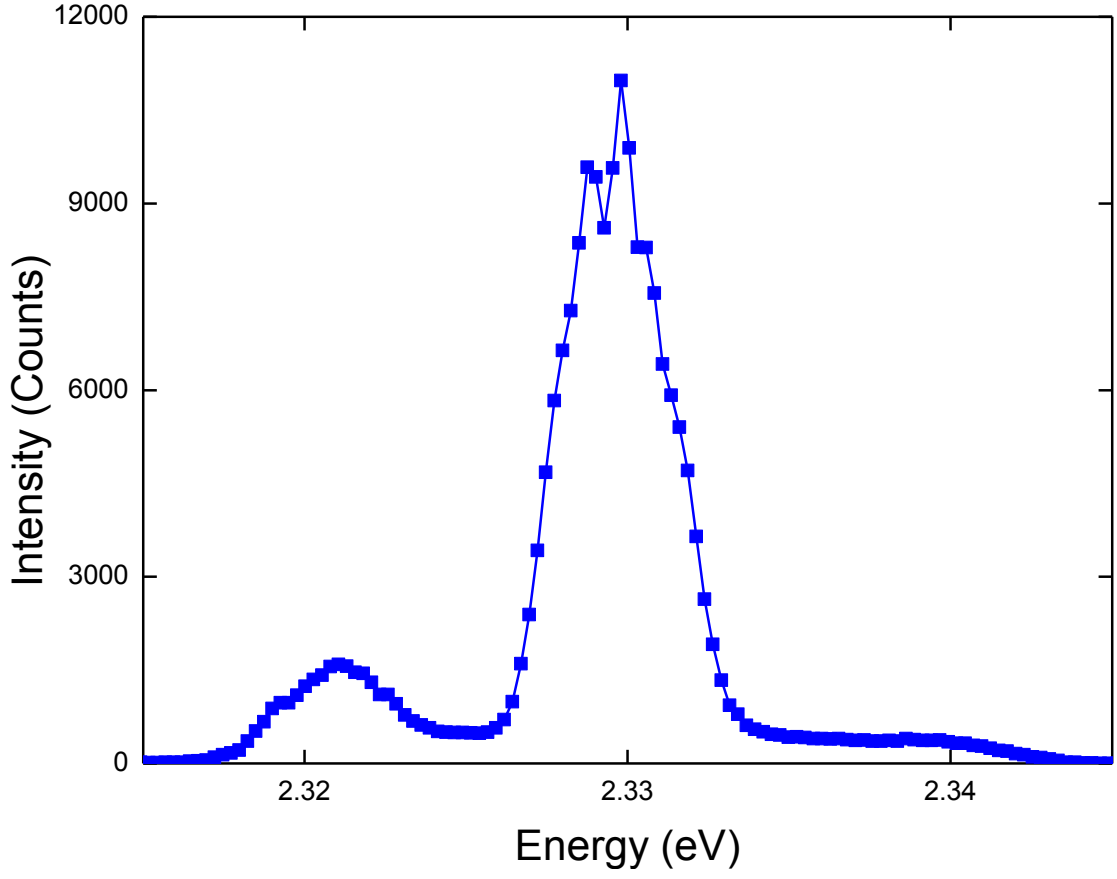

Fig. B.5: Laser spectrum.

consequently found by summing all of the total energy values. The total energy under the spectrum was then converted to the total power under the spectrum by dividing by the 10 second exposure time. The total power was found to be

$$P_4 = 47{,}000 \text{ eV/sec.} \tag{B-21}$$

Using Eq. (B-20) and (B-21), the measured detection efficiency through the spectrometer is determined to be

$$t_{Spectrometer\ Measured} = \frac{P_4}{P_3'} = 0.017. \tag{B-22}$$

The calculated value for the detection efficiency through the spectrometer in the previous section was found to be 0.201. The measured efficiency is thus an order of magnitude less than the calculated one.

Using the calculated transmission though the entrance optics from the sample to the spectrometer in Eq. (B-10), the total detection efficiency based on the measured value through the spectrometer is

$$t_{Measured} = t_{Entrance} t_{Spectrometer\ Measured} = 0.0000840, \qquad \text{(B-23)}$$

or 0.0084 %, which is about an order of magnitude lower than the calculated value determined in Eq. (B-18).

Appendix C Excitation spot size

A Gaussian beam calculation of the excitation spot size is shown in the first part of this appendix and is compared to a laser beam profiler measurement of the spot in the second part.

C.1 Calculated spot size

The laser used to pump the sample has a specified diameter of ~2.0 mm at the aperture and full angle divergence of <1.5 mrad. The diameter of the spot of the beam focused onto the sample by a f=100 mm focal length lens is calculated. The laser beam is assumed to be perfectly Gaussian, meaning that the beam is localized near the propagation axis. The Rayleigh range ($2z_0$) is first calculated to show that the beam is collimated over the distance it travels in the PL setup and that its divergence can be regarded as negligible. Next, the spot size of a focused, collimated Gaussian beam is calculated.

The laser beam is assumed a Gaussian beam propagating along the z axis. The beam is confined within a cylindrical-like boundary containing most of its energy: its maximum intensity occurs at the z-axis and the cylinder's outer boundary is defined by a transverse distance of $1/e^2$ times its maximum intensity from the z axis. The function w(z) defines the beam radius. The beam waist, or the position at which it has a minimum radius is at at z=0. The waist radius (w_0) at this point is [14]

$$w(z = 0) = w_0. \tag{C-1}$$

The Rayleigh range, related to the beam's depth of focus, is defined by z_0 as [14]

$$w(z_0) = \sqrt{2}w_0. \tag{C-2}$$

Within the range $0<z<z_0$, (or $-z<z<z_0$), the beam size does not increase very drastically and the wavefronts are planar.

At z= z_0, the wavefronts have a minimum radius of curvature. Moving along the propagation axis away from the Rayleigh range, the beam wavefronts start to become spherical. For z>> z_0 in the far field, the wavefronts are planar, with

$$w(z \gg z_0) = \frac{\lambda z}{\pi w_0}. \tag{C-3}$$

where λ is the wavelength and the (half angle) far field divergence is defined as

$$\theta_0 = \frac{\lambda}{\pi w_0}. \tag{C-4}$$

Equation (C-4) is the far field divergence for a diffraction-limited laser beam with a beam quality of M^2=1. The laser used for measurements in this thesis has a beam quality of M^2=1.2, meaning that it cannot be focused as tightly as the ideal Gaussian beam. However, it is assumed for this calculation that Eq. (C-4) approximates the behaviour of the laser beam. The following formula can be used to find the Rayleigh range:

$$z_0 = \frac{\pi w_0^2}{\lambda}, \tag{C-6}$$

with w_0=1 mm and λ= 532 nm to give z_0= 5.91 m. As the distance that the laser beam travels between its aperture and the focusing lens is much less than this value of z_0, it can be assumed that it is reasonably collimated and has no divergence at the focusing lens.

It is assumed that the beam's radius is ~ 1mm at the lens. Without loss of generality, the following formula for the lens positioned at z=0 can be used to calculate the beam waist after transmission through the lens [14]:

$$w_0^{'} = \frac{\lambda}{\pi w_0} f = \theta_0 f. \tag{7}$$

In Eq. (C-6), w_0' is the waist radius of the beam after transmission through the lens and is located at z~=f. This formula gives w_0' = 16.9 μm, and thus, the diameter of the focused spot size is $2w_0'$=33.9 μm.

C.2 Measured spot size

A laser beam profiler was placed in the PL setup to measure the spot size of the unfocused and focused laser beam. The setup is first described. The measurements of the unfocused and focused spot sizes are then shown. A calculation is then shown of the spot size at the estimated angle on the sample.

1) Setup:

A Newport LBP CCD camera laser beam profiler was used to image the 532 nm ND:YAG pump laser beam spot. Note the data in the results section for Samples 3 and 4 came from pump intensities using either a spot focused by the 75.6 mm focal length biconvex lens for the high pump intensities or with an unfocused spot. The setup is first discussed for the unfocused spot and then for the focused spot.

The LBP profiler comes with three different filters which may be used to attenuate the beam, labelled NG4, NG9, and NG10. Their respective transmission values at 532 nm are ~ 15 %, < 0.5 %, and << 0.1 %.

(1) Unfocused beam

To measure the size of the unfocused beam, the profiler was placed directly normal to the incident beam, about 20 inches from the laser. Neutral density filters with a total optical density of 5.0 were placed between the laser beam and the profiler to avoid saturating the camera. To avoid saturating the beam profiler, its gain and shutter speed settings were automatically adjusted. Also, a pinhole of ~ 3 mm in diameter was placed in front of the laser beam to reduce the noise in the measurement from the scattered laser light.

(2) Focused beam

To measure the size of the beam focused by the 75.6 mm focal length biconvex lens, the cryostat was replaced with the profiler (see PL setup diagram in Fig. 3.2). The NG4 and NG9 filters were used. The profiler was placed so that the beam was incident normal to its surface. During measurements on Samples 3 and 4, however, the beam was incident at an angle of ~18.9° to the normal of the sample.

The beam profiler was placed on a translation stage that could be adjusted along the axis of the beam path. To measure the beam at the position of focus, the micrometer actuator on the translation stage was adjusted until the smallest spot size was observed. To avoid saturating the beam profiler CCD camera, its gain and shutter speed settings were automatically adjusted.

2) Measurement

(1) Unfocused beam

The horizontal diameter was found to be 2,235 μm and the vertical diameter was found to be 2,261 μm. A screenshot of the measurement is shown in Fig C.1. Note that the beam profiler was oriented 90° from its upright position, so that the horizontal measurements correspond to the beam's vertical position, and the vertical measurements correspond to the beam's horizontal position. Note that the beam widths were taken at 13.5 % of the peak intensity, corresponding to the typical $1/e^2$ designation of the diameter of a Gaussian beam [14].

(2) Focused beam

The spot's horizontal and vertical widths were 79 μm and 94 μm, respectively. An image of this measurement is shown in Fig. C.2. The beam widths were taken at 13.5 % of the peak intensity. Also note that the beam profiler was placed at 90° from its upright position in the setup, so that its horizontal axis corresponded to the vertical axis in the PL setup and vice versa.

3) Calculation

Projection of horizontal width onto sample:

The laser beam was estimated to be incident on the sample at an angle of 18.9° from the normal as shown in Fig. C.3.

The cryostat's specifications indicate that the distance between the window to the centre is d_1 = 41.3 mm and the radius of its window is d_2 = 19.1 mm (see Fig. C.4). The

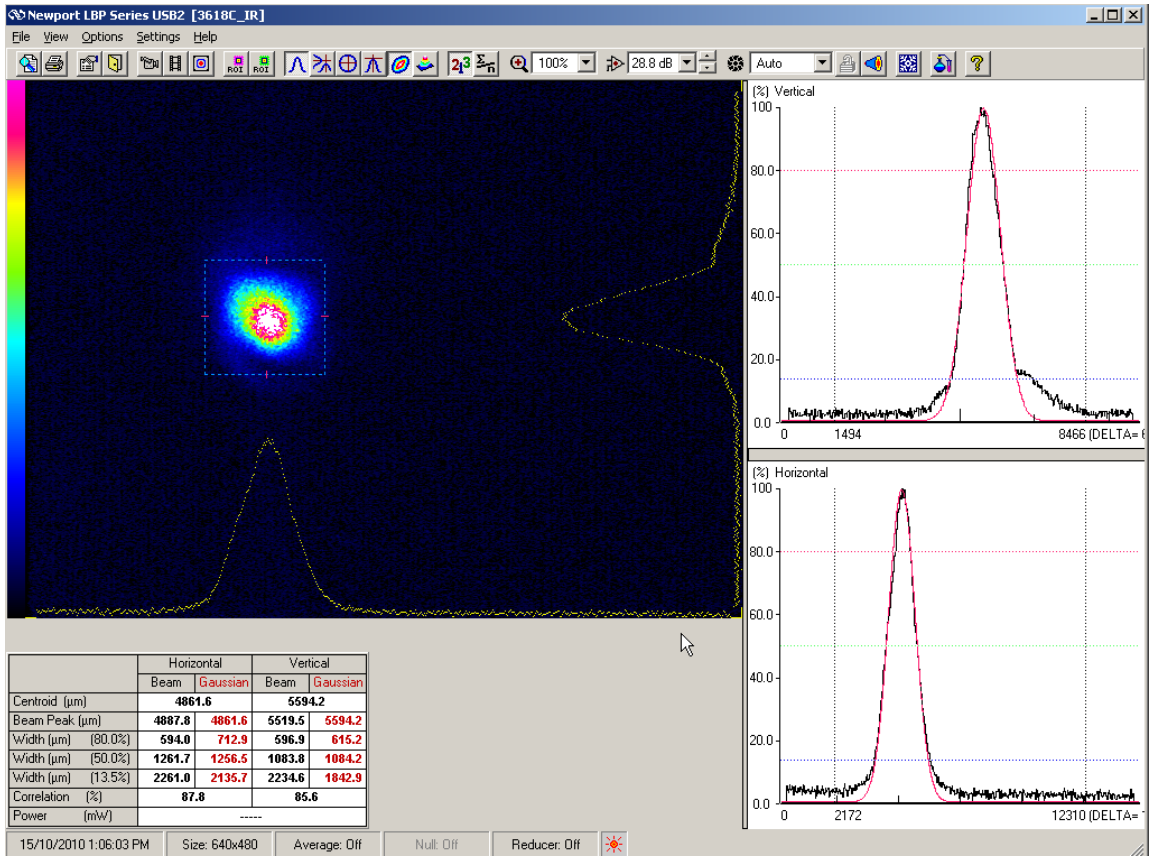

Fig. C.1: Beam profile measurement of unfocused beam. The horizontal width is 2,240 µm, shown under the column labelled "vertical", and the vertical width is 2,260 µm, shown under the "horizontal" column. The $1/e^2$ (13.5% of the peak intensity) width was used.

distance between the outer edge of the window to the spot where the pump beam enters the cryostat was measured to be $d_2 - d_3 \approx 5$ mm. Therefore, $d_3 = 14.1$ mm and Fig. C.3 shows that the angle can be calculated to be $\theta = 18.9°$.

The beam profiler measurements, made with the beam at normal incidence, can therefore be used to calculate the projection of the horizontal component on the sample with this angle. Note that the measured vertical component does not need to be modified.

(1) Unfocused beam

The spot was approximated as an elliptical shape. First the horizontal dimension projected onto the sample was calculated. Then the spot area was calculated. The horizontal spot of the beam onto the sample was at an 18.9° angle from its normal. Thus, the horizontal width is calculated to be

$$S_x = (2{,}235\ \mu\text{m})\cos(18.9) = 2.115\ \text{mm}. \qquad \text{(C-8)}$$

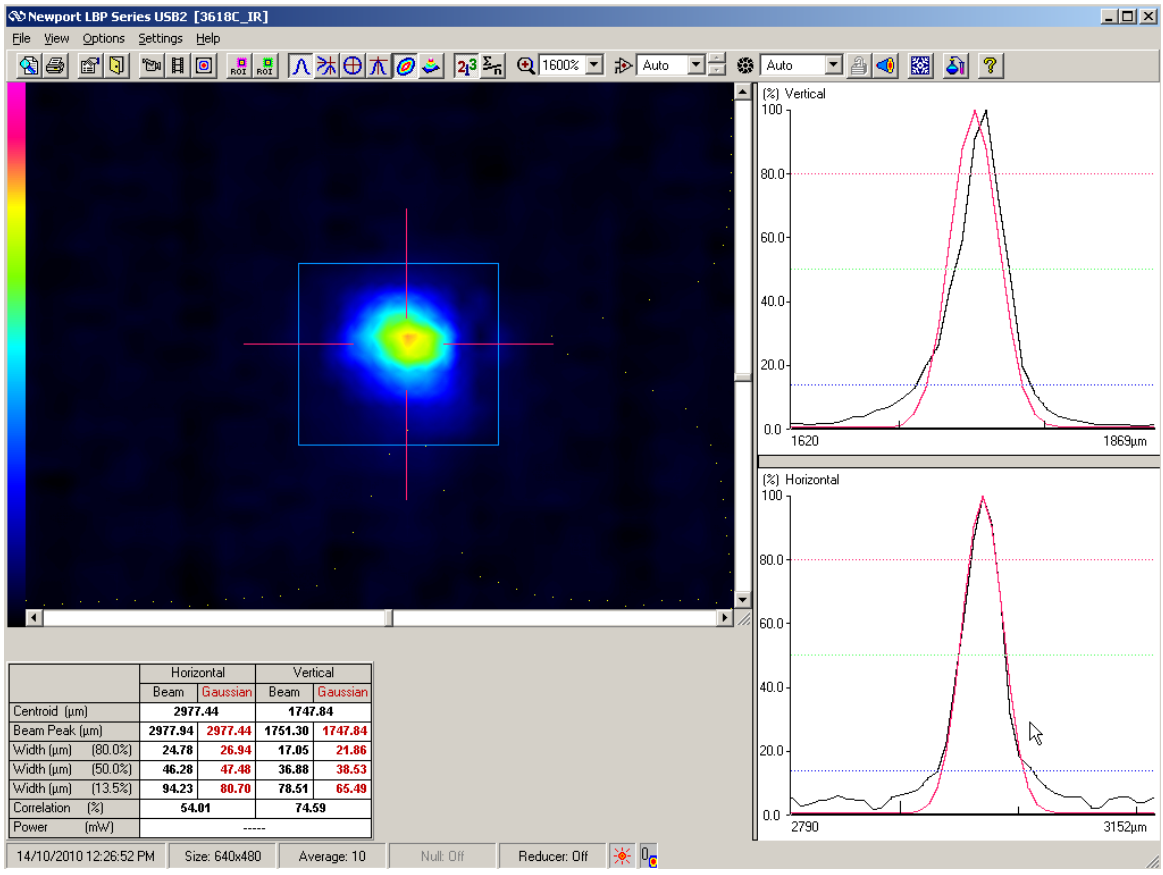

Fig. C.2: Screenshot of laser beam profiler measurement of laser beam at focus of 75.6 mm focal length biconvex lens. The horizontal width is 79 um, shown under the column labelled "vertical", and the vertical width is 94 um, shown under the "horizontal" column. The $1/e^2$ (13.5% of the peak intensity) width was used.

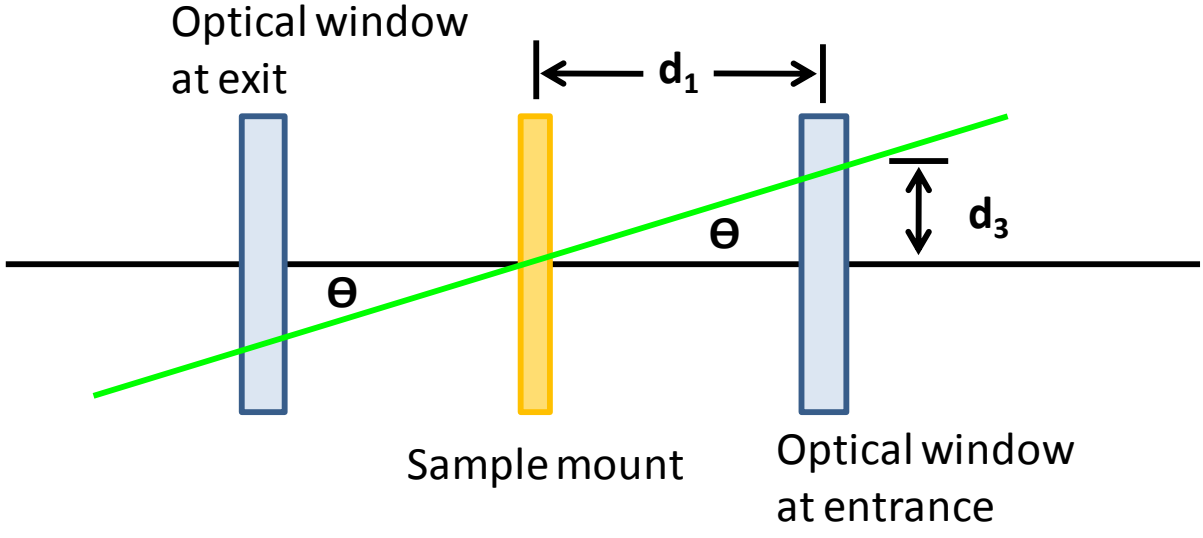

Fig. C.3: Laser beam (green) entering and exiting cryostat. The angle of incidence Θ on the sample is calculated by finding the distances d_1 and d_3.

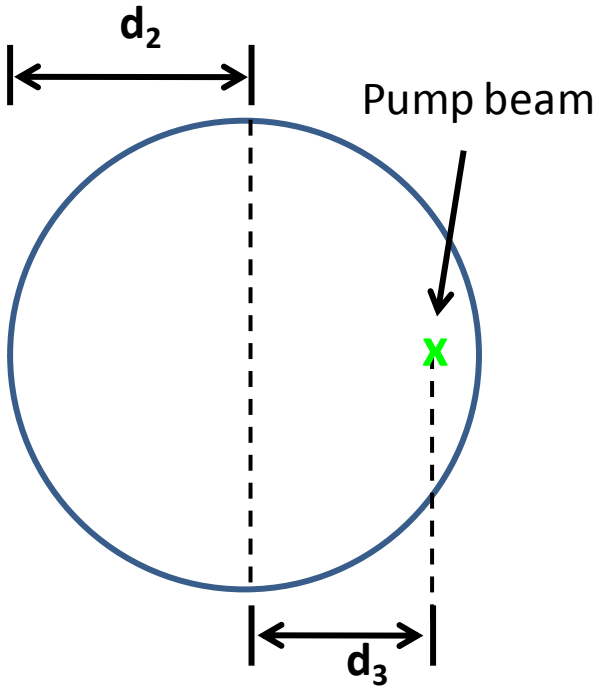

Fig. C.4: View of optical window of beam entering cryostat. The distance d_2 is the diameter of the optical window and d_3 is the distance between the centre of the window (the point at which the beam impinges the sample) and the point at which the beam enters the cryostat window, shown by the green "x".

The area of the unfocused elliptical spot with a major axis length S_y and minor axis length S_x is therefore

$$A = \pi S_x S_y = \pi \left(\frac{2115\ \mu m}{2}\right)\left(\frac{226\ \mu m}{2}\right) = 3.756\ mm^2. \quad \text{(C-9)}$$

(2) Focused beam

The spot was approximated as an elliptical shape. First the horizontal dimension projected onto the sample was calculated. Then the spot area was calculated. The horizontal spot of the beam onto the sample was at an 18.9° angle from its normal. Thus, the horizontal width is calculated to be

$$S_x = (79\ \mu m)\cos(18.9) = 75\ \mu m. \quad \text{(C-10)}$$

The area of the focused elliptical spot with a major axis length S_y and minor axis length S_x is therefore,

$$A = \pi S_x S_y = \pi \left(\frac{75}{2}\right)\left(\frac{94}{2}\right) = 5,500\ \mu m^2. \quad \text{(C-11)}$$

The spot size was studied as the profiler was moved between 1 and 3 mm from its focal spot. Table 8 summarises the results. Note that this time the beam width was larger. Distances from the focus were found from the micrometer actuator on the beam profiler's translation stage. The plus and minus signs indicate movement of the profiler in two different directions along the lens' axis. Note that the movement of the stage was not precisely along the lens' axis, so these measurements are not completely accurate but still show that the beam diameter does not change very much as it is moved a few hundred microns away from its focus.

Table 8: Width of beam at various distances from focus of 75.6 mm biconvex lens

Vertical width (µm)	**Horizontal width (µm)**	**Distance from focus (mm)**
102.12	79.28	0.000
101.91	79.81	+1.000
101.82	86.76	+2.000
118.04	98.26	+3.000
112.22	93.64	-1.000

Appendix D Spectrometer bandpass and resolution

The spectrometer images an optical signal at its entrance slit onto the exit plane. Two important properties of the spectrum that is detected at the exit plane are (1) the bandpass and (2) the spectral resolution. The bandpass is the range of wavelengths that are focused on the exit plane, while the spectral resolution is a measure of the minimum separation of neighbouring spectral lines that can be resolved. These two properties, related to one another, determine the final spectrum and depend on a number of factors within the instrument.

Instrument line profile:

Any spectral source can be considered as a superposition of infinite monochromatic lines. The spectrum of a monochromatic source would ideally be recorded as a single, infinitely narrow line. Figures D.1 (a) and (b) show that the respective "real" and ideal recorded spectra of such a source are in agreement. Figure D.1 (c), on the contrary, shows that the actual recorded spectrum is a broadened peak.

The origin of this broadening comes from many factors within the instrument. The recorded spectrum is a convolution of the real spectrum and the instrument line profile that broadens the peak. The spectral resolution of adjacent peaks, therefore, is limited by the broadening from the instrument, or the instrument line profile.

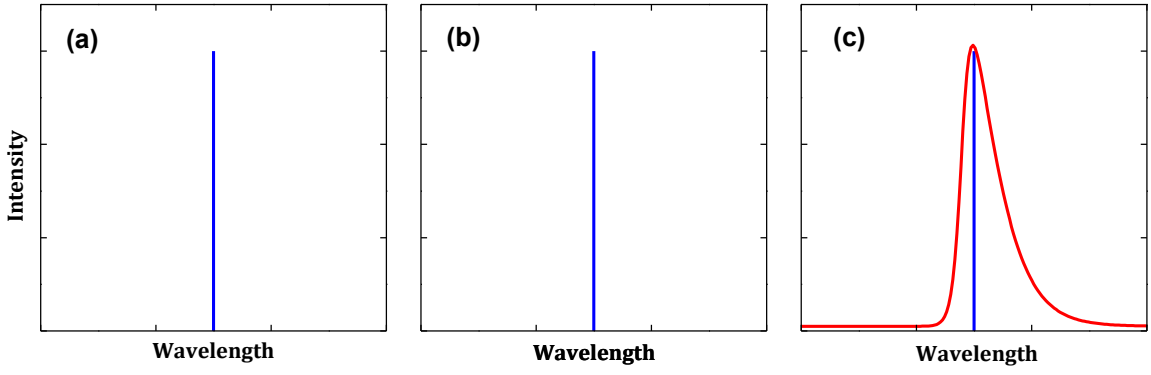

Fig. D.1: Instrumental broadening of a monochromatic source. Adapted from Horiba Jobin Yvon [34] (a) Profile of a true monochromatic source. (b) Ideal recorded spectrum of a true monochromatic source. (c) Actual recorded spectrum (red) of a true monochromatic source (blue).

Dependence of FWHM of measured signal:

Approximating the spectral profile as a Gaussian function, the FWHM of the recorded signal can be represented by the following equation [34]:

$$FWHM = d\lambda_{Slits}^2 + d\lambda_{Resolution}^2 + d\lambda_{Line}^2. \quad \text{(D-1)}$$

The first term in Eq. (D-1), $d\lambda_{Slits}$, includes broadening contributions from the entrance and exit slits. It also includes linear dispersion from the gratings. The second term, $d\lambda_{Resolution}$, comes from the instrumental profile and includes broadening from system aberrations and diffraction effects. The third term, $d\lambda_{Line}$, is the natural line width of the signal.

The entrance and exit slit sizes are important in determining the broadening of the recorded spectrum. If they are finite in size and there are not any other effects that broaden the signal, the instrument line profile is a convolution of the two slit functions. If the slit widths are reduced to an infinitely narrow size and if aberrations are negligible, the line profile is a diffraction pattern. If they are infinitely narrow and aberration effects are much larger than diffraction effects, the line profile due to diffraction becomes enlarged.

Determining the FWHM instrument profile:

The FWHM instrument profile can be determined by measuring the width of a narrow laserline and calculating the bandpass due to the slit width and grating dispersion. The above discussion indicates that there are certain slit width parameters that give the system's best resolution settings. Changing the slit widths from the setting at the limiting resolution alters the resolution.

The bandpass of the signal at the exit plane is as follows [34]:

$$BP = w\,\frac{d\lambda}{dx}. \quad \text{(D-2)}$$

In Eq. (D-2), $d\lambda/dx$ is the linear dispersion. This corresponds to the number of wavelength intervals (usually in nm) within each unit distance across the focal plane (usually in mm). The parameter w is the largest slit width of either the entrance or exit slit.

The signal at the entrance slit is both horizontally and vertically magnified when imaged at the exit plane. The grating introduces a horizontal magnification factor that is

wavelength dependent, shown in Eq. (D-3), while the vertical magnification is the same for all wavelengths of light, shown in Eq. (D-4) [34]:

$$W' = W \frac{\cos(\alpha)}{\cos(\beta)} \frac{L_B}{L_A} \tag{D-3}$$

$$h' = \frac{L_B}{L_A} \text{h}. \tag{D-4}$$

In Eq. (D-3), *W'* is the width of the image at the exit slit while *W* is the width of the entrance slit. The angle α is the angle of incidence and β is the angle of diffraction. The focal length at the entrance is L_A and at the exit is L_B. In Eq. (D-4), *h'* is the image at the exit plane while *h* is the height of the entrance slit. Using Eq. (D-3) and (D-4), Eq. (D-2) becomes [34]:

$$BP = w \left(\frac{\cos(\beta)}{k\, n\, L_B}\right) = \frac{w \cos(\alpha)}{k\, n\, L_A}, \tag{D-5}$$

where *k* is the order of diffraction and *n* is the grating groove density.

Equations (D-2) and (D-5) indicate that the slit widths need to be small, but finite in size. The exit slit width is defined by the number of pixels corresponding to a bandpass or wavelength. For a CCD detector, this is normally 3-6 pixels. The CCD detector has pixels of size 26 x 26 μm.

Experiment:

The spectrum of a 632.8 nm helium neon (HeNe) laser was measured at various spectrometer entrance slit widths to determine the slit width at the limiting resolution of the instrument using the CCD detector and Grating III. The laser power was attenuated from ~10 mW with neutral density filters. The beam had a diameter of ~ 1 mm.

This experiment was done under two different conditions. In the first case, the unfocused laser beam was directed into the spectrometer. In the second case, the laser was expanded with a beam expander and then focused onto the entrance slit of the spectrometer to fill as much of the grating area as possible. The two different setups are described below.

(1) Unfocused beam

The laser was attenuated with neutral density filters to have a power of ~1.51 nW measured with a Newport 918D-SL-OD3 silicon photodetector and 842-PE optical power meter. The

beam was then passed through a pinhole to avoid any extra reflections entering the spectrometer. This beam was reflected off a glass microscope slide which was aligned to direct the beam into the spectrometer. Note that in this case, the beam encounters only a small spot on the grating.

(2) Expanded and focused beam

There are a few differences in this setup that the one described in (1). The laser power was reduced to ~8.51 nW with neutral density filters. After reflection off the glass slide, the beam was expanded ten times using a Newport LC-075 beam expander. A pinhole set at the diameter of 10 mm was placed after the beam expander to ensure that this diameter beam was passed to the focusing lens. The focusing lens was a 50.2 mm biconvex lens placed directly in front of the spectrometer. Using d = 10 mm and f = 50.2 mm in Eq. (28), we find that the f/# of the light entering the spectrometer is 5.02. This is greater than the spectrometer's f/# of 4.1, meaning that the light underfills the total area of the grating; however, it fills a much larger area than in the first case.

A series of spectra of the HeNe were taken as a function of entrance slit width. Slit widths were investigated between 0.01-0.5 mm at a fixed exposure time of 0.1 seconds. Figures D.2 and D.3 show the laser spectrum at various slit widths in cases (1) and (2), respectively.

Figure D.3 shows a non-symmetric spectrum at larger slit widths. This becomes apparent for slit widths greater than 0.15 mm. This may be a cause of improper focusing of the beam onto the entrance slit. The focusing lens had a short focal length. There was not much distance between the lens and the entrance slit, so the lens could have been easily misaligned.

Another possible reason for the asymmetric laser spectrum could have been due to diffraction effects caused by placing the pinhole around the expanded beam. It is noted that an aperture should be at least three or four times larger than the waist radius of a Gaussian beam to not alter its Gaussian shape. As the beam was expanded from 1 mm to 10 mm, the expected waist radius of the expanded beam is 5 mm. Thus, the aperture was only twice as large as its waist radius and may have easily introduced diffraction effects into the beam profile.

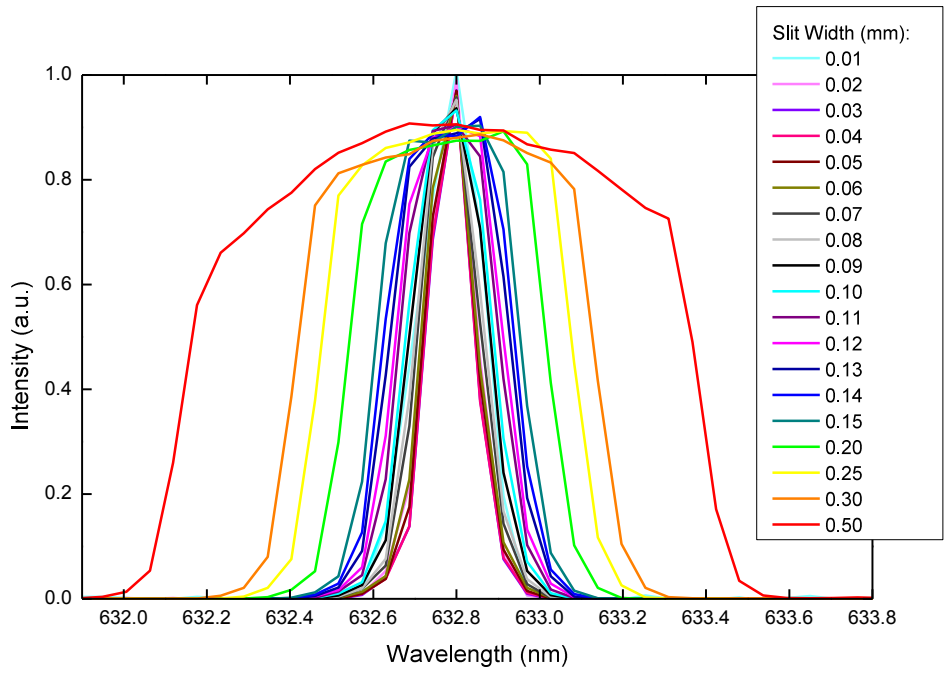

Fig. D.2: HeNe laser spectra at various entrance slit widths between 0.01-0.50 mm for case (1) of the unfocused beam. The spectra are normalized with respect to the maximum intensity value at 632.8 nm of the peak that had the highest intensity. The laser power was measured to be ~1.51 nW. An exposure time of 0.1 seconds was used.

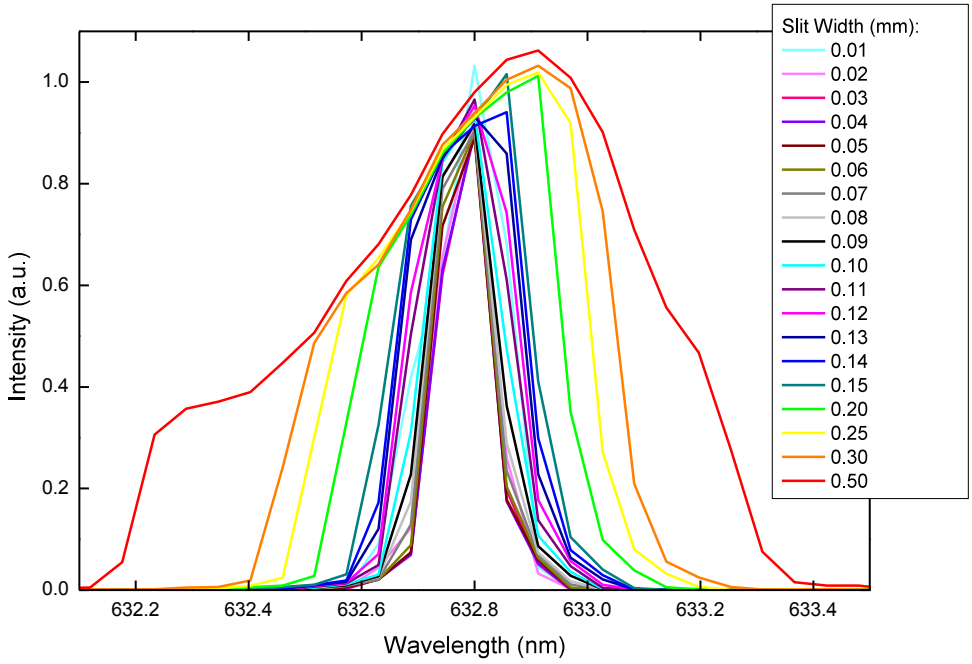

Fig. D.3: HeNe laser spectra at various entrance slit widths between 0.01-0.50 mm for case (2) of the focused beam. The spectra are normalized with respect to the maximum intensity value at 632.8 nm of the peak that had the highest intensity. The laser power was measured to be ~8.51 nW. An exposure time of 0.1 seconds was used.

Figures D.4 and D.5 show a plot of the FWHM as a function of slit width for the data in Figures D.2 and D.3, respectively. On each of these plots, the predicted curve for FWHM as a function of slit width is also plotted. For the predicted curve, a value for linear dispersion of 2.35 nm/mm given by Horiba Jobin Yvon [34] for a grating of groove density 1200 g/mm at 435 nm was used. This number should be a good estimate for the value at 632.8 nm. Equation (D-5) shows the linear dispersion is proportional to the bandpass.

The FWHM values were found by fitting a Gaussian to each laser spectrum, finding the peak height, and then finding the corresponding wavelength positions at half the peak height. A Gaussian fit was done as each recorded spectrum only had a few data points. Figure D.6 shows and example of a Gaussian fit to the spectrum taken at a slit width of 0.02 mm for case (1). By the data shown in Figures D.4 and D.5, it is concluded that the slit width of limiting resolution of the spectrometer is 0.05 mm.

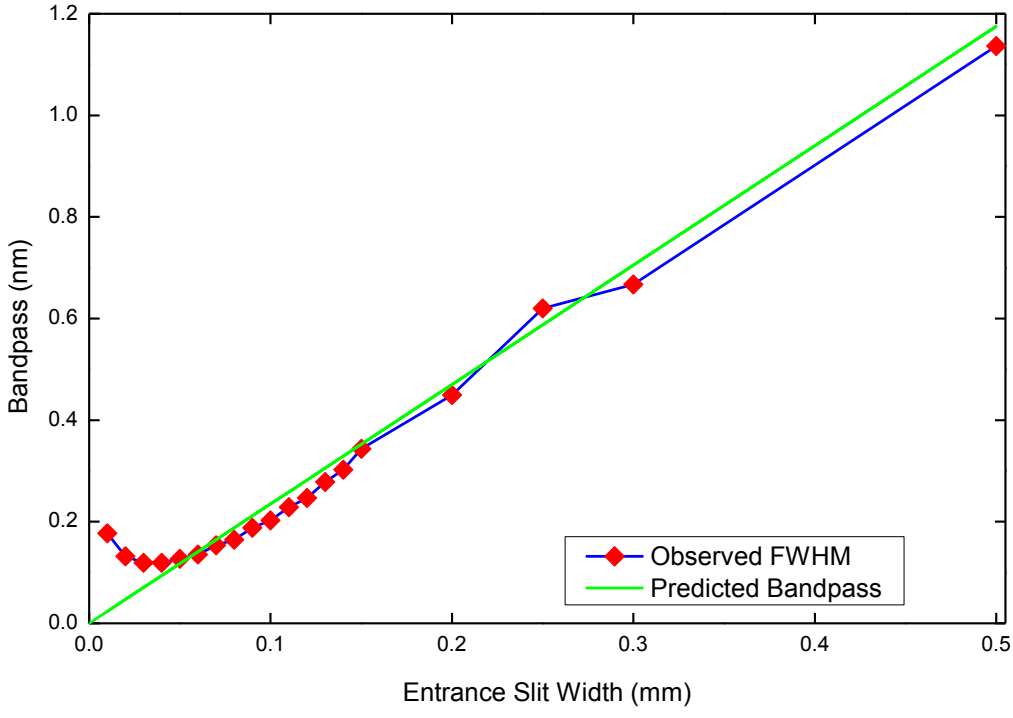

Fig. D.4: FWHM of HeNe as a function of entrance slit width for case (1) of the unfocused beam. The red data points, connected by the blue line for visual aid, are the observed FWHM of the spectra. The predicted linear dispersion is shown in green. The predicted curve is in agreement with the experimental data points above ~ 0.5 mm.

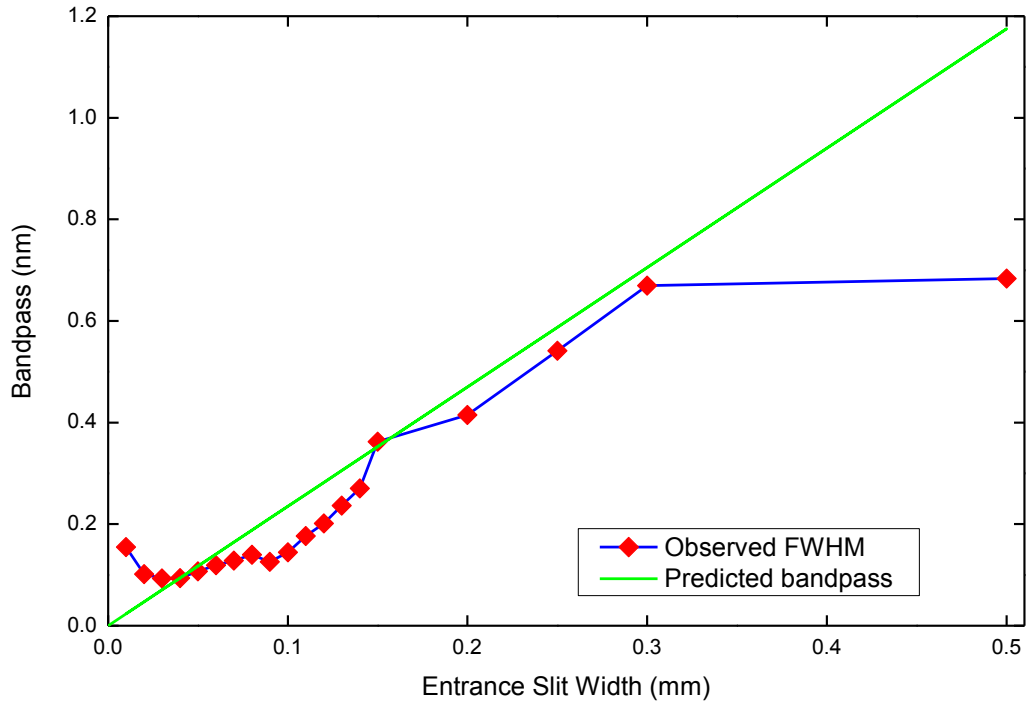

Fig. D.5: FWHM of HeNe as a function of entrance slit width for case (2) of the focused beam. The red data points, connected by the blue line for visual aid, are the observed FWHM of the spectra. The predicted linear dispersion is shown in green. The observed FWHM values are more scattered in this case, due to the asymmetric spectra shown in Fig. 3. There is some agreement between the predicted and measured data above slit widths of 0.05 mm, with the exception of the data point at 0.5 mm.

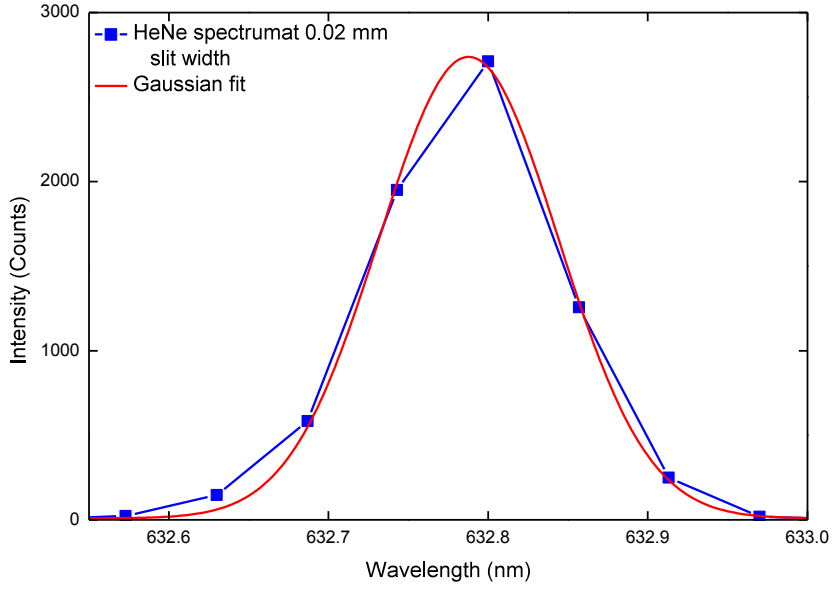

Fig. D.6: Gaussian fit (red) to HeNe spectrum (blue) taken at an entrance slit width of 0.02 mm for the experiment in case (1). Note that the raw data has only 8 data points in the spectrum.

Reference

[1] Young, H. D. and Freedman, R. A., [University Physics: 11th Edition], Pearson Education Inc., San Francisco, California, 1503-1577 (2004).

[2] Schmid, G., [Nanoparticles: From theory to applications], Wiley-VCH, Weinberg, 321-322 (2004).

[3] Chang, L. L. and Esaki, L., "Semiconductor quantum heterostructures," Phys. Today, 45(10), 36-43 (1992).

[4] Chang, L. L., Esaki, L., and Tsu, R.,"Resonant tunnelling in double semiconductor barriers," Appl. Phys. Lett., 24(12), 593-595 (1974).

[5] Guyot-Sionnest, P., "Recent advances in quantum dot physics: Colloidal quantum dots," C. R. Physique, 9, 777-787 (2008).

[6] Ekimov, A. I. and Onushchenko, A. A., "Quantum size effect in three-dimensional microscopic semiconductor crystals," JETP Lett., 34(6) 345-349 (1981).

[7] Brus, L. E., "A simple model for the ionization potential, electron affinity, and aqueous redox potentials of small semiconductor crystallites," J. Chem. Phys., 79(11), 5566-5571 (1983).

[8] Warnock, J. and Awschalom, D. D., "Quantum size effects in simple colored glass," Phys. Rev. B, 32(8) 5529-5531 (1985).

[9] Reiss, P., Protière, M. and Li, L., "Core/shell semiconductor nanocrystals," Small, 5(2), 154-168 (2009).

[10] Veilleux, V., Lachance-Quirion, D., Doré, K., Landry, D. B., Charette, P. G. and Allen, C. Nì., "Strain-induced effects in colloidal quantum dots: lifetime measurements and blinking statistics," Nanotechnology, 21(13), 1340024 (2010).

[11] Moison, J. M., Houzay, F., Barthe, F., and Leprince, L., "Self-organized growth of regular nanometer-scale IhAs dots on GaAs," Appl. Phys. Lett., 64(2), 196-198 (1994).

[12] Nirmal, M. and Brus, L., "Luminescence photophysics in semiconductor nanocrystals," Acc. Chem. Res., 32(5), 407-414 (1999).

[13] Liu, W., Howarth, M., Greytak, A. B., Zheng, Y., Nocera, D. G., Ting, A. Y. and Bawendi, M. G., "Compact biocompatible quantum dots functionalized for cellular imaging," J. Am. Chem. Soc., 130(4), 1274-1284 (2008).

[14] Saleh, B. E. A. and Teich, M. C., [Fundamentals of Photonics: Second Edition], John Wiley & Sons, Inc., Hoboken, New Jersey, 75-94, 209-214, 682-702 (2007).

[15] Colvin, V. L, Schlump, M. C. and Alivisatos, A. P, "Light emitting diodes made from cadmium selenide nanocrystals and a semiconducting polymer," Nature, 370, 354-356 (1994).

[16] Talapin, D. V., Lee, J., Kovalenko, M. V. and Shevchenko, E. V., "Prospects of colloidal nanocrystals for electronic and optoelectronic applications," Chem. Rev., 110(1), 389-458 (2010).

[17] Johnston, K. W., Pattantyus-Abraham, A. G., Clifford, J. P., Myrskog, S. H., MacNeil, D. D., Levina, L. and Sargent, E. H., "Schottky-quantum dot photovoltaics for efficient infrared power conversion," Appl. Phys. Lett., 92(15), 151115 (2008).

[18] Sun, S., Murray, C. B., Weller, D., Folks, L. and Moser, A., "Monodisperse FePt Nanoparticles and Ferromagnetic FePt Nanocrystal Superlattices," Science, 287(5460), 1989-1992 (2000).

[19] Gómez, D. E., Califano, M. and Mulvaney, P., "Optical properties of semiconductor nanocrystals," Phys. Chem. Chem. Phys., 8(43), 4989-5011 (2006).

[20] Griffiths, D. J., [Introduction to Quantum Mechanics: Second Edition], Pearson Education Inc., Upper Saddle River, New Jersey, 224-229 (2005).

[21] Nanda, K. K., Kruis, F. E. and Fissan, H., "Energy levels in embedded semiconductor nanoparticles and nanowires," Nano Lett., 1(11), 605-611 (2001).

[22] Eisberg, R. and Resnick, R., [Quantum Physics of Atoms, Molecules, Solids, Nuclei, and Particles], John Wiley & Sons, Inc., New York, 232-237 (1985).

[23] Lea, S. M., [Mathematics for Physicists], Brooks/Cole, Thomson Learning Inc., Belmont, California, 419-425 (2004).

[24] Kreyszig, E., [Advanced Engineering Mathematics: Fifth Edition], John Wiley & Sons, New York, 173-183 (1983).

[25] BenDaniel, D. J. and Duke, C. B., "Space-charge effects on electron tunnelling," Phys. Rev., 152(2), 683-692 (1966).

[26] Pellegrini, G., Mattei, G. and Mazzalodi, P., "Finite depth square well model: Applications and limitations," J. Appl. Phys., 97(7), 073706-1-8 (2005).

[27] Lippens, P. E. and Lannoo, M., "Calculation of the band gap for small CdS and ZnS crystallites," Phys. Rev. B, 39(15), 10935-10942 (1989).

[28] Valenta, J., Juhasz, R. and Linnros, J., "Photoluminescence from single silicon quantum dots at room temperature," J. of Luminescence, 98(1-4), 15-22 (2002).

[29] Valerini, D., Creti, A. and Lomascolo, M., "Temperature dependence of the photoluminescence properties of colloidal CdSe/ZnS core/shell quantum dots embedded in a polystyrene matrix," Phys. Rev. B, 71(23), 235409-1-6 (2005).

[30] Varshni, V. P., "Temperature dependence of the energy gap in semiconductors," Physica (Amsterdam), 34, 149-154 (1967).

[31] Nirmal, M., Daboussi, B. O., Bawendi, M. G., Macklin, J. J., Trautman, J. K., Harris, T. D. and Brus, L. E., " Fluorescence intermittency in single cadmium selenide nanocrystals," Nature, 383, 802-804 (1996).

[32] Lee, S. F., Osborne and M. A., "Brightening, blinking, bluing and bleaching in the life of a quantum dot: Friend or foe?," ChemPhysChem, 10(13), 2174-2191 (2009).

[33] Vij, D. R., [Luminescence of Solids], Plenium Press, New York, 1-3,53-67,95 (1998).

[34] "The optics of spectroscopy" tutorial, Horiba Jobin Yvon, http://www.horiba.com/us/en/scientific/products/optics-tutorial/monochromators-spectrographs/#c3756 (April 15, 2010).

[35] Kagan, C. R., Murray, C. B. and Bawendi, M. G., "Long-range resonance transfer of electronic excitations in close-packed CdSe quantum-dot solids," Phys. Rev. B, 54(12), 8633-8643 (1996).

[36] Halliday, D., Resnick, R. and Walker, J., [Fundamentals of Physics: Fifth Edition], John Wiley & Sons, Inc., New York, 459 (1997).

[37] Leatherdale, C. A., Woo, W.-K., Mikulec, F. V. and Bawendi, M. G., "On the absorption cross section of CdSe nanocrystal quantum dots," J. Phys. Chem. B, 106(31), 7619-7622 (2002).